ULTRACOMPACT OPTICAL FIBER SENSORS BASED ON 3D μ-PRINTED FERRULE/FIBER-TOP MICROSTRUCTURES

YAO MIAN

PhD

The Hong Kong Polytechnic University

2021

The Hong Kong Polytechnic University

Department of Electronic and Information Engineering

Ultracompact Optical Fiber Sensors Based on 3D μ-Printed Ferrule/Fiber-Top Microstructures

YAO MIAN

A thesis submitted in partial fulfillment of the requirements for the degree of Doctor of Philosophy

December 2019

CERTIFICATE OF ORIGINALITY

I hereby declare that this thesis is my own work and that, to the best of my knowledge and belief, it reproduces no material previously published or written, nor material that has been accepted for the award of any other degree or diploma, except where due acknowledgement has been made in the text.

____ (Signed)

YAO Mian (Name of student)

Abstract

Optical fibers have become a versatile and enabling technology for development of various kinds of sensors because of their advantages such as small size, low weight, immunity to electromagnetic interference, remote sensing and multiplexing capabilities. Over the past decades, tremendous efforts have been made to develop new fiber-optic sensors. Notably, optical fiber-tip devices based on micromachined ferrule/fiber-top structures have become a very unique technology for development of miniature fiber-optic sensors. However, as the geometry of the ferrule/fiber-end surface is not compatible with conventional micro/nano-fabrication technologies, it remains challenges to fabricate 3D complex structures such as suspended mirrors to develop high-performance fiber-tip sensors for applications where miniaturization is critical. In this thesis, a novel optical 3D μ-printing platform established by our research team is introduced. With this printing technology, three kinds of ultracompact optical ferrule/fiber-top sensors are developed for measuring displacement, refractive index, and acoustic wave, respectively.

Firstly, small optical fiber displacement sensors are fabricated by directly printing polymer suspended mirrors on the end surface of fiber-optic ferrules. With an own-established optical 3D μ-printing platform, three kinds of ferrule-top suspended-mirror devices (SMDs) are rapidly fabricated by using SU-8 photoresist. Optical reflection spectra of the fabricated SMDs are measured and then analyzed by using fast Fourier transform. The application of the ferrule-top SMD as a miniature displacement sensor is experimentally demonstrated.

Secondly, ultrasmall optical fiber refractive-index sensors are developed by directly printing polymer suspended microbeams on the end surface of standard single-mode optical fibers. The reflection spectra of the fabricated fiber-tip devices have been measured and used to analyze the Fabry-Pérot (FP) cavities formed by suspended microbeams. The optical fiber-tip sensors can detect the RI changes of both liquid and gas and can also be used to measure the pressure of ambient environment via the detection of pressure induced refractive-index change. High sensitivities of 917.3 nm/RIU to RI change and 4.29 nm/MPa to gas-pressure change have been achieved experimentally. Such ultrasmall optical fiber-tip sensors with remote sensing capability are promising in microfluidic biosensing and environmental monitoring applications.

Lastly, ultracompact fiber-optic acoustic sensors are presented by directly printing suspended optomechanical microresonator on the end-face of standard single-mode optical fiber. The suspended optomechanical microresonator acts as a reflection mirror and forms a Fabry-Pérot cavity together with the end-face of optical fiber. The mechanical resonance of the fiber-top optomechanical microresonator is analyzed by finite-element method (FEM). The response of the sensor to both acoustic waves and ultrasonic waves are experimentally tested and compared with simulation results. The optical fiber-tip sensor shows a high sensitivity of 118.3 mV/Pa and a corresponding noise equivalent acoustic signal level of 0.328 μPa/Hz$^{1/2}$ at audio frequencies. With a resonance-enhanced mechanism, the sensitivity is further enhanced at the frequency of fundamental vibration resonance of the optomechanical resonator.

Publications arising from the thesis

Journal papers:

1. **M. Yao**, Y. Zhang, X. Ouyang, A. P. Zhang, H.-Y. Tam, and P. K. A. Wai, "Ultracompact Optical Fiber Acoustic Sensors Based on a Fiber-Top Spirally-Suspended Optomechanical Microresonator," Opt. Lett. 45, 3516-3519 (2020).
2. **M. Yao**, X. Ouyang, J. Wu, A. P. Zhang, H.-Y. Tam, and P. K. A. Wai, "Optical Fiber-Tip Sensors Based on In-Situ μ-Printed Polymer Suspended-Microbeams," Sensors 18, 1825 (2018)
3. **M. Yao**, J. Wu, A. P. Zhang, H.-Y. Tam, and P. K. A. Wai, "Optically 3-D μ-Printed Ferrule-Top Polymer Suspended-Mirror Devices," IEEE Sensors Journal 17, 7257-7261 (2017).
4. J. Wu, **M. Yao**, F. Xiong, A. P. Zhang, H.-Y. Tam, and P. K. A. Wai, "Optical Fiber-Tip Fabry–Pérot Interferometric Pressure Sensor Based on an In Situ μ-Printed Air Cavity," Journal of Lightwave Technology 36, 3618-3623 (2018).
5. J. Wang, **M. Yao**, C. Hu, A. P. Zhang, Y. Shen, H.-Y. Tam, and P. K. A. Wai, "Optofluidic tunable mode-locked fiber laser using a long-period grating integrated microfluidic chip," Opt. Lett. 42, 1117-1120 (2017).
6. M.-J. Yin, **M. Yao**, S. Gao, A. P. Zhang, H.-Y. Tam, and P. K. A. Wai,

"Rapid 3D Patterning of Poly(acrylic acid) Ionic Hydrogel for Miniature pH Sensors," Advanced Materials 28, 1394-1399 (2016).

Conference papers:

1. **M. Yao**, X. Ouyang, A. P. Zhang, H.-Y. Tam, and P. K. A. Wai, "Optical fiber-tip microfluidic refractive-index sensors," in CLEO Pacific Rim Conference 2018, OSA Technical Digest (Optical Society of America, 2018), F1E.3, DOI: 10.1364/CLEOPR.2018.F1E.3. (received Best Student Paper Award).
2. **M. Yao**, J. Wu, A. P. Zhang, H.-Y. Tam, and P. K. A. Wai, "Optical fiber end-facet polymer suspended-mirror devices," in 2017 25th Optical Fiber Sensors Conference (OFS), 2017, DOI: 10.1117/12.2267632.
3. **M. Yao**, P. K. A. Wai, J. Wu, A. P. Zhang, and H.-Y. Tam, "Optical 3D μ-printing of ferrule-top polymer suspended-mirror devices," in 2016 IEEE SENSORS, 2016, DOI: 10.1109/ICSENS.2016.7808491. (finalist in Student Best Paper Award).

Acknowledgements

I would like to appreciate everyone who provided me with help during the pursuing of my PhD degree in the Hong Kong Polytechnic University.

First of all, I would like to express my sincerest gratitude to my chief supervisor, Prof. P. K. A. Wai, for his patient and kind guidance. His profound knowledge and constructive suggestions help me a lot in my PhD period. And his passion, meticulosity and enthusiasm on research set me a good example and will influence me in the following days.

I also would like to thank Dr. A. Ping Zhang, my co-supervisor, for providing me with the first-class equipment and environment to do research. I am grateful for his suggestive advice and efforts on revising my writings.

I wish to thank Dr. Mingjie Yin for his help in material preparation, experiment design and data processing. I am very grateful to Dr. Jushuai Wu and Dr. Shaorui Gao for their support in the setup of experimental platform and optical design. Besides I appreciate Dr. Zhengyong Liu, Dr. Bin Zhou, Dr. Yangxi Zhang, Miss. Yaxi Yan, Mr. Xia Ouyang, Mr. Feng Xiong, Mr. Xin Cheng, Mr. Julien Bonefacino for their help and useful discussions on my experiments.

I wish to acknowledge Dr. Ming-Leung Vincent Tse, Dr. Chi-Fung Jeff Pun and Dr. Shun-Yee Michael Liu for their kindly technical help. I also wish to express my gratitude to everyone in the Photonics Research Centre and my friends in Hong Kong for their help in my study and life. I really appreciate the four-year wonderful life in Hong Kong, and it will be a great treasure in my life.

Finally, I want to express my gratitude to my parents for their unselfish dedication and support. This thesis is dedicated to them to express my deepest love and gratitude!

Table of Contents

List of Figures

List of Tables

List of Acronyms

Acronyms	**Description**
AFM	Atomic force microscope
ASE	Amplified spontaneous emission
CCD	Charge-coupled device
DMD	Digital-micromirror device
DPI	Dual polarized interferometer
FBG	Fiber Bragg grating
FEM	Finite element method
FFT	Fast Fourier transformation
FP	Fabry-Pérot
FPI	Fabry-Pérot interferometer
FSR	Free spectral range
FWHM	Full width at half maximum
LCD	Liquid crystal display
LPG	Long period grating
MEMS	Microelectromechanical systems
MZI	Mach-Zehnder interferometer
OMsL	Optical maskless stereolithography
OPPI	Octoxyphenylphenyliodonium hexafluoroantimonate
PGMEA	Propyleneglycol monomethylether acetate

PDMS	Polydimethylsiloxane
PMMA	Polymethyl methacrylate
RI	Refractive index
RIU	Refractive index units
SEM	Scanning electron microscope
SLM	Spatial light modulator
SMF	Single mode fiber
SOI	Silicon on insulator
SWCNT	Single-walled carbon nanotube
TBA	Tributylamine

Chapter 1

Introduction

1.1 Background

Nowadays information is generated, processed, stored, presented and transmitted in ever-increasing amounts [1]. As the key means of acquiring information, sensors are in high demand on efficient collection of many types of information, especially under the scheme of Internet of Things. Particularly, high-performance photonic sensors play a vital role in many application fields such as medicine, biotechnology, chemistry, food quality control, automotive, aerospace, and homeland security [2].

A photonic sensor is a miniature system in which the measurand induces modulations on the probe light in the form of amplitude, frequency or/and phase. The sensor will then output a signal which contains the information of the measurand after light-matter interaction and signal processing [3]. Compared with other sensing technologies, the advantages of photonic sensors include high sensitivity, wide dynamic range, low detection limit, electromagnetic immunities, biocompatibility, and multiplexing capacity. Because of these advantages, photonic sensors have become an active research area in the past decades. Different types of sensor have been proposed, such as surface plasmon resonance sensors [4], interferometer-based sensors [5], optical waveguide sensors [6], optical resonator sensors [7], optical fiber sensors [8], and photonic crystal sensors [9].

Optical fiber has become one of the promising technologies to develop new photonic sensors. Many optical fiber technologies, such as fiber Bragg gratings [10], long-period gratings [11], fiber Fabry-Pérot cavities [12], nanofibers based optical resonators [13], photonic crystal fibers [14] and other specialty optical fibers [15], have been demonstrated to develop various kind of sensors for sensing a great many of measurands. In particular, fiber-based photonic sensors have been widely applied in 'high performance' sensing applications where large dynamic range, wide bandwidth, and low noise are required simultaneously [16]. For example, in under water acoustic detection, high sensitivity and large dynamic range are simultaneously required because the background noise pressure can be 11 orders higher than the threshold detection level. Researchers took advantages of interferometric techniques to develop fiber-optic hydrophone whose dynamic strains is as low as $\sim 10^{-15}$ in the presence of static strains over 1% [17].

Notably, the flat end-surface of optical fiber provides a unique platform for developing miniature photonic sensors. The small size and large aspect ratio of optical fibers make it a promising candidate for in vivo and in situ sensing as a highly integrated photonic sensor device [18]. Because of its remote sensing capability of fiber-optic sensors, fiber-tip devices have applications in which the probe light is modulated by measurand at the fiber tip and the same fiber provides an easy access for signal retrieval and propagation. What is more, in biomedicine field, the small size of optical fibers allows minimally intrusive in situ and in vivo sensing of organisms [19]. Fiber tip devices have also been used for beam shaping. For example, polymer micro-tip with adaptable radius of curvature has been fabricated on the end surface of a single-mode fiber for efficient light coupling between a submicron size SOI-waveguide and the fiber [20]. Moreover, optomechanical devices have been demonstrated for pressure sensing [21], near-field probes [22], and atomic-force microscopy [23]. Finally, nanostructures have also been fabricated on fiber end-surface to investigate plasmonics [24] and surface-enhanced Raman scattering (SERS) [25].

Many fabrication techniques have been applied to pattern the flat end-surface of an optical fiber, for example photolithography [26], nanoimprinting [27], interference lithography [28], electron-beam lithography [29], focused ion-beam milling [30], two-photon polymerization [31], femtosecond laser ablation [32], and thin-film deposition [33]. Each fabrication technique has its advantages and drawbacks. For example, current photolithography systems are capable of patterning arbitrary 2D geometries at nanoscale. The resolution is sufficient for most applications and the cost is reasonable, however, alignment is a significant problem because the aspect ratio of optical fibers is too large to operate under contact mask aligner [19]. Moreover, conventional photolithography lacks 3D fabrication capability. Electron-beam lithography offers a resolution as high as sub-10 nm. However, the high costs and low throughput limit its use in many experiments. The resolution of focused ion-beam milling is comparable with electron-beam lithography, but only a small number of materials can be patterned.

1.2 Motivations and objectives of research

Though optical fiber-based photonic sensors have been intensively investigated in the past decades and a variety of micro/nano-fabrication techniques have been proposed to fabricate optical fiber sensors, the research and development of ultracompact optical fiber sensors based on fiber-top microstructures are still rare because of fabrication challenges. This research project aims to develop new photonic sensors based on 3D microstructures printed on the end surfaces of fiber-optic ferrule or optical fiber. Small-size high-performance optical fiber-tip sensors are highly desired in many sensing applications where the space is highly restricted. For instances, in many endoscopy devices, the sensors need to be small enough to be inserted into human body, while in microfluidic devices, the sensors need integrated within narrow microchannels. Moreover, the geometries of the fiber-top 3D microstructures are designed and optimized to improve the sensing performance of the fiber-tip sensors. For example, the mechanical resonance of microresonators has been employed to enhance the acoustic pressure sensitivity by printing spirally suspended mirrors on the end surface of optical fiber.

In this thesis, three different kinds of optical fiber sensors are developed by using the own-established optical μ-printing technologies based on maskless exposure approaches. Firstly, suspended mirror devices are successfully printed on the end-surface of ceramic ferrule and the displacement sensing application is demonstrated. Secondly, a suspended micro-beam is directly printed on the end-face of a standard single mode fiber and the device can work as refractive index sensor and pressure sensor. Lastly, fiber-tip acoustic sensors are fabricated by printing spirally-suspended optomechanical microresonators on the end surface of optical fiber.

1.3 Outline of Thesis

The chapters of this thesis are organized as below:

Chapter 1: Introduction. In this chapter, the background of optical fiber sensors is reviewed. The objectives of the research project are described, and the outline of the thesis is presented.

Chapter 2: Overview of optical fiber-tip sensors. In this chapter, the sensing mechanisms, fabrication techniques, and applications of optical fiber sensors are review. The optical 3D μ-printing technology and the testing of its microfabrication ability are presented in detail.

Chapter 3: Miniature optical fiber displacement sensors based on optically 3D μ-printed ferrule-Top suspended mirrors. In this chapter, an optical fiber displacement sensor has been presented by direct printing of different kinds of SMDs on the end-faces of optical fiber ferrules. The reflection spectra of the ferrule-top SMDs have been measured and then numerical analyzed by using fast Fourier transform to characterize the SMDs. The performance of the fabricated ferrule-top SMD-based displacement microsensor has been experimentally tested.

Chapter 4: Ultrasmall optical fiber refractive-index sensors based on in-situ μ-printed fiber-top suspended-microbeams. In this chapter, a miniature optical fiber refractive index sensor based on directly printed polymer suspended microbeams on the end-face of standard single-mode optical fiber is presented. The optical fiber-tip sensors have been demonstrated to detect the RI change of liquid and the air pressure, respectively. High sensitivities of 917.3 nm/RIU to RI change and 4.29 nm/MPa to gas-pressure change have been achieved.

Chapter 5: Ultracompact optical fiber acoustic sensors based on in situ μ-printed fiber-top optomechnical microresonators. In this chapter, optical fiber-tip acoustic sensors are developed by design and fabrication of a spirally-suspended optomechanical microresonator on the end surface of optical fiber. The mechanical resonance of the fiber tip sensor is analyzed by finite-element method (FEM). The response of the sensor to both acoustic waves and ultrasonic waves are measured. Its frequency response has been experimentally characterized and compared with theoretical analysis. The fabricated optical fiber acoustic sensor shows a high sensitivity of 118.3 mV/Pa at audio frequency and a corresponding noise equivalent acoustic signal level of 0.328 $\mu Pa/Hz^{1/2}$.

Chapter 6: Conclusions and future outlook. In this chapter, a summary of this thesis is given and future work on fiber tip sensors is presented.

Chapter 2

Overview of Optical Fiber-Tip Sensors

2.1 Introduction

The first optical fiber sensor can date back to the first half of the twentieth century when the flexible endoscopes were developed and widely used, which created a revolution in medicine that continues to today. The invention of low-loss optical fibers in the late 1970s paved the way for the development of modern fiber optic sensors.

Fiber optic gyroscopes based on the Sagnac effect and fiber optic hydrophones based on Mach–Zehnder interferometers were the most successful sensor of the first generation of fiber optic sensors development. Then Fabry-Pérot (FP) interferometers, either extrinsic or intrinsic, led the second wave of fiber optic sensors. The development of in-line Bragg grating optical filters originally designed for optical communication purposes started the third wave of fiber optic sensors development.

With the development of micro/nano-fabrication techniques, the integration of functional materials and structural modification on optical fibers has become a hot research area to investigate novel optical fiber sensors. The decoration of optical fibers with functional materials for specific sensing applications has been the main driving force to increase the number of measurable parameters and, to decrease the limits of detection (LODs) during the last decades. However, the small cross section, ultra-large aspect ratio and curved surfaces of optical fibers make them difficult to be surface micromachine by conventional micro/nano-fabrication strategies. In most cases, the poor control and the modest technological readiness of the integration methodologies, posed severe limitations in their applicability in real scenarios. As a consequence, although optical fibers provide ideal platforms for novel photonic sensors development, a great amount of work was required to set the first milestones related to the identification of suitable fabrication strategies able to correctly operate onto not conventional substrates as the case of optical fibers.

The flat end-face of an optical fiber is a uniquely unconventional substrate for sensor development. Its microscopic cross section and large aspect ratio provide unobtrusive access to remote and confined environments, while its biocompatibility, all-optical interrogation, and mechanical robustness provide access to hostile environments that feature extremes of temperature, pressure and electromagnetic interference.

2.2 Conventional optical fiber-tip thin-film FP cavity sensors

In this section, the working principles of optical fiber-tip sensors, especially for fiber-tip sensors based on thin-film FP cavity, are introduced and the fabrication techniques for conventional fiber-tip sensors are briefly reviewed. Here conventional sensors refer to devices whose sensing elements are generally entities with simple geometry such as diaphragms or semispherical cap. The manufacture technologies are commonly straightforward and inexpensive, whereas the micromachining precision, geometrical control ability and processing capability for complicated 3D microstructures are limited. Nevertheless, various types of conventional optical fiber-tip sensors have been developed, which show versatile sensing abilities with high performance.

2.2.1 Sensing principles

The foundation of the innovation and development of optical fiber-tip sensors is the physical or chemical mechanism underneath. Over the past decades, a number of operation principles have been exploited to investigate optical fiber-tip sensors and devices, including interferometers, optical microresonators, plasmonic resonances [24, 34-37], surface enhanced Raman scattering (SERS) [25, 27, 38-40], optical tweezers [41-43], metasurface [44-46], *etc*. In this section, we focus on Fabry-Pérot interferometers (FPIs) because it's closely related to my work presented in chapter 3-5. Detailed reviews about the sensing principles of fiber-tip sensor can be found in the literature [18, 47].

Fiber-optic interferometers have been extensively investigated and widely used in the past decades for various sensing applications. Among different kinds of interferometers, Fabry-Pérot interferometers (FPIs) are particularly attractive for the development of optical fiber-tip sensors because they can provide competitive sensitivities without the need of a long length of optical fiber compared with Mach-Zehnder interferometer and Michelson interferometer [48]. As shown in **Figure 2.1 (a)**, FPIs consist of two reflective surfaces, which can be the end-face of an optical fiber and a diaphragm. The round-trip propagation phase shift in the Fabry-Pérot cavity is given by

$$\phi = \frac{4\pi n_1 L}{\lambda}, \tag{2.1}$$

where n_1 is the refractive index of the medium between the two reflective surfaces, L is the cavity length, and λ is the optical wavelength in free space.

From Equation 2.1, the wavelength of the resonance dips in the reflection spectrum should satisfy the condition

$$\frac{4\pi n_1 L}{\lambda_m} = 2m\pi, \tag{2.2}$$

where m is an integer. Thus the resonance wavelength can be expressed as

$$\lambda_m = \frac{2n_1 L}{m}. \tag{2.3}$$

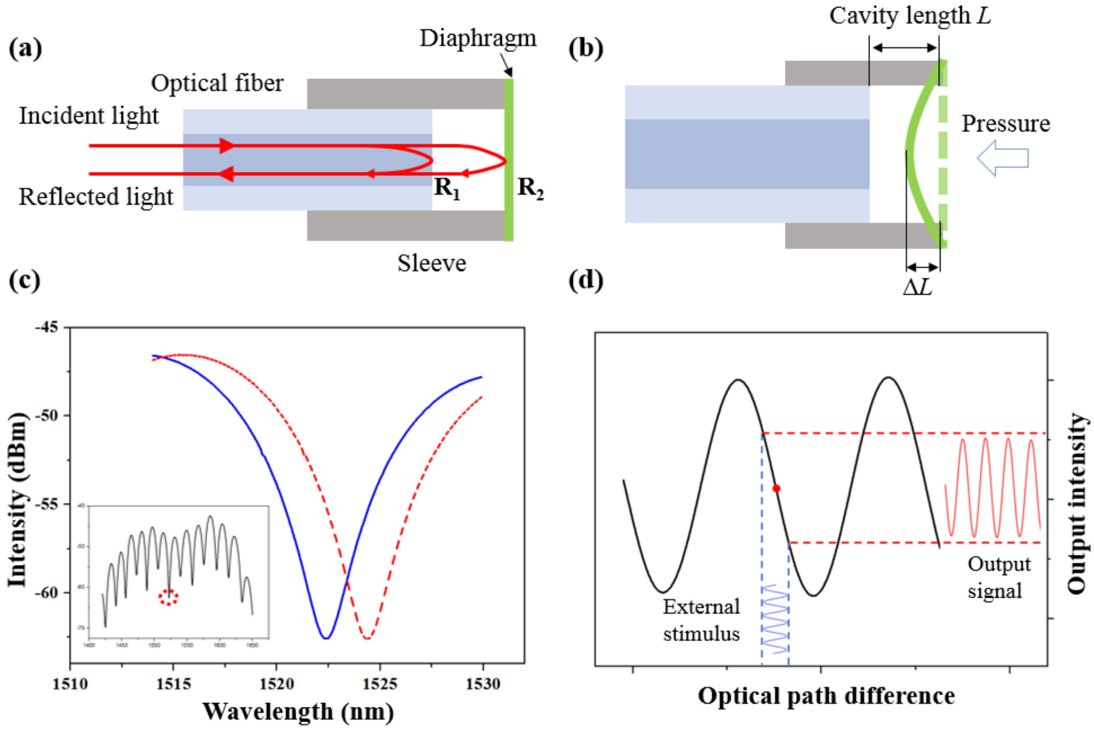

Figure 2.1 (a) Schematic diagram of a typical diaphragm-based fiber-optic FPI sensor. (b) Deformation of the membrane under external pressure. (c) Shift of the resonant dip when the cavity length or the refractive index of the medium changes. Inset shows the typical reflection spectrum of a FPI sensor. (d) Relationship between the intensity of reflected light and the variation of optical path difference of a FP cavity.

Equation 2.3 shows the peak/valley wavelength is related to the cavity length of the FPI and the refractive index of the medium filled in the FP cavity. One can monitor the shift of the resonant wavelength to determine the change in cavity length or refractive index of the medium induced by external stimulus. For example, elastic diaphragms are commonly used to develop fiber-tip pressure sensors. As illustrated in **Figure 2.1 (b)**, when the pressure applied to the diaphragm changes, the diaphragm will deform and as a result, the cavity length changes and the resonant wavelength shifts. Assuming the refractive index of the medium doesn't change when the diaphragm deflects, the change of the cavity length can be calculated as

$$\begin{aligned} \lambda_m + \Delta\lambda_m &= \frac{2n_1}{m}(L + \Delta L) \\ \Delta L &= \frac{m}{2n_1}\Delta\lambda_m = \frac{L}{\lambda_m}\Delta\lambda_m, \end{aligned} \tag{2.4}$$

where $\Delta\lambda_m$ is the peak wavelength shift.

Similarly, the linear relationship between the change in refractive index of the medium and peak wavelength shift can be expressed as

$$\Delta n = \frac{m}{2L}\Delta\lambda_m = \frac{n_1}{\lambda_m}\Delta\lambda_m. \tag{2.5}$$

This signal demodulation approach is called peak/valley-tracking method. **Figure 2.1 (c)** shows the shift of a resonant dip under circumstances where the cavity length or the refractive index of the medium filled in the FP cavity changes. Since commercially available optical spectrum analyzer can offer high spectrum resolution, this wavelength tracking method can achieve high resolution. However, the free spectrum range of the reflection spectrum limits the dynamic range of detection. what's more, the response time of sensors based on this demodulation method is limited by the scanning speed of optical spectrum analyzer, which makes it difficult to detect fast varying signals. Besides, the cavity length cannot be directly calculated by this method.

Instead of tracking a certain peak/valley wavelength, two adjacent peak/valley wavelengths in the reflection spectrum can be used to interrogate the FP cavity. By using Equation 2.2, the cavity length can be derived as

$$L = \frac{\lambda_1 \lambda_2}{2n_1(\lambda_1 - \lambda_2)} = \frac{\lambda_1 \lambda_2}{2n_1 FSR}, \tag{2.6}$$

where λ_1 and λ_2 are two adjacent resonance peaks or dips in the reflection spectrum. FSR denotes free spectrum range of the reflection spectrum. Assuming the FSR is significantly smaller than the peak/valley wavelength, Equation 2.6 can be simplified as

$$L = \frac{\lambda_1^{\ 2}}{2n_1 FSR}. \tag{2.7}$$

The change of cavity length can be deduced as

$$\Delta L = \frac{\sqrt{2}\lambda_2}{\lambda_1 - \lambda_2} \cdot \frac{L}{\lambda_1} \Delta \lambda_1. \tag{2.8}$$

When comparing Equation 2.8 with Equation 2.4, one can see that the traceable resolution of two adjacent peaks/valleys method is worse than that of peak/valley-tracking method.

Besides the reflection spectra of Fabry-Pérot interferometers, the intensity of the reflected light can also be explored to obtain FP cavity information and demodulate the signals.

Assuming I_0 is the incident light intensity, R_1 is the reflectivity of one reflective surface, R_2 is the reflectivity of another reflective surface, the reflected light intensity of the FP cavity is given by [49]

$$I = \alpha_0 \frac{R_1 + \eta R_2 - 2\sqrt{\eta R_1 R_2}\cos(4\pi n_1 L/\lambda)}{1 + \eta R_1 R_2 - 2\sqrt{\eta R_1 R_2}\cos(4\pi n_1 L/\lambda)} I_0, \tag{2.9}$$

where α_0 is a constant describing the optical loss owing to the lead in/out fiber and η is a coefficient of the intensity loss in the FP cavity.

The finesse of an optical resonator is an important factor which is defined as its free spectral range divided by its bandwidth (full width at half-maximum). The finesse factor is determined by the losses of the resonator and it can be defined as

$$F = \frac{\pi}{2\arcsin(\frac{1-\sqrt{\rho}}{2\sqrt[4]{\rho}})} \approx \frac{\pi}{1-\sqrt{\rho}}, \tag{2.10}$$

where ρ is the fraction of the left circulating power after one round-trip, and the condition for the approximation is that the round-trip loss of the optical cavity is low.

The finesse factor a FP cavity can be expressed as

$$F = \frac{\pi \sqrt[4]{R_1 R_2}}{1-\sqrt{R_1 R_2}}. \tag{2.11}$$

Equation 2.11 indicates that FP cavities with higher reflectivities of the reflective surfaces will have higher finesse values. In case a FP cavity has reflective interfaces with low reflectivities, the intensity of high order reflected light beams from each reflective surface become negligible and the a two-beam interference model can be adopted. The reflected light intensity of a so called low-finesse FP cavity is given by

$$I = \alpha_0 \left[R_1 + \eta R_2 - 2\sqrt{\eta R_1 R_2} \cos(4\pi n_1 L / \lambda) \right] I_0. \qquad (2.12)$$

From Equation 2.12, it can be seen that the reflection spectra of low-finesse FPIs present sinusoidal waveforms as shown in **Figure 2.1 (d)**. For a certain wavelength, the reflected light intensity depends on the cavity length of the FPI and the refractive index of the medium filled in the cavity. As a result, external stimulus which either alter the cavity length or change the refractive index of the medium can be detected by monitoring the intensity of reflected light of a FPI. Take a diaphragm-based FPI acoustic sensor for example, the acoustic pressure applied on the sensor induces deflection of the diaphragm, thus changing the cavity length of the FPI. The reflected light intensity for weak sinusoidal acoustic pressure can be expressed as [50]

$$\Delta I = 2 I_0 \gamma \frac{4\pi}{\lambda} \Delta L \sin(\omega t), \qquad (2.13)$$

where γ is the fringe visibility of the FPI, ΔL is the amplitude of pressure induced cavity length variation, and ω is the angular frequency of the excitation sound wave. Equation 2.13 shows that the variation of reflected light intensity has a linear relationship with the change of cavity length. Acoustic pressure can be detected by interrogating the alternating current (AC) components of the output signal from a photodiode (PD), which can convert light signals to electric signals. Since the response time of commercially available PD can be very short (in the range of nanoseconds), intensity-based demodulation method is suitable for the detection of rapidly changing signals such as ultrasonic waves.

2.2.2 Fabrication techniques

a) Transfer and assembly

Transferring microscopic sensing elements to the optical fiber tip and then assembling is an effective and versatile technique which inherits the benefits of fabricating on planar substrates, and meanwhile avoids the problems caused by the special geometry of fiber tip. This technique is widely used in the development of optical fiber-tip pressure sensors based on Fabry-Pérot interferometers, which consist of an air cavity and an elastic diaphragm transferred to the end-face of an optical fiber. Sleeves such as capillary tubes and ceramic ferrules are usually employed to support the reflective membrane and define the Fabry-Pérot cavity. Besides, sleeves provide both protection for the optical fiber and path for alignment. Optical fibers are carefully inserted into the sleeves and the gap distance between fiber tip and the diaphragm is precisely controlled. As shown in **Figure 2.2 (a)**, the first tip mounted fiber-optic pressure sensor was demonstrated by Wolthuis *et al.* via transferring a pressure sensitive silicon diaphragm to a glass tube in 1991 [51]. In 1999, a ceramic ferrule was used as the sleeve and a cooper diaphragm was transferred as the sensing element [52]. Since then various kinds of membranes have been transferred to the fiber tip for pressure/acoustic sensing, including silica [48, 53], silicon [54], silver [55-59], stainless steel [50], chitosan [60], Parylene-C [61], graphene [62-65],

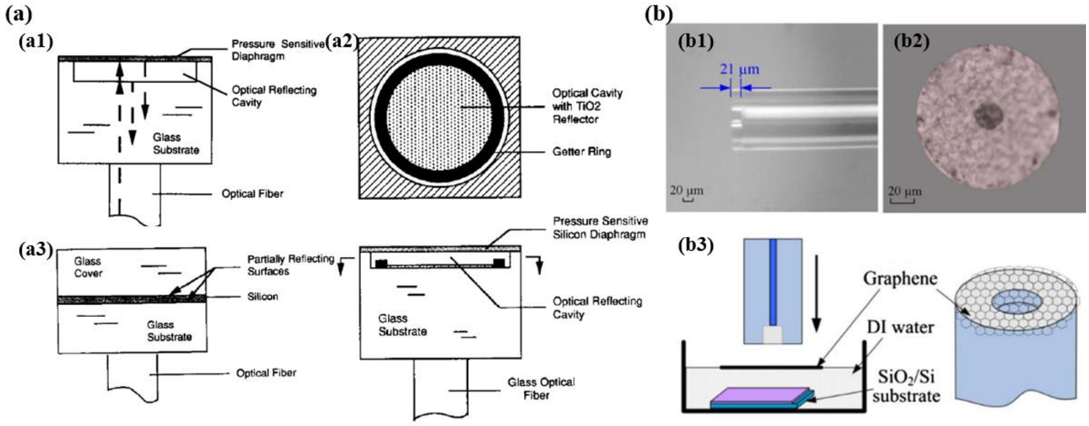

Figure 2.2 (a) The first fiber-optic pressure and temperature sensors based on tip mounted thin film. (a1) depicts the schematic of the FPI based pressure sensor. The sensor configurations for pressure and temperature detection are illustrated in (a2) and (a3), respectively. Adapted from Ref [51]. (b) Highly sensitive fiber tip pressure sensor based on graphene diaphragm. (b1) shows the microscope image of a standard single mode fiber with a capillary fusion spliced to its tip. A nanometer-thick graphene was transferred to the fiber tip as shown in (b2) by the method illustrated in (b3). Adapted from Ref [65].

graphene oxide [66], MoS_2 [67], silk fibroin [68], and so on. It's known that the pressure sensitivity of a FPI sensor with edge fixed circular diaphragm can be expressed as [69]

$$S = \frac{\Delta L}{\Delta P} = \frac{3(1-v^2)}{256} \cdot \frac{D^4}{Et^3}, \tag{2.14}$$

where ΔL is the deflection of the central point of the diaphragm, ΔP is the applied pressure, D is the diameter of the circular diaphragm and t is its thickness, v and E represent the Poisson ratio and Young's modulus of the diaphragm, respectively. Equation 2.14 indicates that for a fiber-tip diaphragm-based pressure sensor where the dimeter of the diaphragm is limited, the mechanical property and thickness of the diaphragm are vitally important for enhancing the sensitivity, *i.e.*, a diaphragm with smaller thickness and higher Young's modulus will result in higher pressure sensitivity. In 2012, Jin *et al.* transferred a nanometer-thick few-layer graphene diaphragm to the fiber-capillary tip [65], as shown in **Figure 2.2 (b)**, and achieved ultrahigh pressure sensitivity of 39.4 nm/KPa owing to that the Young's modulus is as high as 1 TPa [70] whereas the thickness of a single layer graphene is merely about 0.355 nm [71]. In the next year, the same group demonstrated an ultrasensitive ferrule-top acoustic sensor by the adoption of ~100-nm-thick multilayer graphene diaphragm with a pressure sensitivity of 1100 nm/KPa and a noise equivalent signal level of ~60 $\mu Pa/Hz^{1/2}$ [62]. The improved pressure sensitivity is due to the increasement of diaphragm's diameter.

Despite that commercially available capillary tubes and ceramic ferrules are convenient and low-cost, the feature size of these sleeves is still too large for miniature fiber-tip sensors, *e.g.*, the diameter of a ceramic ferrule is about 3 mm. Hill *et al.* reported a FPI pressure sensor consisting of a photolithographically patterned SU-8 cap mounted to the tip of an optical fiber [72]. By utilization of multiple photolithography, the polymer sleeve and deformable membrane are integrated together, as a result, the outer diameter of the sensor is reduced to 300 μm. Methods for fabrication of miniature fiber-top cavity have been reported by using commercial fusion splicers [55, 65, 73, 74]. By fusion splicing a section of capillary tube with a single-mode fiber and then cleaving a certain length of the capillary, a cavity with desired length can be readily fabricated as shown in **Figure 2.2 (b1)**.

b) Conformal coating of polymer films

Spin coating is a well-established and widely used deposition technique in micro/nano-fabrication where planar substrates such as silica wafer are the targets to be coated. When it comes to the fiber tip, the quality of the polymer film prepared by spin coating degrades, *i.e.*, curved surface and nonuniform coatings will occur because centrifugal forces produced by the spinning of substrate are insufficient to overcome the viscosity of the polymer solution on the small area of fiber tip where surface tension dominate the profile of the droplet. Efforts have been made to modify the spin coating process for the adoption of this technique on the fiber tip [75-77]. With a specially designed chuck which vertically fixed the optical fiber, Prasciolu et al. realized the deposition of poly methyl methacrylate (PMMA) thin film on the fiber tip via spin coating [76]. Uniform thin film with thickness around several hundred nanometers have been achieved by using spin coating [77-

79]. Sleeves such as ceramic ferrule are usually adopted to increase the area of the end-face, which can improve the quality of the film. Other deposition techniques such as dip coating [26, 80, 81], spray coating [82], dip and vibration coating [83], and thermal evaporation [84] have been proposed for conformal coating of polymer films on the fiber tip.

Dip coating is a simple and cost efficiency method for the deposition of thin polymer film on fiber tips. By immersing the fiber tip into polymer solution and then evaporating the extra solvent, polymer film with uniform thickness on the fiber tip can be obtained. The profile of the film is determined by surface tension and viscosity of the liquid polymer. By the adoption of polymer solution with lower concentration, which has lower viscosity, one can get films with smaller thickness and curvature. In addition, with the help of sleeves, the area of the end-face increases, resulting in better planarization of the polymer film. Normally films of thickness around several micrometers can be acquired via this method [80, 81]. Thicker films with larger curvature or even spherical cap can be realized by either increasing the viscosity of the polymer solution or multiple implementation of dip coating method. A spherical cap was fabricated on the end-face of a standard single-mode fiber by dip coating UV-curable polymer followed with UV polymerization [85]. The fiber-tip polymer cap can play a role as a plano-concave optical microresonator with high quality factor over 10^5, as a consequence, an ultrahigh sensitivity of 1.6 mPa/$Hz^{1/2}$ and a broad bandwidth of 40 MHz have been achieved. The strong confinement is due to the curvature of the spherical cap, which refocuses the diverging beam back into the FP cavity and prevents the light from lateral leaking, and the high reflectivity of the mirrors. This case indicates that dip coating method is capable of producing smooth polymer surface with high reflectivity.

Based on dip coating method, the dip and vibration technique can dramatically reduce the thickness of the polymer film to ~100 nm with good repeatability [83]. After dip coating process, a vibration of the fiber tip is introduced to remove the redundant polymer solution, which significantly reduce the thickness and curvature of the eventual film. The distance between the free fiber tip and the clamping point is controlled, meanwhile the initial displacement of the fiber tip to trigger vibration is fixed, thus guaranteeing the repeatability of the film thickness.

Spray coating is a novel deposition technique with remarkable advantages such as high utilization efficiency of materials, wide applicability to substrates with various size and geometry, which is especially suitable for coating the fiber tip. A nozzle is employed to atomise the polymer solution and then deposit it on the substrate uniformly. It has been demonstrated that thin film with thickness of around 5 μm was deposited on the fiber tip through spray coating [82].

c) Thermal reflow

Thermal reflow is a process in which initial patterns are reshaped into destination profiles by heating up the material to a threshold temperature. Surface tension will drive the melt material to relocate into a certain shape determined by surface energy, wettability and adhesion of the material, and finally define the shape of the solidified material after cooling down [86].

Polymeric materials are often processed by thermal reflow to develop fiber-tip sensors. Gang *et al.* demonstrated a fiber-tip FPI ultrasonic sensor with a semispherical cap fabricated by thermal reflow of polyvinyl chloride (PVC) diaphragm [87]. A plastic welder with temperature control was used to heat the polymer thin film, and the optimized heating temperature and time is 300 °C and 20 seconds, respectively.

The native material of optical fibers, *i.e.*, silica, can also be treated with thermal reflow to create simple 3D topographies such as microspheres. Compared with polymer, the glass transition temperature of silica is much higher (~1200 °C), thus CO_2 laser, arc discharge or microburner is chosen to melt the fiber tip. Surface tension will relocate the melt silica into a sphere, as a result, silica microsphere on the fiber tip can be readily obtained after cooling. Bulb-lens for emitted light collimation have been fabricated on the fiber tip by using thermal reflow and the device can work as a vibration sensor [88]. Silica microspheres has also been implemented on the fiber tip as a WGM resonator with high quality factor [89], which indicates the surface of the microsphere fabricated by thermal reflow is very smooth.

d) Chemical etching

Chemical etching can be employed to either intrinsically pattern the material of fiber tip or extrinsically process sensing elements. Microwells have been fabricated on the fiber tip by etching doped glass for fluorescence and SERS sensing [90, 91]. In the fabrication of all-silica diaphragm-based FPI sensors, hydrofluoric acid is used to etch the diaphragm so as to reduce the thickness of the film [48]. Moreover, a 750 nm-thick silica diaphragm originated from the thermal oxide layer of a silicon wafer can be obtained by etching away the silicon [53].

e) Through fiber pattering

A polymer tip can be readily fabricated by simply immersing the optical fiber tip into photosensitive polymer solution and then launching light with proper wavelength into the fiber. Polymer cured by the guided light can extend to several hundred micrometers due to self-guiding effect of the polymer, *i.e.*, the refractive index of the photosensitive material increases as it's polymerized, thus contributing to the collimation of the light beam [92]. The topography of the polymer tip, to a certain degree, can be tuned by tailoring exposure conditions, properties of the guided light and photosensitive material [93-95].

Since the first demonstration of through fiber pattering in 1974 [96], this technique has been developed over the decades and found applications ranging from light coupling [97, 98] to sensing [99-101]. Polymer tips with flat end-face can be fabricated by imposing a boundary to restrict the self-guiding photopolymerization process, which have been used to from FP cavities for distance measurement [99] and refractive index sensing [100].

2.2.3 Sensing applications

Conventional optical fiber-tip FPIs fabricated by techniques described above have been widely employed in various sensing applications including the detection of temperature [102-104], pressure [53, 57, 61, 65, 68, 72, 85], RI [100, 105, 106], humidity [107-109] and biochemical measurands [110-112]. Ultrasonic sensors based on fiber-tip FPIs can date back to 1996 when a polymer thin film was transferred to the end-face of an optical fiber to form a FP cavity, and the diaphragm's thickness change induced by acoustic waves was interferometrically detected [113]. The sensor showed a comparable sensitivity with that of polyvinylidene difluoride (PVDF) membrane-based ultrasound sensor, and the noise floor was 2.3 KPa with 25 MHz bandwidth. With the development of material science, thinner diaphragms with enhanced mechanical strength have been adopted to improve the pressure sensitivity, *e.g.*, graphene diaphragm based acoustic sensor exhibits noise equivalent signal level of ~60 $\mu Pa/Hz^{1/2}$ [62]. By the adoption of functional material, Polyvinyl alcohol (PVA) film, whose effective RI decreases and thickness increases when absorbing water, Su *et al*. demonstrated fiber-tip humidity sensor with a sensitivity of 0.07 nm per 1% relative humidity [109]. In addition, a polyvinyl alcohol (PVA)/poly-acrylic acid (PAA) film was coated on the fiber tip to form a miniature pH sensor [111], which made use of the swelling effect of the responsive film, *i.e.*, the optical path of the FPI changes when the film is immersed in solutions with different RI values. Moreover, Tierney *et al.* proposed fiber-optic glucose probes by coating the fiber tips with carbohydrate sensitive hydrogels [110]. Owing to the incorporation of novel functional materials as the sensitive diaphragms, optical fiber-tip sensors based on FPIs with new functionality and improved performance have been developed.

2.3 Optical fiber-tip sensors based on fiber-top microstructures

With the rapid development of modern micro/nano-fabrication technology, unprecedented manufacturing resolution and 3D fabrication capability have been achieved, which provides exciting opportunities for the development novel optical fiber-tip sensors based on sophisticated microstructures requiring high processing accuracy. The sensing mechanisms of these sensors are consistent with those discussed in section 2.2.1. The fabrication techniques are emphasized in this section, meanwhile the applications of optical sensors based on fiber-top microstructures are reviewed.

2.3.1 Fabrication techniques

Many micro/nano-fabrication techniques have been employed to implement microstructures on the fiber tip. Several representative techniques are introduced as below, and a brief discussion about the advantages and drawbacks of each method is given. Detailed reviews on the fabrication techniques for fiber-top sensors and devices can be found in the literature [18, 47].

a) Focused ion beam milling

Focused ion-beam (FIB) milling makes use of a high-energy focused beam of ions such as gallium to strike the target sample, ablating and machining materials at micro- and nanoscale according to predesigned path. Modern FIB systems can provide spot sizes of less than 5 nm, which guarantees ultrahigh resolution. FIB milling is capable of carving the native material of optical fibers, *i.e.*, silica. Lenses have been directly engraved on the fiber tips by carefully controlling the processing conditions [30, 114-116], and a smooth surface with 3.6 nm roughness has been achieved [114]. Microprisms have also been fabricated on the cores of optical fibers via this technique to alter the light beams for optical trapping and manipulation [43]. Besides silica, metallic materials can also be patterned by the adoption of FIB milling, which allows for the development of fiber-tip resonant plasmonic sensors and devices based on metallic nanostructures. The demonstrations of fiber-tip plasmonic sensors or SERS probes fabricated by FIB milling can be found in the literature [37, 40, 117, 118].

Iannuzzi *et al.* have demonstrated that silica cantilevers can be directly fabricated on the fiber tips by FIB milling for monolithic sensors [23, 119, 120]. **Figure 2.3 (a)** depicts the main steps for the carving of a fiber-top cantilever. A bridge with both ends clamped was fabricated at first as shown in **Figure 2.3 (a1)–(a3)**, followed by the reduction of the beam's thickness as depicted in **Figure 2.3 (a4)**. Then a pyramid tip, as shown in **Figure 2.3 (a5)**, was carved on the cantilever for applications such as atomic force microscope (AFM) where the tip would scan the surface of the targets as a probe. Finally, the supporting anchor under the pyramid tip was removed as shown in **Figure 2.3 (a6)**. As the cantilever is right above the fiber core, deflection of the cantilever beam induced by external stimulus, or the vibration in cavity length, can be readily interrogated by interferometry as illustrated in **Figure 2.3 (b)**. The implementation of AFM has been demonstrated by the adoption of such fiber-top cantilevers [119], and performance comparable to that of commercial AFM systems has been achieved when the fiber-top AFMs are working in contact mode. Output signal acquired from a fiber-top AFM scanning a calibration grating is shown in **Figure 2.3 (c)**. Based on similar fiber-top microstructures and readout apparatus, a variety of applications including refractive index sensing [121], hydrogen detection [122], pressure and humidity sensing [123], and biosensing [124] *etc.* have been reported.

The major drawbacks of FIB milling include inevitable ion doping into

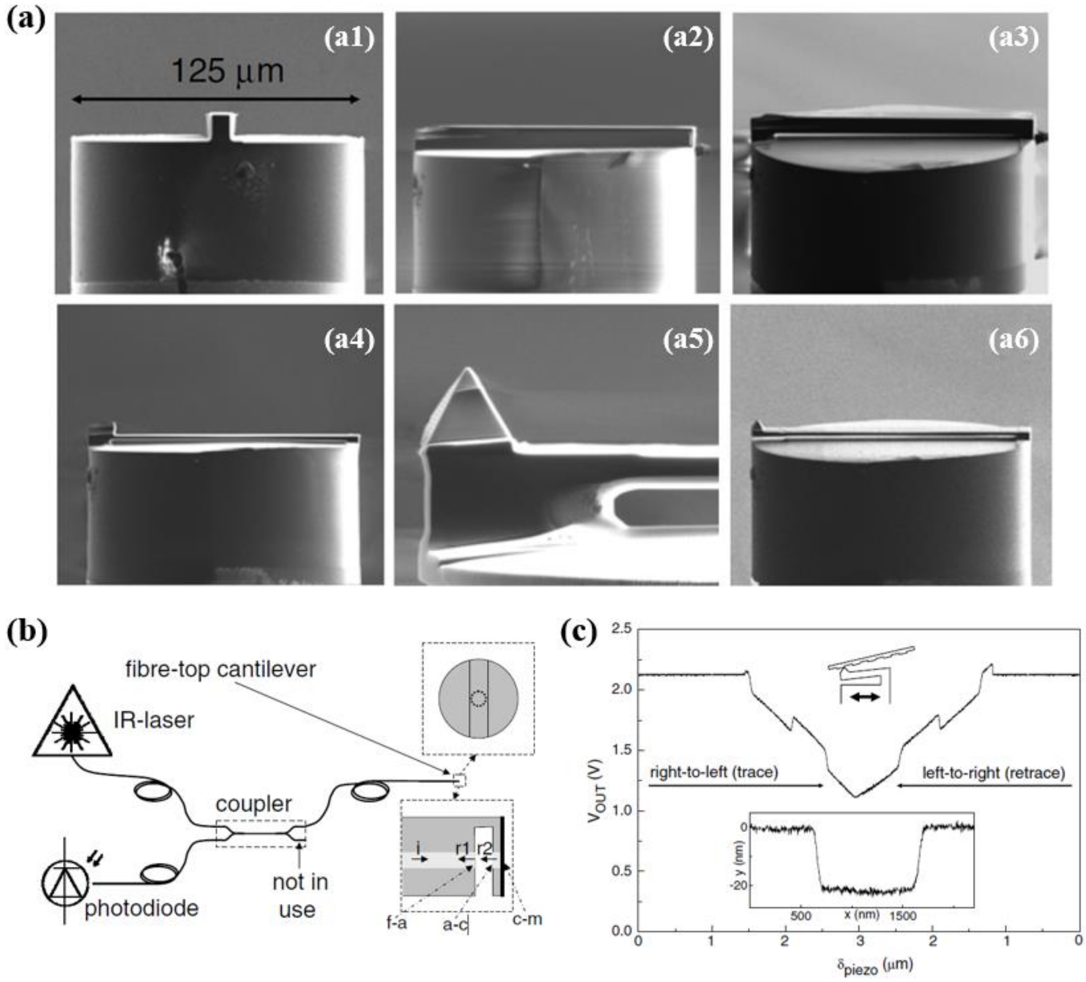

Figure 2.3 (a) Micrographs showing the major fabrication procedures to carve a fiber-top cantilever. (b) Schematic diagram of the readout apparatus allowing for the interrogation of the cantilever beam's position. (c) Experimental results for the fiber-top AFM measuring a calibration grating in contact mode. Adapted from Ref [119].

the substrate and angled sidewalls of the etched wells [47]. Besides, the ultrasmall spot size results in time consuming fabrication processes and limited area which can be processed in one step, which restrict the potential for mass production. Moreover, the 3D fabrication capability of FIB milling is limited by the etching manner, which makes it difficult to process sophisticated microstructures such as sealed cavities. Last but not least, the expensive apparatus prevents the wide application of this technique.

b) Femtosecond laser ablation

Similar to FIB milling, femtosecond laser ablation takes advantage of focused femtosecond laser pulses with high energy instead of ion beams to micromachine surface materials. The cost is generally lower and processing speed is faster than those of FIB milling, whereas the surface of the processed areas are usually rougher [125]. This technique has been employed to fabricate Fresnel zone plate lens [126], surface gratings [127] and SERS probes [32, 128].

Iannuzzi *et al.* has utilized femtosecond laser to fabricate fiber-top cantilevers in a two-step process [125]. Firstly, femtosecond laser scanned the area to be etched of the fiber in a predefined pattern. The laser energy at the focal volume was optimized to alter the chemical property of glass without ablating it. After exposure, the fiber tip was immersed into HF with low concentration for chemical etching. The patterned area had higher reactivity to acid due to femtosecond laser illumination, thus it was etched faster than the rest part of the fiber.

Compared with FIB milling, femtosecond laser ablation provides a cheaper, faster and more convenient method to micromachine fiber tips. However, the surface quality of the patterned area and fabrication precision degrade.

c) Photo lithography

Photo lithography is a well-established and widely used technique to pattern arbitrary 2D micro-/nano-structures in both industry and research community. A photomask is usually employed to modulate ultraviolet (UV) light into predefined pattern, subsequently the pattern is transferred to the photosensitive materials through UV exposure. State of art photolithography apparatus can offer nanoscale resolution. Problems occur when the flat tip of an optical fiber becomes the substrate because the large aspect ratio of optical fibers is not suitable to the commonly used contact mask aligners, which is originally designed for planar substrates such as silica wafer.

Attempts have been made to overcome the incompatibility. Fiber wafers have been created by binding a cluster of optical fibers with epoxy, followed by cleaving and polishing [129]. Sasaki *et al.* proposed a self-aligning method where conventional mask aligner was abandoned [82]. A specially designed mask with mechanical alignment guide was fabricated by electroplating and utilized for both alignment and pattern transfer. Commercial fusion splicers have been employed to assist the alignment [26].

Two optical fibers are mounted in a fusion splicer, while one fiber is coated with photoresist on its tip, and another UV transparent fiber with metallic 2D microstructures patterned by FIB milling plays a role as a photomask. The alignment and approaching are completed automatically by the fusion splicer and then UV light is launched into the mask fiber for pattern transfer.

Although techniques described above have solved certain issues in the adoption of photolithograph on the fiber tip, inconvenient procedures such as the fabrication of fiber wafers and customized photomasks still limit the application of photolithography on directly patterning the fiber tip.

d) Interference lithography

The inference patterns created by multiple coherent light waves have been utilized to produce large areas of regular arrays of periodic features with naonoscale resolution. Interference lithography allows nano-fabrication of periodic structures in all three dimensions without the need for expensive apparatus and photomasks. The resolution of interference lithography is limited by the diffraction limit of the laser beam, which becomes the major shortcoming of this technique.

The adoption of interference lithography for fiber-tip patterning can trace back to 1999 when Tibuleac *et al*. fabricated diffraction gratings with submicrometer period on the fiber endface [130]. Waveguide grating-structures has been implemented on the fiber tip [28], where a layer of ZnO deposited on the polished fiber endface functioned as the waveguide while a photoresist grating with 425 nm period was fabricated on the waveguide by using interference lithography. Besides gratings, two-dimensional interference patterns have been employed to fabricate fiber-top nanopillars array for SERS sensing [75]. Firstly, A two-dimensional photoresist nanopillar array with 317 nm pitch and 160 nm diameter was patterned by interference lithography, which would serve as a shadowmask in the following etching process. Then a deep reactive ion etching method was adopted to carve the silica material of optical fiber into periodical nanopillars array. Finally, the residual photoresist was removed, and a layer of silver was deposited onto the nanopillars.

Different from conventional interference lithography where bulk optics are usually employed to generate interference patterns, Kim *et al.* proposed a compact optical fiber device to generate concentric interference patterns and further utilized the patterns to engrave surface relief gratings on the fiber tip [78]. A short section of coreless silica fiber was fusion spliced to a standard single-mode fiber, which would expand the fundamental mode exiting from the single-mode fiber. A portion of the beam propagating in the coreless fiber encounters the silica/air interface and reflects back into the fiber, whereas the other part reaches the endface of the core less fiber directly, thus inducing interference patterns. By adjusting the length of the core less fiber, the pitches of the concentric interference patterns can be tuned.

e) Electron beam lithography

In contrast to photolithography, a focused beam of electrons instead of light is employed to pattern electro-sensitive resist which can be selectively dissolved by the developer after exposure. Arbitrary two-dimensional geometries can be realized as electron beam lithography (EBL) works in a serial writing manner. The main advantage of EBL over photolithography lays on its ultrahigh resolution, *i.e.*, sub-10 nm, whereas the diffraction limit of light restricts the smallest feature size photolithography or interference lithography can achieve. The ultrasmall beam width and direct-writing manner decide that the throughput of EBL is low. Besides, the cost of establishing an EBL system is very high, for example, the price for a dedicated EBL system is over 1 million US dollars and a cheaper system reformed from an electron microscope for research and development can still cost 100,000 US dollars. Both the large costs and low throughput limit the usage of EBL to areas such as the fabrication of photomask, prototype devices and research.

The fiber tip micro- and nanostructures patterned by EBL have been exploited to develop photonic sensors and devices. Multilevel phase diffractive elements with 3D profiles fabricated by EBL have been implemented on the fiber tip to realize efficient fiber-waveguide coupling

[76]. A gray-scale exposure manner has been adopted to create 3D feature, *i.e.*, the exposure dose for each pixel of the pattern is calculated and precisely controlled, which results in different cured depths for corresponding unit areas. By depositing metallic materials to nanostructure fabricated by EBL, fiber-top localized surface plasmon resonance (LSPR) devices have been developed for refractive index and acoustic sensing [79].

The patterned resist is more often utilized as a sacrificial layer which will serve as a shadowmask in the following processes and be removed eventually, whereas the nanostructures are transferred to the substrate materials by means of etching or deposition. The selective deposition is usually accomplished by the lift-off technique which originates from conventional microelectromechanical systems (MEMS) technology. In brief, materials are deposited onto the EBL defined resist patterns and then the resist is removed by proper solvent together with the materials deposited on it, leaving behind materials deposited directly on the substrate. The etching method works in an inverse manner where resist patterns are fabricated on a film of the target material and protect the covered region in the following etching process, as a consequence, the target material exposed to the corrosives is removed whereas the other part underneath the resist pattern remains. Nanoholes array in metallic coatings with diameters ranging from 100 nm to 700 nm have been fabricated via EBL and lift-off technique to investigate the behavior of light transmission through these arrays [77]. With an etching process following EBL, nanostructures such as gold nano-grids [83], nanodots [29, 34], and concentric rings [131] have been produced on the fiber tips for various applications from ultra-wideband polarizers to refractive index sensors.

It's noteworthy that unlike silicon wafer, the material of optical fibers, *i.e.*, silica, is an electric insulator which prevents electrons from dissipation, thus leading to an issue of electrostatic charging of the fiber. To solve this problem, an additional conductive layer consisting of conductive polymer [83] or metal [76, 79] is deposited onto the resist, which will guide the charges to ground during the EBL process.

f) Two-photon direct laser writing

In the past few decades, direct laser writing (DLW) technique based on multi-photon absorption process has attracted remarkable attention due to its superior 3D micro- and nanofabrication capability over techniques described above such as FIB milling, femtosecond lase ablation and EBL. In this section we focus on two-photon polymerization (TPP) based direct laser writing technique which has been widely employed in 3D micro- and nanostructures fabrication.

Two-photon absorption is a non-linear process which requires high light intensity so that a pulsed laser with high peak power is usually focused onto the photosensitive materials. The photoresist and the wavelength of laser source are carefully selected according to a general rule that the photoresist is transparent to the laser source's wavelength λ whereas it absorbs light at the wavelength at λ/2. As a consequence, only the photoresist located at the focal spot of the laser beam will undergo polymerization during illumination.

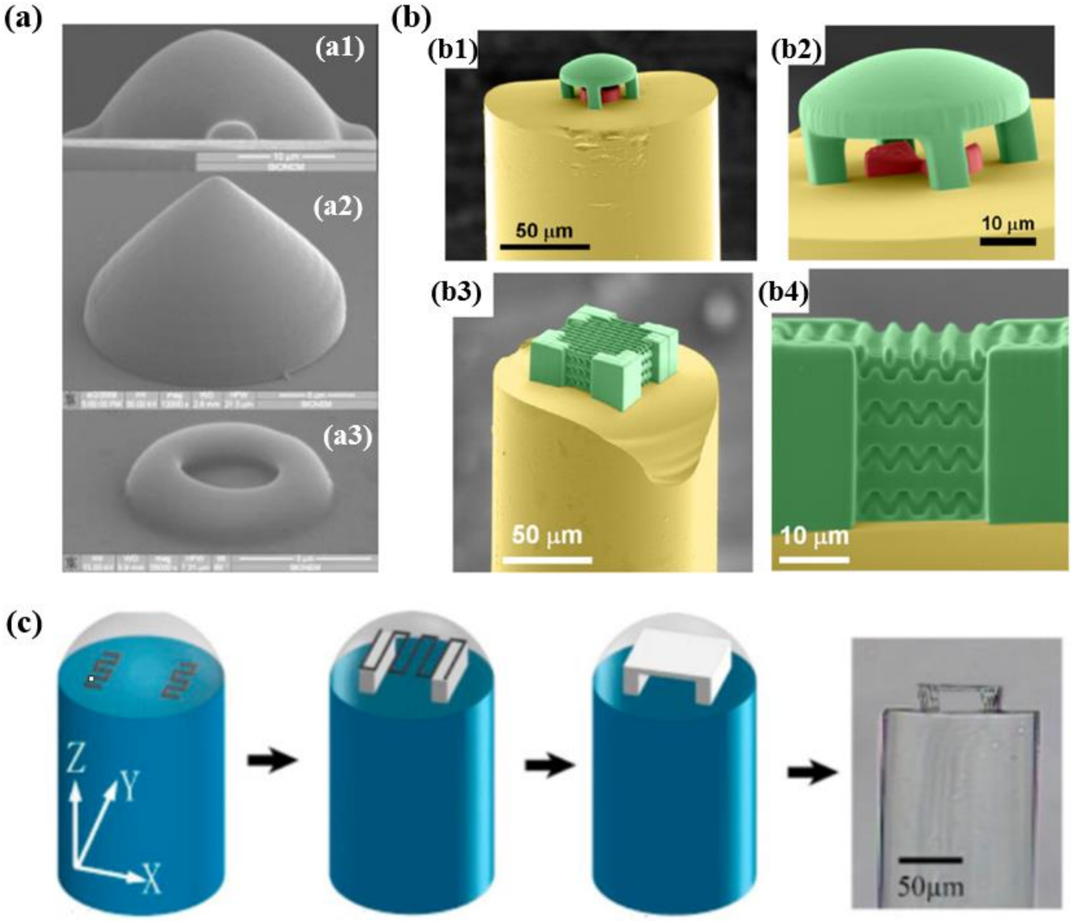

Figure 2.4 (a) SEM images of convergent lens (a1), axicon lens (a2), and ring (a3) fabricated on the fiber tips by two-photon DLW. Adapted from Ref [145]. (b) False color SEM images of fiber-top micro-optics systems and three-dimensional photonic crystals fabricated by DLW. Adapted from Ref [31]. (c) Fabrication processes of a fiber tip acoustic sensor consists of a suspended diaphragm fabricated by DLW. Adapted from Ref [148].

By scanning the focal spot in three-dimensional space, arbitrary 3D geometries can be created after subsequent development. Resolution beyond the diffraction limit, *i.e.*, 100 nm or even better, can be achieved due to the nonlinear two-photon absorption process and the threshold behavior [132]. More content about the origin and development of two-photon polymerization can be found in the literature [133-135].

Two-photon DLW's capability of fabricating complicated 3D structures has enabled the development of all kinds of fiber-top devices including a diversity of lens [136-138], free-form optics [139], micro-photonic systems [31], suspended beams with both ends fixed [140], Fabry-Pérot cavities [141-143], 3D radar-like SERS probe [144], and springs [145]. **Figure 2.4 (a)** shows the scanning electron microscope (SEM) images of several fiber-top microstructures fabricated by two-photon DLW including **(a1)** convergent lens, **(a2)** axicon lens and **(a3)** ring which can be used as a phase mask. More sophisticated fiber-top microstructures constituting micro-optic systems are shown in **Figure 2.4 (b)**. A plano-concave lens was fabricated on the fiber tip while another plano-convex lens with larger radius was suspended right above it, as shown in **Figure 2.4 (b1)–(b2)**. A well-known three-dimensional photonic crystals structure, "woodpile", was also demonstrated as shown in **Figure 2.4 (b3)–(b4)**. The fabrication process for a fiber-top suspended diaphragm with both ends mounted is shown in **Figure 2.4 (c)**, which clearly illustrates the serial writing manner of two-photon DLW. The deformable diaphragm was employed as an acoustic sensor in a similar approach with those elastic diaphragm-based sensors described in Section 2.2, however, the geometries of the suspended membrane can be precisely tailored through DLW and there is no need for an additional sleeve, which contributes to the implementation and miniaturization of fiber-top sensors.

g) Nano-transferring

The basic idea of nano-transferring is similar to the micro-transferring technique introduced in Section 2.2.2, *i.e.*, fabricating nanostructures on planar substrates first with regular nanofabrication platforms and then transferring them to the fiber tips. The transferring step is vitally important for the quality and overall yield of the final devices because flaws or damage can be easily introduced to the well patterned nanostructures during this process due to improper operation [47].

Nano-transferring is commonly accomplished by stripping off the film containing nanostructures from the planar substrate and then attaching the film to the fiber tip with the help of a micropositioner or by pressing the fiber tip into the film floating on water. With the deposition of metallic nanostructures upon fiber end-surface, optical probes based on SPR or SERS can be developed for sensing applications. Smythe *et al.* has demonstrated the adoption of nano-transferring technique to relocate metallic nanostructures patterned by EBL to the fiber tip where a sacrificial polymer film is employed to strip the nanostructures from silica wafer [146]. The sacrificial layer that supports the nanostructures during the transfer process is finally removed by oxygen plasma, leaving behind metallic nanostructures on the fiber tip, which is subsequently employed as a SERS probe. A limitation exists in this approach that the adhesion between nanostructures and the substrate cannot be too strong to strip. To eliminate this limitation, the same group proposed a more convenient and universal method by incorporating a process called nanoskiving, where an ultramicrotome was utilized to slice epoxy nanopost array coated with gold [147]. The nanopost array was embedded in epoxy before sectioning, and then slabs containing nanostructures was transferred by dipping the fiber tip in water. After the removal of epoxy, several types of metallic nanostructures were successfully transferred to the fiber end-face.

In another approach, a drop of epoxy is delivered to the fiber tip as an adhesive layer which will release the nanostructures from substrate after the epoxy cures [24, 148-151]. More strategies about nano-transferring can be found in the literature [152, 153].

h) Self-assembly

Self-assembly (SA) is a powerful bottom-up nanofabrication technology which provides an easy and cost-effective access to the nano-regime [154].

Although the manufacturing precision and geometrical control capability of SA method are limited, it's suitable to unusual substrates such as fiber tips. Besides, high vertical resolution can be achieved in layer-by-layer SA. The first application of SA on fiber tips can date back to 1998 when the end-face of optical fiber was decorated by SA for the investigation of SERS performance [38]. Over the past few decades, new sensor designs with more complicated structures and enhanced performance have emerged and can be found in the literature [155-159].

2.3.2 Sensing applications

A variety of sensing applications based on fiber-top micro- and nanostructures have already been introduced during the review of fabrication techniques. To summarize, physical sensors which detect parameters such as pressure [123], refractive index [160], force [124], velocity [161], *etc*. have been implemented on the fiber tips. Miniature fiber-tip sensors have also found applications in biomedicine where in vivo interrogations of cells and organisms with minimal damage are guaranteed [19, 162]. In addition, various fiber-tip sensors based on plasmonic resonance or SERS have been developed [24, 25, 35, 38, 163, 164]. The incorporation of micro- and nanostructures not only offer opportunities for novel sensor designs, but also contribute to the improvement of sensing performance.

2.4 Optical 3D μ-printing technology

In Section 2.3, several micro- and nanofabrication techniques commonly used to pattern the end surface of optical fiber for the development of sensors have been reviewed. Each technique has its advantages and shortcomings. Besides the incompatibilities between fiber tips and some fabrication platforms and the fact that certain techniques lack for 3D fabrication capability, there is always a tradeoff between precision and throughput. To overcome the limitations in current fabrication technologies, we develop an optical 3D μ-printing technology which suits microfabrication on the fiber tip. The manufacturing speed is fast compared with EBL or FIB milling, while a considerable resolution can be achieved. Fiber-top microstructures have been fabricated via this own-developed technology for sensing applications.

2.4.1 DMD-based optical maskless lithography

Photolithography is a mature and widely used micro-nano fabrication technique in both industry and research. Selective exposure of photosensitive polymers allows arbitrary 2D geometries to be defined in parallel and on the wafer-scale. State of the art photolithography systems are capable of nanoscale patterning. In large-scale integrated circuit manufacturing, photolithography technology is a key step which determines the smallest feature size and transistor density of the IC chip. The long evolution of the semiconductor industry has made the original contact-photolithography a ubiquitous and affordable technology, and therefore a mainstay of research laboratories around the world. Photolithography has been used to develop photonic sensors, especially fiber-tip sensors, however, there are some issues in employing this technique on optical fibers.

In typical photolithography processes, firstly a special mask is designed and fabricated, then UV exposure is used to transfer the pattern on the mask to the photoresist on the substrate after carefully alignment. Unfortunately, when then substrate becomes an optical fiber instead of silicon wafer, contact mask aligners are not compatible with the large aspect ratio of optical fibers. Although some strategies have been proposed to overcome this problem, it’s still inconvenient to directly use contact photolithography to pattern optical fiber tip or the curved surface. What’s more, the expensive fabrication cost of the mask and pollution problem in contact exposure manner also prevent the utilization of photolithography in the development of optical fiber sensors.

Proximity exposure and projection exposure technologies are developed to provide an alternative route to overcome the mask pollution problem of contact exposure. A step further leads to the so called maskless lithography technology, in which spatial light modulators (SLM) are usually employed to generate optical patterns. Gray-scale exposure is available by using maskless lithography since SLM can refresh the patterns at a high speed. A more exciting optical 3D μ-printing technology can be developed based on optical maskless lithography. Here we focus on DMD based optical 3D μ-printing technology.

2.4.2 Optical 3D μ-printing technology for fiber-top microstructures

Figure 2.5 shows the schematic of the optical 3D μ-Printing system. UV (365nm) beam coming from light source passes through the illumination optics and then illuminates onto the DMD chip. The light reflected from the DMD chip is modulated to an optical pattern which is previously uploaded to the DMD chip. After passing through the projection optics, the image on the DMD chip is finally projected onto the photoresist on the substrate.

UV lasers, UV lamps or UV LEDs can be used as the light source. We choose non-coherent light source (UV lamps) or partly coherent light source (UV LEDs) to avoid interference. A high-pressure mercury lamp, OmniCure® S2000 from Lumen Dynamics, whose emission light cover both UV (190 nm ~380 nm) and visible bands (380 nm ~770 nm), is used in our system. UV LED is another option for the light source due to its advantages of long lifetime and low power consumption. A UV LED, LC-C2, from Hamamatsu Photonics is also used in one of our systems Compared with UV lasers, the interference speckle effect is not obvious since light emitted by the UV LED is partly coherent.

The key component of the 3D μ-Printing system is the spatial light modulater (SLM). Liquid crystal display (LCD) was firstly used as the SLM in maskless exposure system, however, several drawbacks such as large pixel size, low filling rate, long response time and strong absorption in UV band limit its application. DMD, which is invent by Dr. Larry J. Hornbeck from Texas Instruments in 1987, has been widely used in digital light processing (DLP) systems because of its miniature size and high resolution. A DMD chip consist of millions of micron-sized micromirror, and currently the commercially available DMD chips have resolutions of 640 × 480, 800 × 600, 1024 × 768, 1280 × 1024, 1920 × 1080, 1920 × 1200 and 2560 × 1600. The arrangement of these micromirrors follows a two-dimensional matrix pattern, *i.e.*, in rows and columns. The filling rate of a DMD chip can is typically more than 90%, which is significant to the improvement of optical efficiency and quality of the generated patterns. Each individual micromirror can be addressed and controlled independently by the control unit, which is usually implemented by a Field Programmable Gate Array (FPGA) for research and development. In general, the micromirrors are driven by electrostatic force generated by the input voltage signal from the addressing electrodes, resulting in three possible states, *i.e.*, on state, off state, and reset

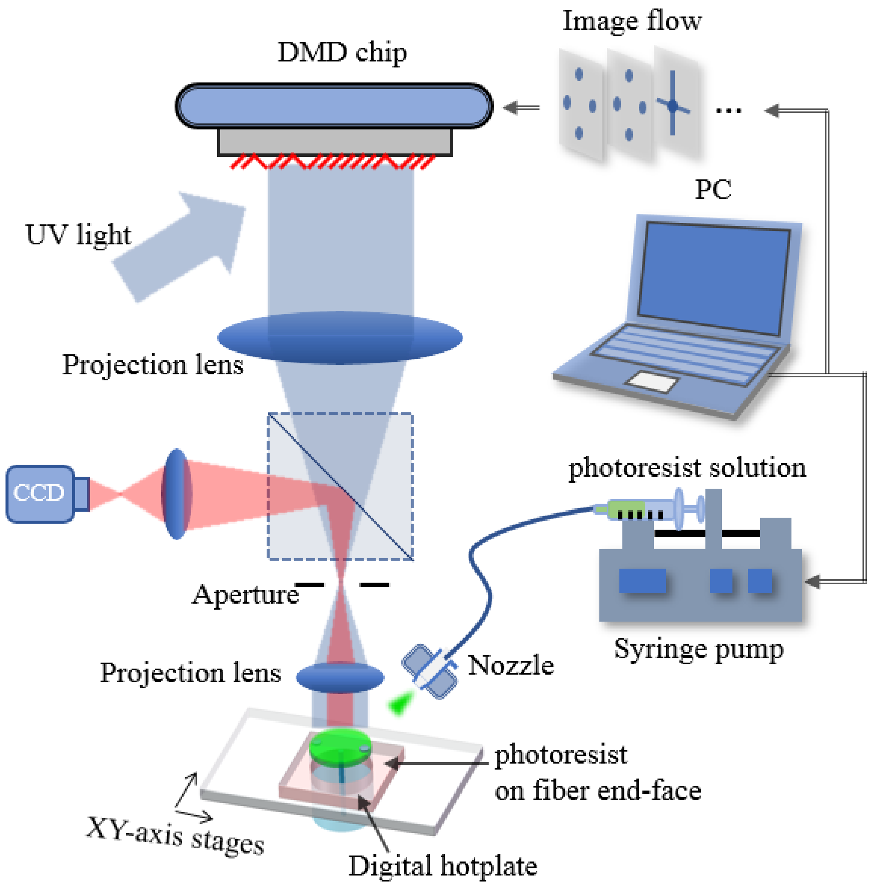

Figure 2.5 Schematic diagram of the optical 3D μ-Printing technology.

state, which are determined by the rotation of the micromirrors. The on state of a micromirror defined by high voltage (binary signal of "1") is implemented by a 12° rotation from the optical axis, where the light beam reflected from this micromirror propagates along the axis of the projection optics and thus can be collected by the projection optics. On the contrast, when a micromirror is turned into off state by low voltage (binary signal of "0") from the addressing electrode, the angle of its rotation is -12°, thus the light beam reflected by this micromirror walks off the accepting angle of the objective lens's aperture and can not be collected by the projection optics. The reset state is defined by the circumstance where no signal voltage is applied on the electrode. Based on the three states described above, arbitrary two-dimensional pattern can be generated by the DMD chip via controlling millions of micromirrors independently. The pitch sizes of commercially available DMD chips include 7.6 μm, 10.8 μm, and 13.7 μm, such small pixel size guarantees the fidelity of the patterns displayed by the DMD chip. After being scaled down by the projection optics, the size of smallest feature of the images generated by the DMD chip can be further reduced, which is competitive with photo masks. Besides resolution, accuracy and pixel size, another important parameter is the optical efficiency of the DMD chip, which is generally determined by factors such as reflectivity at the operation wavelength, filling rate of the micromirrors and response time. For our optical 3D μ-printing technology, the wavelength of the light source is 365 nm. DMD chips with reflectivity promotion layers for UV light are chosen, and the reflectivity for 365 nm is more than 90%. The filling ratio of micromirrors for commercial DMD is can reach up to 98%, which exceeds 56% of LCD and other types of SLMs. Owing to the light weight of micromirrors and the actuation method, the response time of DMD chip is typically shorter than 1 ms, which meets the demand of our application. Moreover, the contrast ratio is also an important factor which affects the accuracy of UV exposure dose distribution. Typical contrast ratio of DMD chip is 1000 : 1 and a high ratio of 2000 : 1 can be achieved through optimization of pixel structure, whereas the contrast ratio of LCD is below 700 : 1.

2.4.3 Fabrication process

The fabrication processes can be generally divided into three parts. Firstly, commercial software solidworks is used to design the 3D models of the structures to be printed. An own-developed add-on software is then used to slice the CAD model into layers of image data which will be uploaded to the DMD chip. Secondly, the substrate is deposited by photoresist. Thirdly, dynamic UV exposure of the photoresist and followed with develop. These processes will be introduced in detail as below.

2.4.3.1 3D modeling and data to graphic converting

3D models are firstly designed by using solidworks and saved as a common data format STL. **Figure 2.6 (a)** shows the 3D model of an array of cones deigned by solidworks. Then a commercial software Tecplot is used to open the 3D models for further processing. As shown in **Figure 2.6 (b)**, a cone is

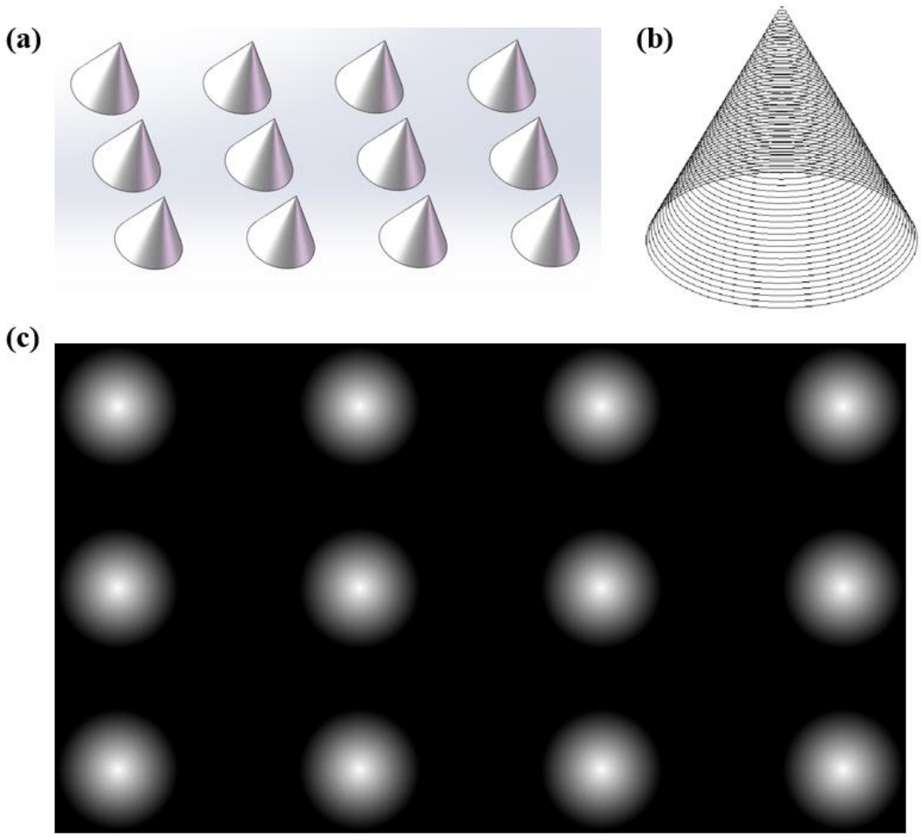

Figure 2.6 (a) 3D models of the micro cones to be printed. (b) A cone sliced into 50 layers by Tecplot. (c) BMP image generated by the add-on software.

sliced into 50 layers by using the Tecplot software. The add-on software based on Tecplot Application Programming Interface (API) is developed under visual C++ environment.

Firstly, a function provide by Tecplot is used to slice the 3D model into several layers and the coordinates of points which consist of the outline of each layer are provided. Interpolation is utilized to fill in the gap between the discrete points. Then the interior of each layer's outline is filled by using the so-called flood-fill algorithm. Each layer of the processed data corresponds to a 2D matrix, which eventually become one frame image uploaded to the DMD chip. Finally, the data matrix is exported either as gray-scale bitmap picture for visualization or own-defined data format, as shown in **Figure 2.6 (c)**.

2.4.3.2 Deposition of photoresist

In order to ensure the quality of micro/nano-fabrication, it is a vitally important step to deposit uniform thin layer of photoresist with well controlled thickness on the substrate. Spinning coating is a reliable deposition method for wafer scale substrates, where centrifugal forces compete with the viscosity of the liquid polymer. However, when the substrate is the flat tip of an optical fiber, surface tension can dominate to create curved and non-planar coatings. New deposition techniques are in demand to coat the fiber tip with high quality photoresist film.

Dip coating is a simple and effectively method when the desired thickness of the film is small (several micrometers to tens of micrometers).

Firstly, insert the cleaved optical fiber into ceramic ferrule. By simply immersing the ferrule tip into photoresist solution and then evaporate the solvent, a uniform layer of photoresist can be obtained. Since the diameter of the single mode fiber (125 μm) is much smaller than that of the ceramic ferrule (~3 mm), the curvature of the thin film on the fiber tip is sufficiently small. The thickness of the photoresist film can be controlled by adjusting the concentration of the photoresist solution.

The dip coating method can be further modified to improve the quality of the photoresist film. After the end-face of fiber ferrule is dip coated with photoresist solution, a glass slide coated with anti-adhesion layer made in polydimethylsiloxane (PDMS) is used to press the photoresist droplet, where a polymer spacer with specific thickness is employed to precisely control the thickness. Then the whole device is soft baked to remove the solvent, finally the photoresist coated fiber ferrule can be peeled off from the glass slide after cooling down to room temperature.

Compared with dip coating, spray coating is a more flexible and versatile method for photoresist deposition. An ultrasonic nozzle was utilized

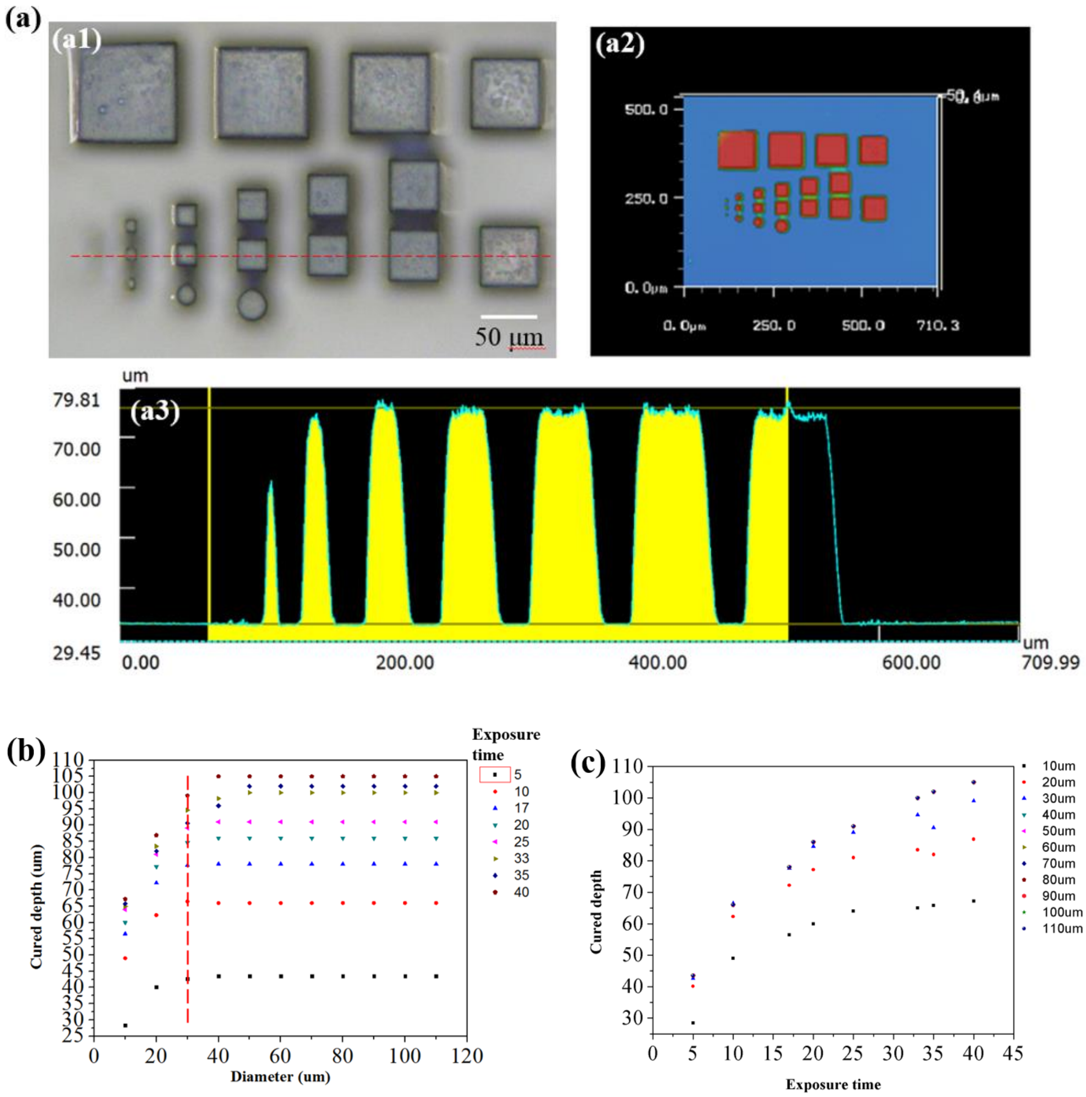

Figure 2.7 Optimization of the exposure conditions on planar substrates. (a) Optical image of the fabricated test pattern. Topography obtained by a confocal microscope is shown in (a2) and (a3) shows thee surface profile. (b) and (c) illustrate the relationship between cure depth and exposure doze. The size of the rectangular is also considered.

to integrate the spray coating process with the optical maskless exposure technology to establish an optical 3D μ-printing technology. The thickness of the single-layer photoresist film can be tailored by adjusting the pumping rate of the syringe pump and the scanning velocity as well as the gas pressure associated with ultrasonic nozzle and the distance between the nozzle and substrate. In order to evaporate the solution after spray coating, ceramic heaters and thermal-couple were embedded in the mount of optical fiber to form a miniature integrated digital microheater.

2.4.3.3 Dynamic optical exposure

The optical fiber is firstly moved to a position below the ultrasonic nozzle for spray coating of a thin layer of photoresist. Then the film is in situ soft-baked to remove solvent. The soft-bake time is optimized according to the concentration of photoresist solution and the film thickness. After soft bake, the sample is moved to the pre-aligned position for optical exposure, with the assistance of the digital camera-based machine vision metrology. Thereafter, the image data that sliced from the CAD model of the 3D microstructure by own-developed add-on software is used to generate optical patterns to irradiate the photoresist film on the optical fiber end-face. A typical exposure time is about 10 seconds under the power density of 35.86 mw/cm^2. After exposure, the sample is in situ post-baked by using the integrated digital micro-heater. The processes are automatically repeated for the fabrication of the next layer of 3D microstructure. Finally, the sample is developed by using suitable developer.

It's notable that the optimization of fabrication conditions is necessary before μ-printing on the end-face of optical fiber. A series of squares with different sizes are employed as test patterns. The fabrication is conducted on planar substrate for simplification, and an optical image of the fabricated micropads is shown in **Figure 2.7 (a)**. The exposure dose has been varied to investigate its influence on cure depth and the relationship is summarized in **Figure 2.7 (b)** and **(c)**. We not only test the exposure dose versus cure depth relationship, but also examine the influence of pattern size. The profile of the micropads marked by red line in **Figure 2.7 (a1)** is illustrated in **(a2)**. The exposure dose for these squares are the same, which should have resulted in similar cure depth. However, the height of micropads with smaller size breaks the uniformity. It's interesting to find out that for squares with side lengths larger than 30 μm, the exposure dose *vs*. cure depth curves are identical; while for patterns with smaller feature size, the cure depth under certain exposure dose tends to be reduced. We believe this phenomenon is due to the proximity effect, which also indicates that the ideal exposure dose for microstructures with distinguishing feature sizes need to be optimized individually.

The exposure dose *vs*. cure depth relationship can be used as a reference for μ-printing on the end-face of optical fiber. Further optimization based on fabrication results is required to produce microstructures identical to the design.

2.5 Summary

In summary, a DMD-based optical 3D μ-printing technology for the development of novel fiber-tip sensors is introduced in detail in this chapter. Firstly, conventional optical fiber-tip sensors based on FP cavities are reviewed. We illustrate and analyze the sensing mechanisms of these fiber-tip FPI sensors in detail, which lays the foundation of sensors to be presented in the following chapters. Then a variety of state of art micro/nano-fabrication techniques enabling the implementation of micro/nano-structures on the end-face of optical fiber for sensor development are introduced. Meanwhile, a number of sensing application based on these fiber-top microstructures are reviewed. In the following section, we introduce a DMD-based optical 3D μ-printing technology for fiber-top microstructures in the aspects of system components and general fabrication procedure, which starts with the 3D models design and data converting, then followed with the deposition of photoresist thin film onto the end-face of optical fiber, and finally a dynamic UV exposure process and development.

Chapter 3

Miniature Optical Fiber Displacement Sensors Based on Optically 3D μ-Printed Ferrule-Top Suspended Mirrors

3.1 Introduction

A Suspended mirror is a typical resonant component widely employed in optomechanics [165]. With one of the mirrors in the optical cavity suspended, optomechanical resonant interactions can be observed and investigated in the resonant cavity. The cavity has been called a “rubber cavity” [166] because the mechanical motion directly modulates the cavity length which will shift the resonant frequency. The first experimental implementation of suspended mirrors was a Fabry-Pérot (FP) cavity with moving mirrors for detection of gravitational waves through laser interferometry [167]. Later on, demonstrations of optical bistability [168], optical spring effect [169], and optical cooling [170] with suspended mirrors on the gram scale have also been made.

A suspended mirror not only works as a mechanical resonator but also intrinsically plays the role of an optical reflector. Besides investigations of optomechanical coupling in a cavity, a more straightforward application is to interrogate the displacement of the suspended mirror through monitoring the FP cavity. Olcum S et al. [171] demonstrated mass measurement of nanoparticles at the attogram scale using suspended nanochannel resonators. The system uses the resonant frequency of a microcantilever suspended in vacuum to detect the motion of the cantilever. The displacement of the suspended mirror is converted into electric signal acquired from the photodetector. High sensitivity can be achieved because the mechanical resonant frequency of the suspended microcantilever is highly sensitive to the change of mass. Moreover, such suspended mirror devices, especially for micromachined cantilevers, have been used for the detection of small forces [172, 173] and biochemical molecular molecules [174].

Although suspended mirror devices can achieve ultrahigh sensitivity, a major problem which prevents the wide usage of these sensors outside laboratories is the requirement for sophisticated readout apparatus that can precisely detect the suspended mirror's position. Optical readout methods have advantages of high accuracy and immunity to EMI over electronic ones, however, the alignment of the light beam with the suspended mirror is complicated and time consuming.

Since the end surface of optical fiber is an inherently light-coupled substrate, it's very attractive for the development of compact and highly integrated fiber-top suspended mirror devices which can be easily interrogated without the necessity of alignment procedure. If a suspended mirror is printed on the end surface of an optical fiber, light can be directly coupled into this FP cavity and the reflected signal can be easily collected for the interrogation of the suspended mirror through the same fiber. The deflection of the suspended mirror can be monitored to detect displacement induced by external force, which can be further employed as a miniature fiber-optic displacement sensor. Such displacement sensors can be further explored and employed for applications like atomic force microscope, biological and chemical sensors.

However, the small cross-section and large aspect-ratio of optical fibers make it difficult to be processed by using conventional micro/nano-fabrication platforms as described in Chapter 2. Iannuzzi's group has made significant contributions to the development of optical fiber sensors based on fiber-top cantilevers via carving a suspended beam from the cleaved edge of optical fiber by FIB [120]. Other techniques such as photolithography [26], nanoimprinting [27], interference lithography [28], electron-beam lithography [29] and two-photo polymerization [136] have also been proposed to overcome the challenges existing in fabricating micro/nano-structures on the end-face of optical fiber. However, these methods have some drawbacks such as time consuming, inconvenient fabrication process, and generally low throughput.

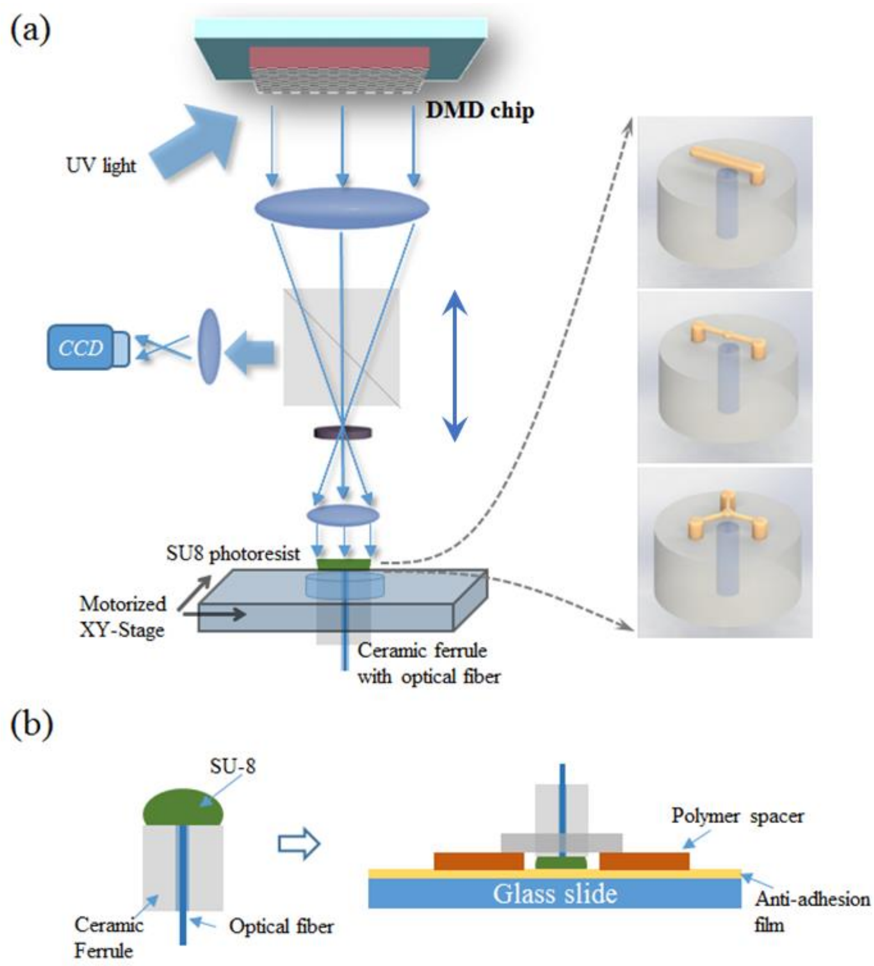

Figure 3.1 (a) Schematic diagram of the optical 3D μ-Printing technology. (b) The deposition of SU-8 photoresist thin film on the end-face of a ceramic ferrule of optical fiber.

In this chapter, a novel 3D optical microfabrication method is introduced to directly print SMDs on the end surface of an optical fiber ferrule. The ceramic ferrule is temporarily employed to increase the area of the substrate, thus reducing the degree of difficulty in deposition of photoresist and optical 3D μ-printing process. In the following two chapters, owing to the improvement of the microfabrication technology, the ferrule of optical fiber connector is removed, and the μ-printed structures are scaled down to the end-face of optical fiber. As shown in **Figure 3.1 (a)**, an optical 3D μ-printing platform is established by using a UV grade digital-mirror device (DMD) and a high-power UV source at wavelength of 365 nm [175, 176]. Three kinds of SMDs with different geometries are designed by using a commercial CAD software, as shown in the right side of **Figure 3.1 (a)**. These three types of SMDs differ not only in geometries, but also in mechanical resonance properties, which will be presented in next section. Then, an in-house developed add-on software is used to slice the 3D model into 200 layers to generate the image data. For this kind of gray scale pattern, the image data can be stored and presented in a bitmap format. With another in-house developed control software, the image data is loaded to the DMD chip frame-by-frame to dynamically generate the optical patterns. Since the switching speed of the DMD chip is very high (less than 1 ms), accurate control of the exposure dose can be achieved. After passing through projection optics, UV light patterns are projected upon the photoresist coated on the end surface of an optical fiber ferrule. Motorized XY-stage with high precision is employed to move the optical fiber to the position for UV exposure. Based on the monotonically additive light-penetration property in photoresist, i.e., the optical pattern used for the exposure of the top layer affects the other layers below to be fabricated in an additive manner [177], the predefined SMD with 3D features can be fabricated in a layer-by-layer exposure scheme.

3.2 Design and analysis of polymer suspended-mirror devices

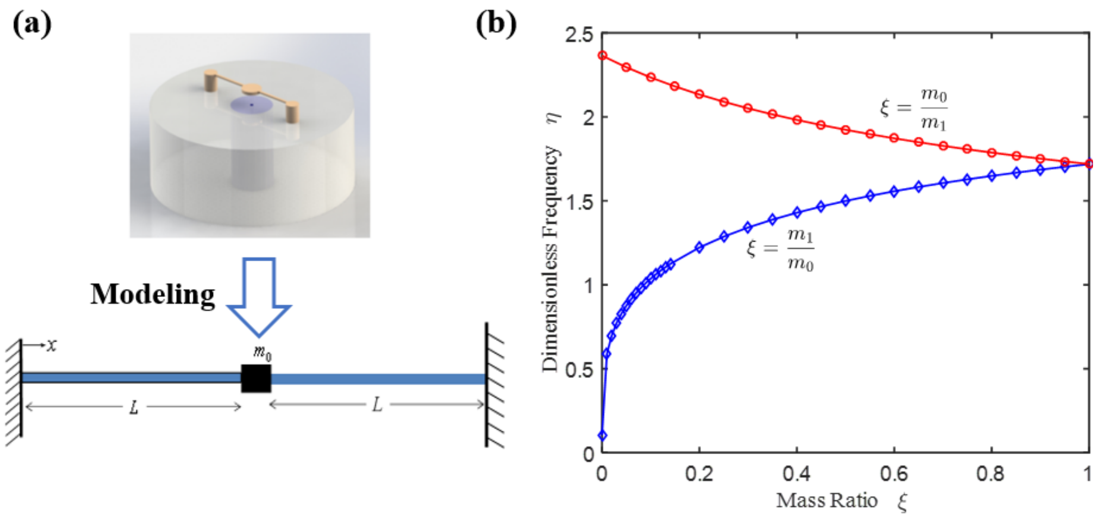

Figure 3.2 (a) Theoretical modelling of a suspended-mirror device. (b) Calculated dependence of dimensionless frequency on mass ratio.

3.2.1 Theoretical modeling of suspended-mirror devices

As shown in **Figure 3.2 (a)**, the two ends clamped suspended mirror is considered as a uniform cantilever beam with length L and a tip mass m_0 for simplification. The governing equation of the vibration of an Euler beam is given by [178]

$$EI\frac{\partial^4 w}{\partial x^4}+\rho\frac{\partial^2 w}{\partial t^2}=0, \tag{3.1}$$

where E, I and ρ are Young's modulus and the second moment of the crosssectional area and linear density, respectively, x is the coordinate measured from the clamped end and w is the deflection which is a function of x and time t.

The boundary conditions are

$$w(0,t)=0,\ w'(0,t)=0,\ w'(L,t)=0,\ EIw'''(L,t)=m_0\ddot{w}(L,t), \tag{3.2}$$

where $w' \equiv \partial w/\partial x,\ \dot{w} \equiv \partial w/\partial t.$

Solving Equation 3.2, the resonant frequency of the cantilever beam is

$$f=\frac{\omega}{2\pi}=\frac{\eta^2}{2\pi}\sqrt{\frac{EI}{\rho L^4}}, \tag{3.3}$$

where η is a coefficient related to the tip mass and is plotted in **Figure 3.2 (b)**.

3.2.1 Finite element analysis of suspended-mirror devices

Finite element method (FEM) has also been used to calculate the fundamental resonance frequency of the suspended mirrors. **Figure 3.3** shows the fundamental mode's shapes of three different types of suspended mirror devices and the values of fundamental frequency are marked in the figure, respectively. The results indicate that the eigenfrequency will decrease if we increase the weight of the suspended mirror. Meanwhile, the geometry of the suspended mirror has significant influence on its fundamental frequency. For instance, a cantilever-like suspended mirror with one end clamped has lower fundamental resonance frequency than that of a suspended mirror with both ends clamped when they have same beam length and thickness. The value of the resonance frequency matches the result obtained from Equation 3.3. The length, width and thickness of the suspended beams used for simulation is 430 μm, 30 μm and 10 μm, respectively. The diameter and thickness of the mass block is 60 μm and 40 μm, respectively. The Young's modulus and Poisson ratio of SU-8 used in simulation are 4.0 GPa and 0.22, respectively.

Figure 3.3 FEM simulation results for mechanical resonance of the suspended mirrors.

3.3 Fabrication of polymer suspended-mirror devices

SU-8 is a well-known epoxy-based negative photoresist which has been widely used in the fields of MEMS and bio-MEMS. SU-8 is often employed to fabricate polymer optical devices due to its favorable properties such as good mechanical strength, highly transparent in both visible and near infrared band range and chemical resistance.

EPON resin SU-8 from Momentive Ltd. was used in the fabrication of SMDs. The photoacid generator was octoxyphenylphenyliodonium hexafluoroantimonate (OPPI) (Hampford Research Inc.), and tributylamine

(Meryer Chemical Technology Co., Ltd.) was used as the inhibitor to improve lateral resolution. A UV-absorbing agent, 2-(2H-Benzotriazol-2-yl)-4,6-bis(1-methyl-1-phenylethyl)phenol (also known as Tinuvin 234) (Sigma-Aldrich Inc.), was used to suppress light penetration depth and enhance the vertical resolution in the UV exposure process. Cyclopentanone (Sigma-Aldrich Inc.) was utilized to dissolve these compositions in a weight ratio of OPPI/tributylamine/Tinuvin 234/SU-8 = 2:0.014:0.2:100. The concentration of inhibitor and UV dye can be tuned to optimize the fabricated results but there is always a tradeoff between resolution and fabrication speed. Higher concentration of UV dye and inhibitor tends to yield subtle 3D features at the cost of longer fabrication time. The developer used in the experiments was propyleneglycol monomethylether acetate (PGMEA) (Sigma-Aldrich Inc.).

As discussed in Section 2.4.3, a challenge in micro/nano-fabrication on the end-face of optical fiber is to deposit this unconventional substrate with a uniform layer of photoresist. Similarly, coating the end-face of ceramic ferrules with a flat layer of SU-8 photoresist with accurate thickness is vitally important for critical dimension control of SMDs. For wafer scale substrates, spinning coating is commonly used for the deposition of photoresist, however, due to the limited area and large aspect ratio of ferrule end-face, it’s not suitable to directly employ spinning coating on ferrule end-face.

Instead of spinning coating, a simple method is used to coat a uniform layer of SU-8 on the ferrule end-face. As shown in **Figure 3.1 (b)**, firstly, a small amount of SU-8 solution with given volume is dropped upon the end-face of the fiber ferrule by using a pipettor. Then, the SU-8 droplet is pressed by a glass slide which is coated with a thin layer of polydimethylsiloxane (PDMS) for anti-adhesion. The thickness of the SU-8 film can be precisely controlled with the assistance of a polymer spacer with specific thickness.

Thereafter, a digital hotplate is employed for the so-called soft bake process to remove the extra solvent. Both the concentration of SU-8 solution and the target thickness of SU-8 film depend the optimal soft bake time. For example, the sample is soft baked at 65 °C for 5 minutes, and then gradually increase the temperature to 95 °C and hold on for 20 minutes when the concentration of SU-8 solution is 70% (in weight ratio) and the designed film thickness is 70 μm. After cooling down to room temperature, the fiber ferrule can be easily peeled off from the glass slide with a uniform SU-8 film coated on its end-face. This simple but effective method is particularly suitable for the preparation of relatively thick film (from ~10 μm to ~500 μm) when compared with other methods such as spinning coating, spray coating and thermal evaporation. Spacers with customized thicknesses are needed if the heights of the SMDs to be fabricated are various. A more convenient and universal method is to mount the glass slide with anti-adhesion layer on a high-precision motorized vertical stage to press the SU-8 droplet and thereby precisely define the thickness of the SU-8 film.

After soft bake process, the sample is precisely aligned to the target location for optical exposure with the digital camera-based machine vision metrology. A red laser light is launched into the optical fiber for illumination and the light spot above the fiber core is captured by the digital camera for alignment. The projection optics is then moved to a specific vertical position by using a motorized Z stage for UV exposure so that a clear pattern is projected upon the SU-8 thin film. With the sliced image data of the SMD models, a dynamic optical exposure process is then applied to the SU-8 photoresist on the ferrule top, which typically takes about 15~20 seconds under the power density of 35.86 mW/cm^2. The vertical position of the projection optics is a critical parameter which needs to be optimized before optical exposure. A calibration pattern is usually employed to illuminate the substrate and the image is captured by the CCD camera. A rough tuning can be performed by scanning the vertical position of the projection optics until a clear image of the predefined pattern is obtained. The vertical position acquired from rough tuning is then used as a baseline, and a finer tuning is accomplished by μ-printing target microstructures with a series of vertical positions around the baseline. The optimized vertical position for the projection optics is then determined by evaluating the fabrication results.

After dynamic UV exposure, a post bake process where the sample is baked at 65 °C for 5 minutes and 95 °C for 15 minutes is conducted to

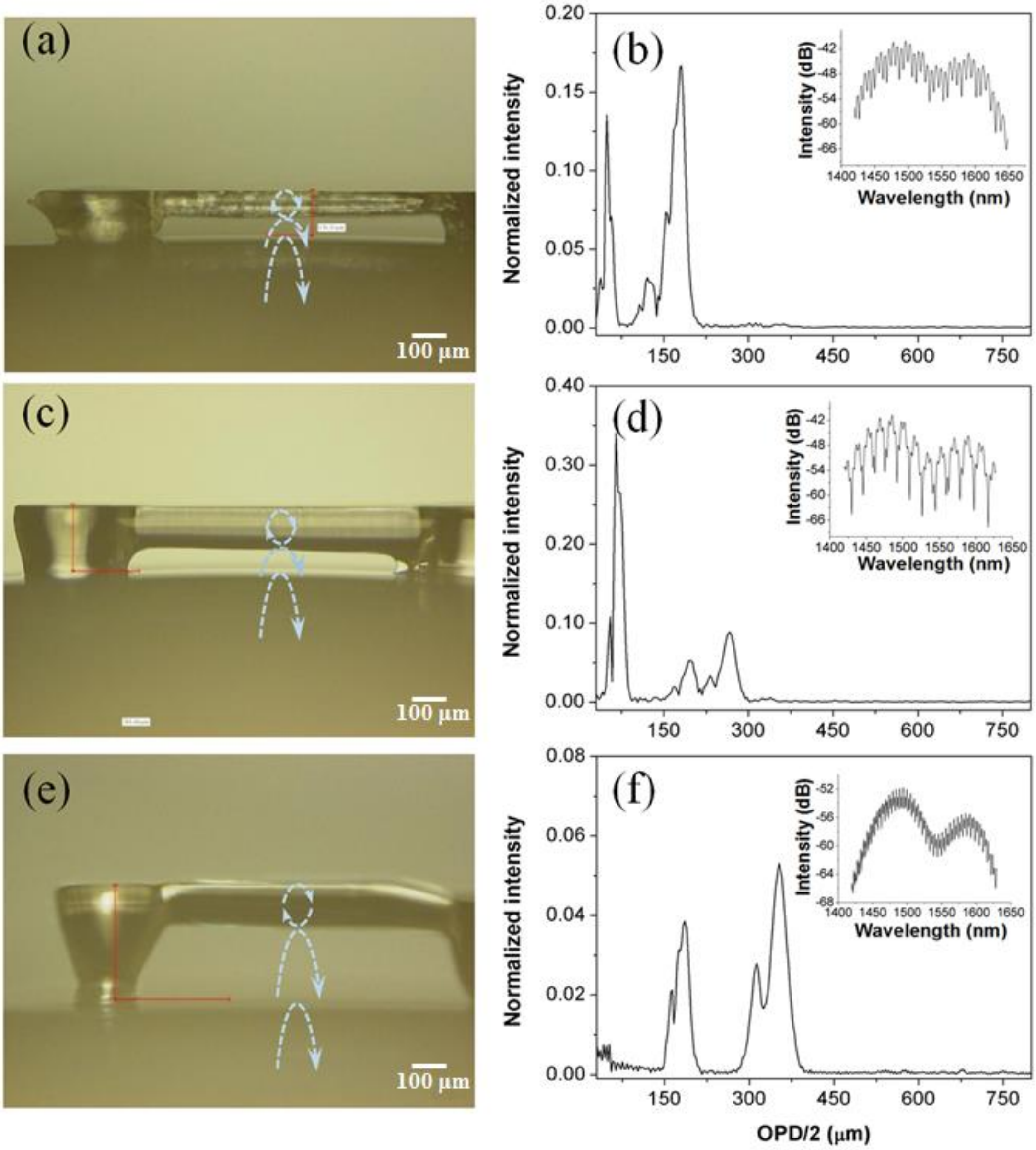

Figure 3.4 (a), (c) and (e) Optical images of three ferrule-top SMDs with different cavity lengths. (b), (d) and (f) FFT results of the reflection spectra of the corresponding SMDs shown in (a), (c) and (e), respectively. The insets are their measured reflection spectra.

provide energy for the cross-link reaction. Both the increasing and decreasing of baking temperature are slow and gradual to avoid crack. Finally, the sample is immersed in PGMEA and the developing time is about

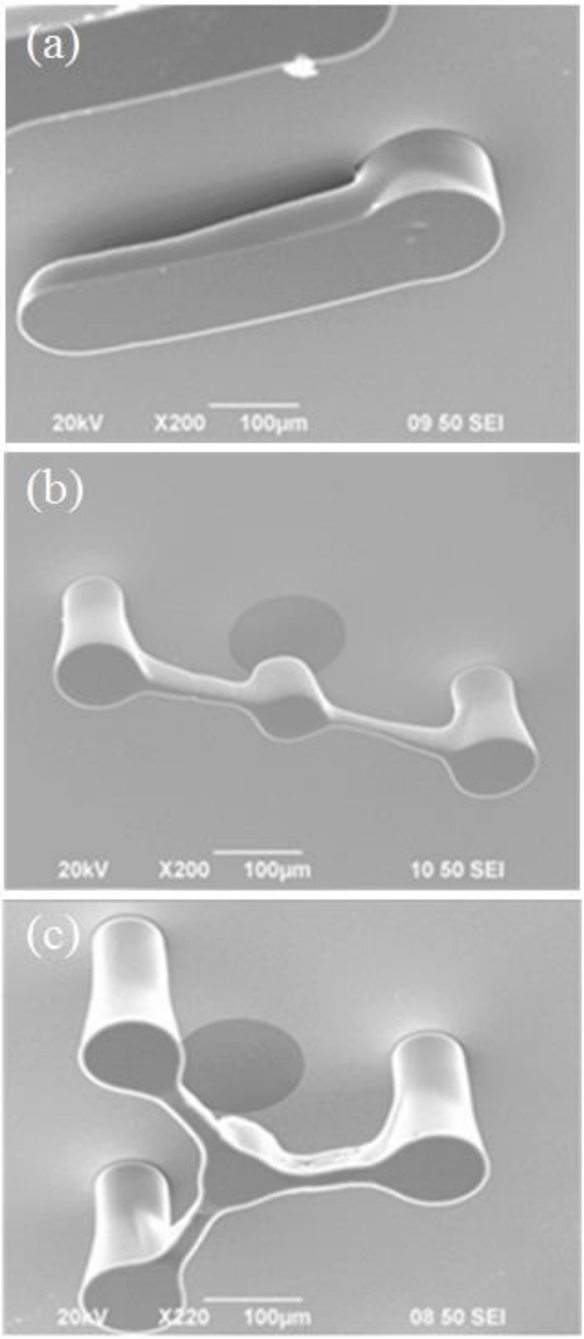

Figure 3.5 Scanning electron microscope images of the suspended mirrors on the end surface of ferrule of optical fiber connector.

15 minutes, followed by a rinse process by using isopropanol to minimize the risk of collapse of the 3D microstructures induced by stiction issue.

Another key parameter for the fabrication of SMDs is the optical exposure dose. The fabrication conditions for the supporting pillar and the suspended parts of the designed SMD need to be optimized, respectively. Sufficient exposure dose is preferred for the supporting pillars to guarantee good adhesion with the substrate while the exposure dose for the suspended beams need to be precisely controlled. As introduced in Section 2.4.3, test patterns are firstly fabricated on planar substrates such as silica wafer to figure out the relationship between cure depth and UV exposure dose for the specific photoresist, which provides guidance for the exposure dose of the SMDs to be printed. Further optimization based on the fabrication results if needed for SMDs with different thicknesses of mirrors. By changing the thicknesses of polymer spacers, the total height of the device can be tailored.

Optical images of three fabricated ferrule-top SMDs with different thicknesses are shown in **Figure 3.4 (a)**, **(c)** and **(e)**. A broadband light source, a circulator and an optical spectrum analyzer (OSA) are used to measure their reflection spectra for the characterization of the optical properties of the devices. Fast Fourier transform (FFT) is widely used to analyze the reflection spectra of FPIs. From Equation 2.12, we can see that the period/frequency of the cosine function, which can be determined by the location of peaks in the frequency domain spectra, is related to the cavity length. In our experiments, we adopted FFT to retrieve the cavity information, *i.e.* cavity length, from the measured optical reflection spectra. The FFT's results of the reflection spectra of the SMDs with different cavity lengths are depicted in **Figure 3.4 (b)**, **(d)** and **(f)**, respectively. Inset figures show the corresponding reflection spectra. Since the refractive indices of glass and SU-8 at the wavelength around 1550 nm are 1.46 and 1.57, respectively, the reflectivities of light at the fiber end-face/air and air/suspended-mirror interfaces calculated by Fresnel's equation are 3.5 % and 4.9 %, respectively. It's notable that there are three major peaks in each FFT spectrum, which indicates the interferences occur between the light waves reflected from three interfaces, *i.e.* the interface between fiber end surface and air, the interface between air and bottom face of the suspended mirror, and the interface between air and top face of the suspended mirror. The reflection at each interface is marked by arrow in **Figure 3.4 (a)**, **(c)** and **(e)**. The locations of the peaks are in accordance with the cavity lengths of the SMDs measured by using optical microscope. It's noteworthy that in real application, the resolution of FFT is limited by the spectra width of the light source, the detectable spectra range of the optical spectra analyzer and its resolution. The resolution of cavity length acquired from FFT's result can be estimated by

$$\delta L_c \propto 1/(\lambda_1 - \lambda_0), \tag{3.4}$$

where λ_0 and λ_1 are the start and stop wavelength of the measured reflection spectrum.

Three kinds of SMDs with different geometries as shown in **Figure 3.1 (a)** are fabricated based on the optimized fabrication conditions. **Figure 3.5** illustrate the scanning electron microscope (SEM) images of the fabricated SMDs on the end surfaces of optical fiber ferrules. One can see that the geometries of these fabricated SMDs agree well with the pre-designed 3D

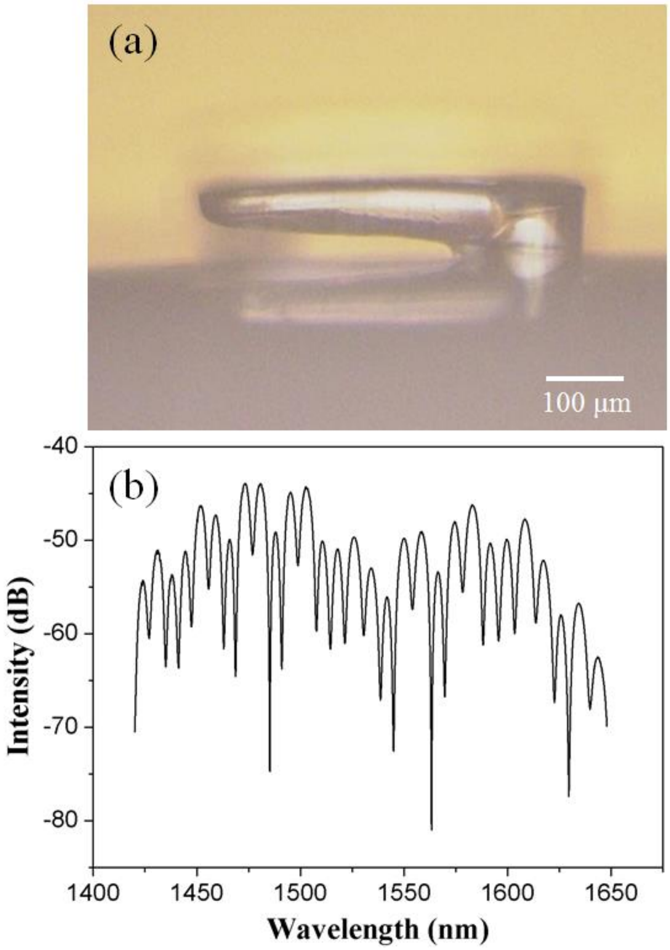

Figure 3.6 (a) Optical microscope image of the cantilever-beam SMDs for displacement sensing. (b) The measured reflection spectra of the SMD.

models, and the alignment between the suspended mirror and the fiber core is good. Moreover, the surfaces of these suspended mirrors are very smooth judging by the SEM images, which is significant for enhancing the reflectivity of the suspended mirror. The root-mean-square surface roughness is measured to be about 5.11 nm by using an atomic force microscope (MultiMode 8, Bruker, Germany).

3.4 Testing of the polymer suspended-mirror devices

3.4.1 Measured reflection spectra

The optical microscope image and the reflection spectrum of the cantilever-beam like SMD as shown in **Figure 3.5 (a)** are depicted in **Figure 3.6**. The cantilever beam's length, width, and thickness are measured to be about 430, 84, and 62 μm, respectively. The fundamental resonant frequency of the cantilever-beam device is estimated as 98.9 kHz by using the finite-element analysis with the measured geometric parameters. By tailoring the geometric parameters such as beam length, width and thickness, the resonant frequency can be tuned flexibly. Since the Young's modulus of SU-8 is relatively low when compared with inorganic materials commonly used for MEMS such as silicon (around 20% of that of silicon), SMDs fabricated by our optical 3D μ-printing technology have generally lower resonant frequencies when compared to devices made from inorganic materials with same geometric parameters.

3.4.2 Displacement sensing

We have experimentally demonstrated that the cantilever-beam SMD can be employed as a displacement sensor. As discussed in Section 2.2.1, the wavelength of a resonance dip in the reflection spectrum of two-beam interference can be expressed as

$$\lambda_m = 2n_r L_c / m \tag{3.5}$$

where n_r is the refractive index of the medium filled in the FP cavity, L_c is

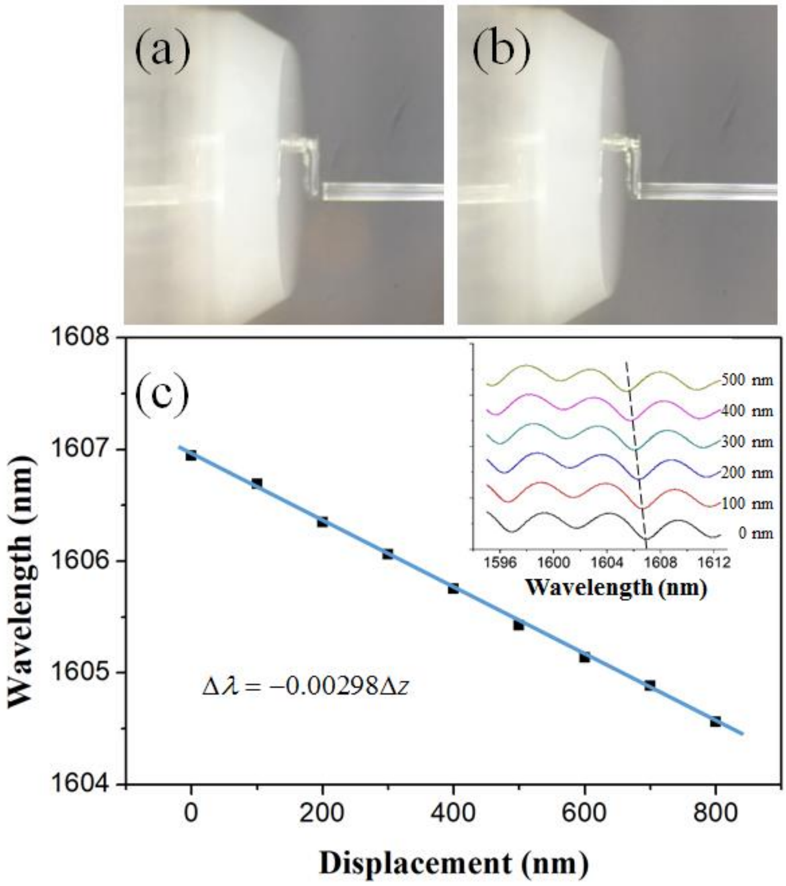

Figure 3.7 (a, b) Microscopic images of a ferrule-top SMD under test. (c) Spectral response of the ferrule-top SMD under pressing. Inset shows the measured reflection spectra under different displacements.

the cavity length and m is the order of the resonant dip. When the free-standing end of the SMD experiences a small displacement dz induced by external force, the spectral shift a resonant dip/peak can be estimated by

$$\Delta\lambda \cong (\lambda_m / L_c) K(x) \Delta z , \qquad (3.6)$$

where $K(x)$ is a coefficient describing the ratio of the cavity length change ΔL to the displacement Δz, which is closely related to the relative position of the SMD over the optical fiber core. By using the profile of cantilever-beam under deflection, $K(x)$ can be numerically calculated.

Optical images of SMD displacement sensor under testing are illustrated in **Figure 3.7 (a)** and **(b)**. The free-standing end of the SMD was pressed by the cleaved tip of a section of optical fiber which was mounted on a PZT nanopositioner. The displacement could be precisely controlled by the nanopositioner while the reflection spectra of the sensor under a series of displacements were recorded, which are shown in the inset of **Figure 3.7 (c)**. We observed a blue shift of the spectra when the displacement increased. A linear relationship between the wavelength of a tracked resonant dip and displacement is depicted in **Figure 3.7 (c)**, which yields a measured spectral sensitivity of 2.98 nm/μm over a small displacement. The theoretically predicted sensitivity is 2.61 nm/μm by using Equation 3.6, which is similar with the experimental result. **Table. 1** summarize several optical fiber displacement/indentation sensors based on different mechanisms including interferometers [179-181], intensity-modulated sensors [182], fiber Bragg gratings [183], and ferrule/fiber-top microcantilevers [119, 184].

Table. 1 Performance summary of different types of optical fiber displacement sensors.

Ref. No.	Types	Operation mode	Sensitivity	Resolution	Dynamic range
179	Michelson and FP interferometer	movable reflector, non-contact	-	2 ~ 45 nm	140 μm
180	fiber-optic FP interferometer	movable reflector, non-contact	-	0.005 nm	0.005 ~ 3200 nm
181	in-line Mach-Zehnder interferometer	movable optical fiber, contact	-0.669 dB/μm	-	0 ~ 30 μm
182	intensity modulated sensor	movable reflector, non-contact	77 μV/nm	1 nm/Hz$^{1/2}$	140 ~ 220 μm
183	fiber Bragg grating	embedded FBG, physical contact	0.6234 nm/mm	-	0 ~ 7 mm
184	ferrule-top indenter	ferrule-top cantilever, contact	300 nm/V	0.6 nm	5 μm
119	fiber-top cantilever	physical contact	-148 nm/V	-	-
our work	ferrule-top suspended mirror	ferrule-top cantilever, contact	2.98 nm/μm	0.3 nm	20 μm

The fabricated SMD shows both good adhesion with the end-face of fiber ferrule and mechanical strength in the experiments. No detachment nor collapse have been observed during the test in which the suspended mirror was pressed forward and back repeatedly. It's confirmed by thermal testing experiments that the device can stand high temperature up to 170 °C, which is actually the hard bake temperature. Moreover, although the reflection spectrum shifts during the heating or cooling process, it can finally recover back to the original state after thermal cycling tests. Since temperature also has influence on the spectra shift of the SMD, which has shown a temperature sensitivity of 0.135 nm/°C in the test of thermal response, the device is kept in room temperature during the displacement test. The long-term stability of the sensor is yet to be investigated, which is crucial for practical use. It's notable that such displacement sensors can be further employed for applications like atomic force microscope and miniature force sensors.

3.5 Summary

The optical 3D μ-printing technology described in Section 2.4.2 has been employed to directly print different kinds of SMDs on the end-faces of optical fiber ferrules for displacement sensing. The reflection spectra of the ferrule-top SMDs have been measured to characterize the SMDs and fast Fourier transform has been adopted to numerically analyze the cavity information of the FPI. Moreover, we have experimentally demonstrated the application of the fabricated ferrule-top SMD as a displacement microsensor and a sensitivity of 2.98 nm/μm has been achieved. Such displacement sensors pave way for the development of miniature fiber-top atomic force microscope, micro force sensor, and biological and chemical sensors. Last but not least, the optical microfabrication technology has capability of rapid printing complex 3D SMDs on the end-faces of optical fiber ferrules, which provides an attractive platform for the development of miniature optical fiber-tip sensors.

Chapter 4

Ultrasmall Optical Fiber Refractive-Index Sensors based on In-Situ μ-Printed Fiber-Top Suspended Microbeams

4.1 Introduction

As discussed in Chapter 2, due to their favorable characteristics of small size, electromagnetic interference immunity, high sensitivity, remote sensing and multiplexing capabilities, optical fiber sensors have been widely employed in a variety of applications including inertial navigational systems, environmental and structural monitoring, biochemical sensing, healthcare, food industry and homeland security [185-187]. With the development of micro/nano-fabrication technology, microscale components and functional materials have been recently integrated on the end surface of optical fiber to develop miniature optical fiber-tip sensors with remarkable performance for various sensing applications [18, 47, 188]. As an inherently light-coupled substrate [18], the flat end surface of optical fiber provides an ideal platform for development of compact photonic devices and sensors with high degree of integration, thus paving the way for a new horizon of "lab-on-fiber".

A great many of optical fiber-tip sensors based on various working principles and distinguishing structures have been proposed. As discussed in Chapter 2, optical fiber-tip sensors based on Fabry-Pérot (FP) interferometers is one of the commonly used structures, which typically consist of a thin diaphragm suspended over the end surface of optical fiber to form an open air cavity. Optical Fiber-tip sensors based on FP cavity have become a research hotspot for the detection of various physical and biological measurands including pressure [65, 102, 123], temperature [103], acoustic wave [48] and refractive index (RI) [121] because of their simple structure and high sensitivity. Optical microresonators with high quality factor have been implemented on the end-face of optical fiber for ultrasensitive ultrasound sensing via increasing the reflectivity of the mirrors of such FP cavities [85]. Moreover, miniature localized surface plasmon resonance (LSPR) biochemical probes have been realized by patterning periodic gold nanodot arrays [34], and high-performance surface-enhanced Raman scattering (SERS) sensors have been demonstrated by fabricating multilayer silver nanoparticles on the end-face of optical fiber [189]. Among all these sensing applications, the accurate measurement of refractive-index of liquid or gas is of high importance and in demand from a variety of fields such as homeland security, food safety, industry and medicine. Several schemes including optical fiber gratings [190-192], interferometers [193, 194], evanescent field [195], surface plasmon resonance [196, 197] have been proposed for refractive-index sensing. Here, fiber-top FP micro-interferometers are employed to detect refractive-index change.

A challenge existing in the fabrication of optical fiber-tip sensors by utilization of conventional microfabrication technologies is that the small size and large aspect-ratio of optical fiber tip is incompatible with commercially available fabrication platforms originally designed for planar substrates. In Section 2.3.1, we have introduced a diversity of fabrication techniques including photolithography [26], nanoimprinting [27], interference lithography [28], electron-beam lithography [29], focused ion-beam milling [30], multiphoton polymerization [31, 136, 141-143], which have been reported to solve the fabrication issue, however, there are some common drawbacks such as time consuming and low throughput, insufficient of flexibility and limited choices of processable materials.

In Chapter 3, we introduce that suspended-mirror devices (SMDs) can be in situ fabricated on the end-face of optical fiber ferrules by using an optical 3D μ-printing technology, and the application of the SMDs as miniature optical fiber displacement sensor has been experimentally demonstrated. However, such ferrule-top SMD sensors which have outer diameter of about 3 mm are still too large for scenarios where the miniaturization of the probe is crucial. For instance, in applications such as endoscopy and microfluidic chip, the sensors need to be small enough to be inserted into blood vessels and microfluidic channels where the space is highly limited. In this chapter, an improved optical μ-printing technology is presented to directly fabricate suspended-microbeams on the end-face of a standard single-mode optical fiber instead of the end-face of optical fiber ferrule. Real fiber-top devices rather than ferrule-top ones have been realized for the implementation of ultrasmall optical fiber-tip sensors.

4.2 Design and analysis of fiber-top suspended-microbeams

The structural design and working mechanism of the optical fiber refractive-index sensor based on fiber-top suspended-microbeams are depicted in **Figure 4.1**. Similar to the suspended-mirror devices introduced in Chapter 3, a hanging microbeam suspended over the end-face of optical fiber is clamped by supporting pillars. The cleaved end-face of standard single-mode fiber together with the suspended microbeam form an open air cavity. As a consequence, reflections occur at the interface between fiber end-face and air, and the two interfaces between air and the bottom/top surfaces of the microbeam. Optical interference happens among these reflected light beams, thus inducing an interference fringe in the reflection spectrum, as shown in **Figure 4.1 (a)**. It's known that the refractive-index of the medium filled in a FP cavity has influence on the optical path difference of two-beam

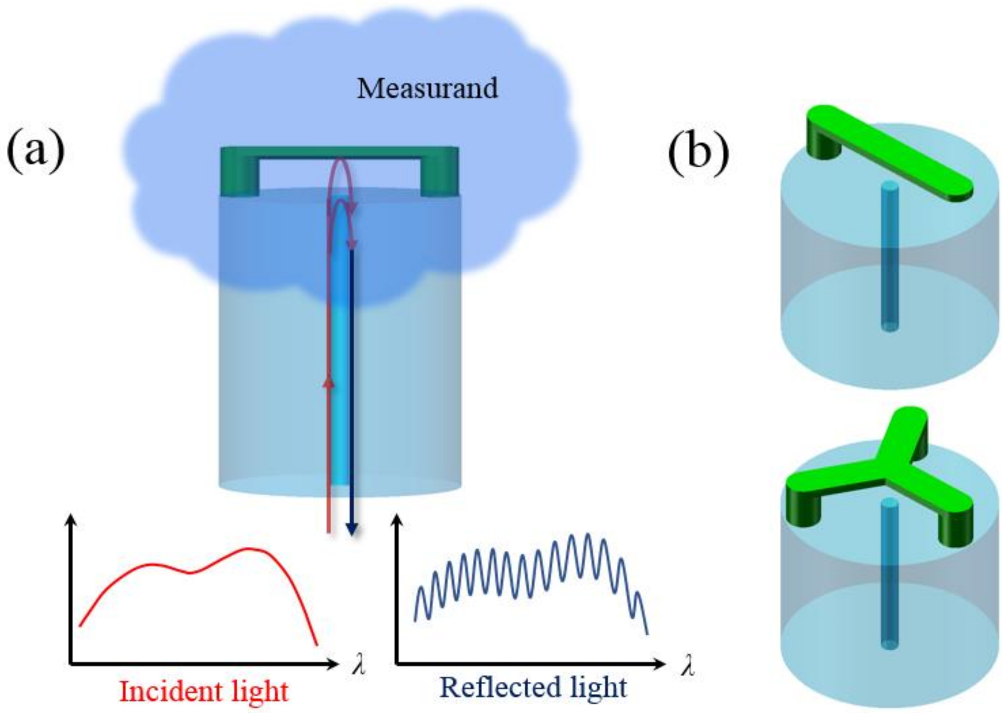

Figure 4.1. (a) Schematic of an optical fiber-tip sensor and its working principle. (b) Schematics of the other two optical fiber-tip sensors with different structures of suspended microbeams.

interference, thus variations in the medium's refractive-index will induce shift of the interference fringe. Based on this principle, when the fiber-top microbeam is immersed into a liquid or gas whose refractive index is different from the indices of optical fiber core and the polymer used to print the microbeam, the change of the refractive index of the liquid or gas can be detected through monitoring the shift of the interference fringe in the reflection spectrum. As shown in **Figure 4.1 (b)**, different kinds of suspended microbeams with distinguishing geometries have been designed to suit diverse sensing applications.

4.3 Fabrication of fiber-top suspended-microbeams

The material used to fabricate the suspended-microbeams was EPON resin SU-8 (Momentive Ltd.) due to its favorable properties such as highly transparent in both visible and near infrared band range, good mechanical strength, capability of serving as permanent components, biocompatibility, and chemical resistance. The refractive index of SU-8 after photopolymerization is around 1.57 at the wavelength of 1550 nm [198].

Octoxyphenylphenyliodoniumhexafluoroantimonate (OPPI) (Hampford Research Inc.) was used as photoacid generator and tributylamine (Meryer Chemical Technology Co., Ltd.) was employed as inhibitor which could improve the lateral resolution of the optical exposure. 2-(2H-Benzotriazol-2-yl)-4,6-bis (1-methyl-1-phenylethyl)phenol (also known as Tinuvin 234) (Sigma-Aldrich Inc.), which can absorb and block the UV light, was adopted to enhance the vertical resolution of the optical 3D μ-printing through controlling the penetration depth of UV light. It's notable that the UV absorption agent is used to roughly tune the property of the photosensitive material so as to enhance the vertical distinguishability, while a refined control of the vertical features of the microstructures depends on the UV exposure dose distribution defined by the dynamic exposure process. Cyclopentanone (Sigma-Aldrich Inc.) was employed as the solvent to dissolve these compositions. A typical weight ratio is

OPPI/tributylamine/Tinuvin 234/SU-8 = 2:0.014:0.2:100, and the concentration of each component can be adjusted according to the demands. For example, a lower weight ratio of Tinuvin 234 will lead to shorter exposure time at the cost of degraded vertical resolution. The developer used in the experiment was propyleneglycol monomethylether acetate (PGMEA) (Sigma-Aldrich Inc.).

An improved optical exposure setup, as shown in **Figure 4.2 (a)**, was utilized to fabricate the optical fiber-tip sensors based on suspended microbeams. The setup is similar to the one introduced in Chapter 3, while several modifications and upgrades have been made to enhance its performance and fabrication capability. A high-power UV LED (365 nm) instead of UV lamp is employed as the light source, and a UV-grade digital

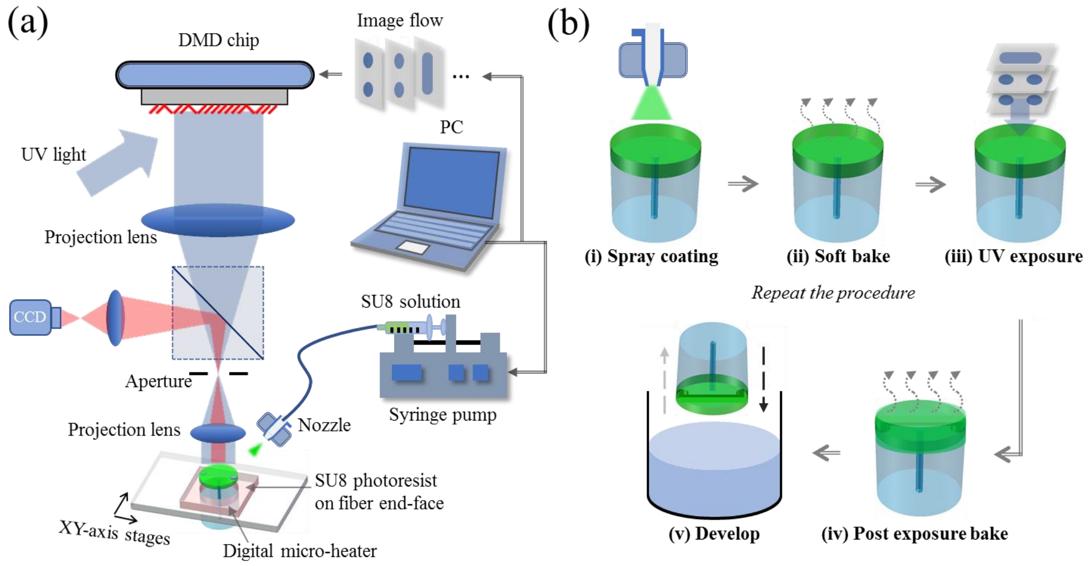

Figure 4.2. (a) Schematic diagram of the optical 3D μ-Printing technology. (b) Flow chart for printing the optical fiber-tip sensors.

mirror device (DMD), which has a reflectivity higher than 90% at the wavelength of 365 nm, is used to generate target optical patterns. Projection optics with larger magnification factor are utilized to scale down, yielding a 193 nm feature size corresponding to one pixel on the DMD chip. Machine vision metrology with richer features such as mark recognition has been developed based on a digital camera [199-201]. Compared with the deposition method presented in Chapter 3, an improved spray coating technique based on ultrasonic nozzle has been adopted to deposit uniform thin layers of SU-8 on the end-face of a standard single-mode fiber. The spray coating process was integrated with the dynamic optical maskless exposure technology for the establishment of an improved optical 3D μ-printing technology. The optical fiber tip was mounted on a XY-axis motorized stage with the assistance of a ceramic ferrule and customized adapter, while the alignment of the optical fiber to the positions for UV exposure and SU-8 film deposition was accomplished by the high precision stage. SU-8 solution was injected into the ultrasonic nozzle by a programmable syringe pump and compressed nitrogen was employed as the driving force for spray coating. Factors that determine the thickness of SU-8 film obtained by one time spray coating process include the pumping rate of the syringe pump, the pressure of nitrogen associated with the ultrasonic nozzle, the distance between the nozzle and the end-face of optical fiber, and the scanning velocity of the stage during spray coating. A scanning manner was adopted to further improve the quality of the film, where the nozzle was fixed while the substrate was moved through the spray region at a constant speed. Experimental results confirmed that the quality of the SU-8 film prepared by our spray coating method was as good as that obtained by spinning coating process, meanwhile the thickness of the SU-8 film on the end-face of optical fiber could be as thin as hundreds of nanometers. Since multiple parameters have influences on the thickness of the film, the thickness of the single-layer SU-8 film can be flexibly tailored by this versatile spray coating technique. Customized ceramic heaters with feed-back loop provide by thermal couple were integrated with the mount of optical fiber to establish a miniature digital microheater which could in situ evaporate extra solvent after spray coating.

The flow chart for the optical 3D μ-printing of fiber-top suspended beams is depicted in **Figure 4.2 (b)**. Firstly, the motorized stage moved the optical fiber to a position below the ultrasonic nozzle waiting for spray coating. The nozzle started to spray atomized SU-8 solution, after the spray flow became steady, the optical fiber passed through the spray area for the coating of one layer of SU-8 film. Then a in situ soft-bake process was accomplished by the embedded digital microheater to remove extra solvent. The optimized soft-bake time was determined by the concentration of SU-8 solution and the thickness of the film, and the temperature for soft-bake was 95 °C. After soft-bake procedure, the optical fiber was moved to a pre-aligned position below the objective lens for the UV exposure. The alignment was completed by launching a red laser into the optical fiber from the other end and capturing the light spot on the end-face coated with SU-8 through the digital camera-based machine vision metrology. Thereafter, the 3D model of the fiber-top suspended microbeam to be printed was converted to image flow by slicing the CAD model via own-developed add-on software. The image was loaded into the DMD chip for the generation optical patterns which would be projected onto the SU-8 photoresist on the end-face of optical fiber. A typical exposure dose was about 10 seconds under the power density of 35.86 mw/cm^2. The post exposure bake process, which would provide energy for the crosslink reaction, was in situ conducted under the temperature of 95°C after UV exposure by the utilization of the customized digital microheater. Then the procedures described above, *i.e.*, spray coating, soft bake, UV exposure, post exposure bake, were automatically repeated with the assistance of control software to fabricate the next layer of the target 3D microstructures. After all layers of the suspended microbeam were irradiated and baked, a final develop procedure was accomplished by immersing the sample into PGMEA for about 15 minutes, followed by a rinse process using IPA to avoid stiction issue. A hard-bake process could be

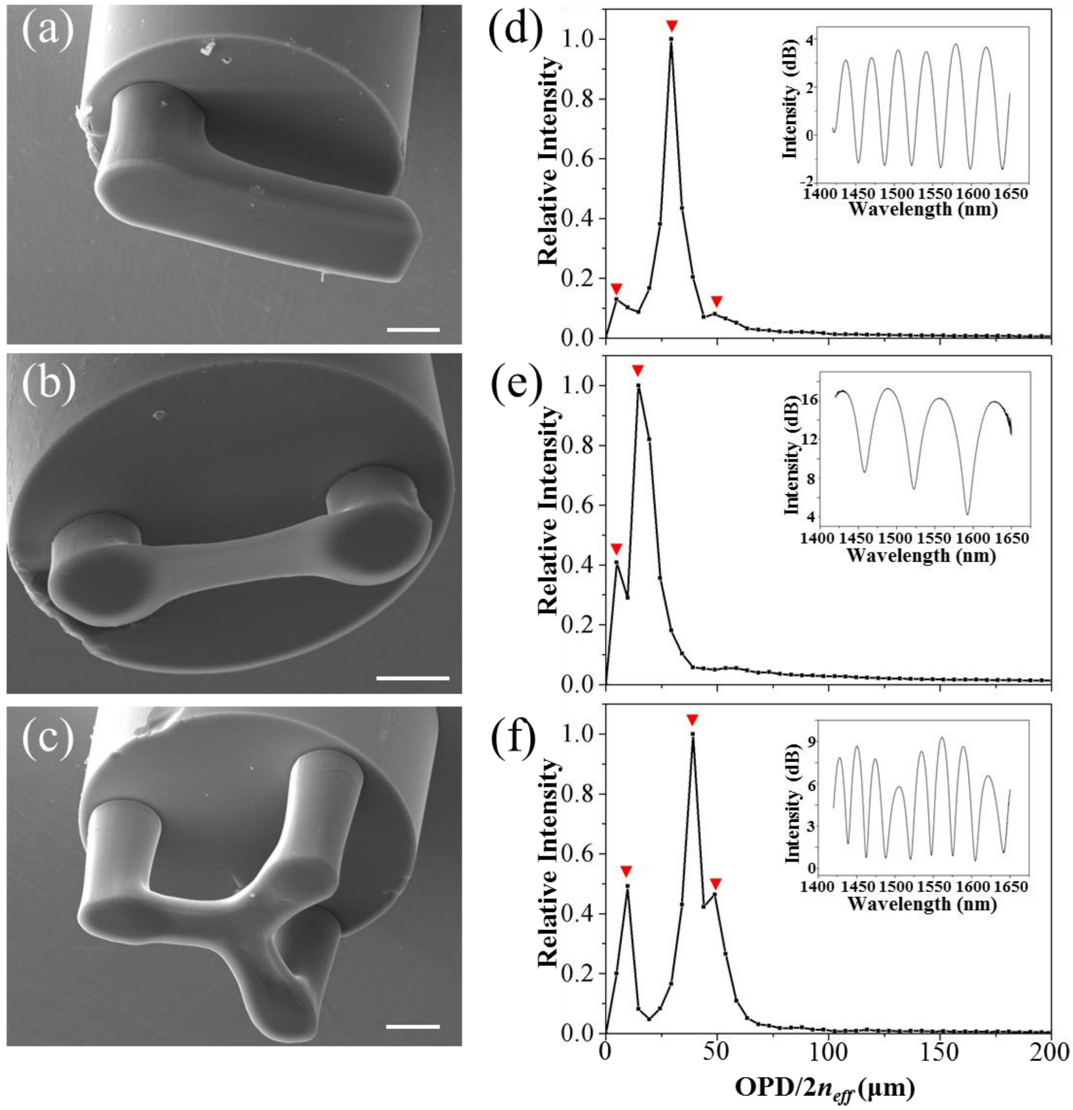

Figure 4.3. (a), (b) and (c) Scanning electron microscope (SEM) image of SU-8 suspended-microbeams printed on the end-face of optical fibers. All scale bars are 20 μm. (d), (e) and (f) FFT's results of the corresponding reflection spectra of optical fiber-tip sensors shown in (a), (b) and (c). Insets are the reflection spectra measured in air.

adopted for permanent devices. A temperature exceeded the highest temperature during the usage was recommended. In our experiment, the device was baked for 1 hour under 170°C to further improve its mechanical strength and chemical stability.

The scanning electron microscope (SEM) images of three types of fiber-top suspended-microbeams as designed in **Figure 4.1** are shown in **Figure 4.3 (a)**, **(b)** and **(c)**, respectively. From the SEM images one can see that the geometries of the fabricated suspended microbeams are in accordance with the original design, and the microstructures are well aligned with the optical fiber. The thicknesses of the three types of suspended microbeams are measured to be 2.2, 1.0 and 6.9 μm, respectively. Cavities lengths of these FP cavities formed by the suspended-microbeams and the end-face of optical fiber are measured to be 30.9, 15.6, and 40.4 μm according to the SEM images.

4.4 Testing of the optical fiber-top refractive-index sesnors

4.4.1 Measured reflection spectrum

The reflection spectra of the fabricated fiber-top suspended microbeams were measured firstly for the characterization of the optical fiber-tip FP micro-interferometers by using a broadband light source, a circulator and an optical spectrum analyzer (OSA), as shown in **Figure 4.4**. Fast Fourier transform (FFT) was applied to acquire the cavity information such as cavity length of the fiber-top micro-interferometers from their reflection spectra. **Figure 4.3 (d)**, **(e)** and **(f)** depict the FFT's results of the optical fiber-top FP micro-interferometers and inset figures show the corresponding reflection

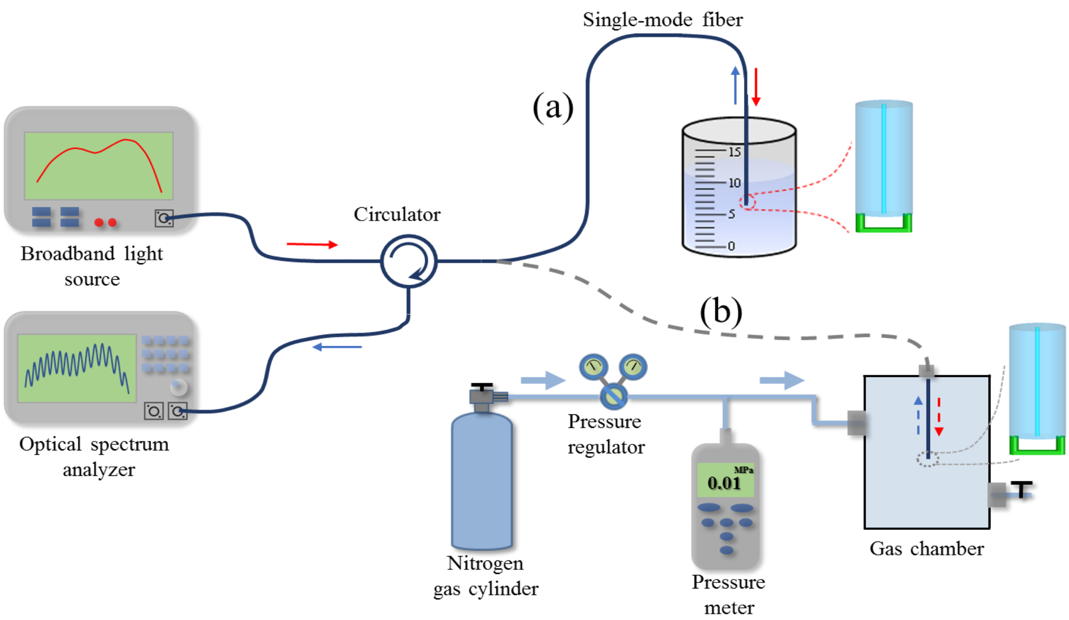

Figure 4.4. Schematic of the experimental setup for testing the optical fiber-tip sensors. (a) refractive index sensing; (b) gas-pressure sensing.

spectra. One can see that the locations of the major peaks in the FFT spectra agree well with the air cavity lengths obtained from the SEM images. There are three major peaks in the FFT spectra, as shown in **Figure 4.3 (d)** and **(f)**, when the FP micro-interferometers have relatively thick microbeams. This phenomenon is in accordance with the SU-8 FP cavities fabricated on fiber-optic ferrules which has been presented in Chapter 3 [202]. When the thickness of the suspended microbeam is sufficiently small, for instance, the FP cavity shown in **Figure 4.3 (b)** has a beam thickness of 1 μm, thus resulting in a merged single peak in the FFT's result as shown in **Figure 4.3 (e)**. A single major peak in the FFT spectrum indicates that only a two-beam interference is dominant in the FP micro-interferometers, which contributes to the suppression of fluctuation of the inference fringe in the reflection spectrum. From the positions of the major peaks in the FFT spectra, we can deduce the cavity lengths of the fiber-top micro-interferometers to be 29.3, 14.7, and 39.1 μm, respectively, which match the values measured from SEM images.

4.4.2 Refractive index sensing

The sensing of the refractive index of liquids filled in the FP cavity is demonstrated as one of the promising applications of the optical fiber-tip sensors. As discussed in Chapter 2, the wavelength of a resonance valley/peak in a FP cavity's interference spectrum can be calculated by using

$$\lambda_k = 2nL / k, \tag{4.1}$$

where n is the refractive index of the medium filled in cavity, L is the cavity length and k is the order of the spectral valley/peak. From this equation, one can see that if the refractive index of the liquid filled in the FP cavity increases, the monitored resonant valley/peak will shift to longer wavelength. Assuming the change of refractive index Δn is small, the shift of a tracked spectral valley/peak is

$$\Delta\lambda \cong (\lambda_k / n)\Delta n\,. \tag{4.2}$$

Figure 4.4 (a) shows the setup used to measure the fabricated optical fiber-tip sensor's response to the change of the refractive-index of

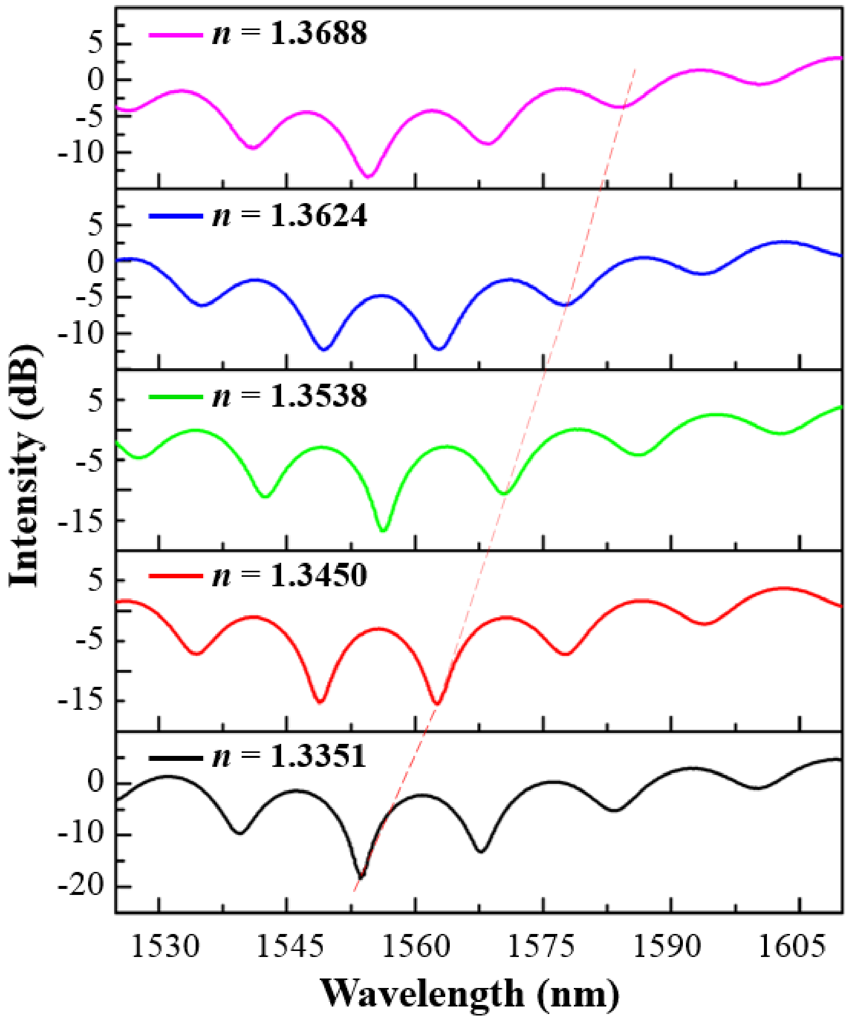

Figure 4.5. Measured reflection spectra of the optical fiber-tip sensor immersed into liquids with different refractive indices.

surrounding liquids. A series of $CaCl_2$ solutions with different refractive indices were used as the testing liquids by varying their concentrations. A commercial refractometer was employed to calibrate the refractive indices of these $CaCl_2$ solutions before test. The refractive indices of the $CaCl_2$ solutions used in the experiment ranged from 1.3351 to 1.3806. The fiber-tip sensor was immersed into $CaCl_2$ solutions with different refractive indices,

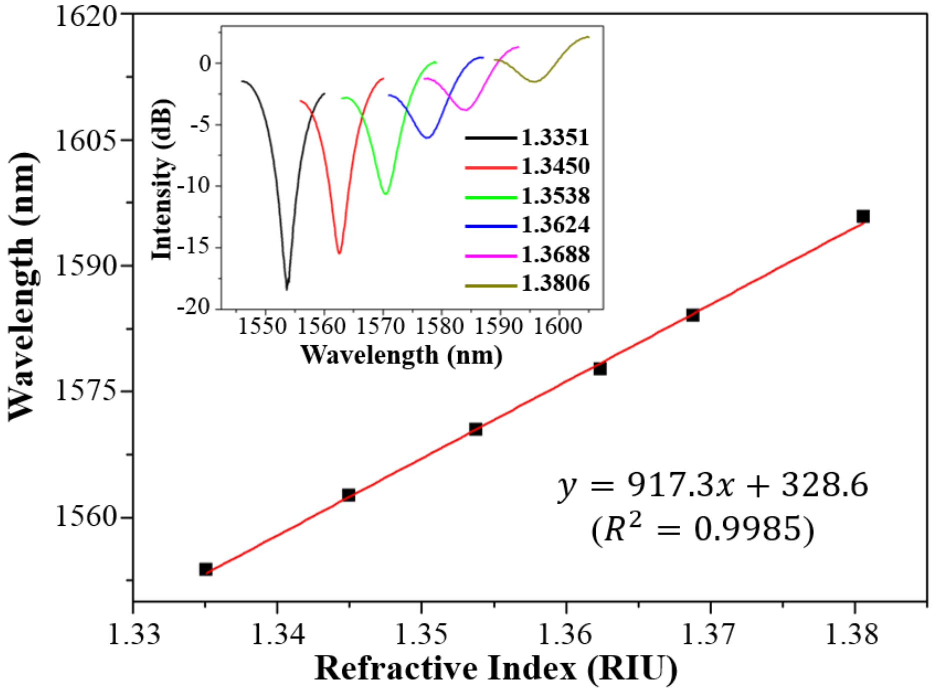

Figure 4.6. Response of a spectral dip of the optical fiber-tip sensor to the RI change of surrounding liquid. Inset shows the spectrum evolution of the spectral dip under monitoring.

after the interference fringe became stable, the reflection spectra were recorded. The fiber-tip sensor was kept still during the test to suppress possible displacement of the suspended microbeam induced by flowing liquid. After the measurement of each $CaCl_2$ solution, deionized water was used to rinse the fiber-tip sensor and then nitrogen flow was employed to dry out the sensor. During the test, the experimental setup was kept at room temperature to avoid interference induced by temperature fluctuation. **Figure 4.5** summarize the measured reflection spectra of the sensor when immersed in $CaCl_2$ solutions with different refractive indices. When the refractive index of the $CaCl_2$ solution was 1.3351, there was a resonant valley located at the wavelength of 1553.7 nm. This dip was tracked by a dash line in the reflection spectra and shifted to longer wavelength with increment of the refractive indices of the $CaCl_2$ solutions.

The relationship between the wavelength of the tracked resonant valley and the refractive index of the $CaCl_2$ solutions is plotted in **Figure 4.6**. A sensitivity of 917.3 nm/RIU estimated by linear regression was achieved, which is similar with the theoretically predicted sensitivity of 1159.4 nm/RIU by using Equation 4.2. Our optical fiber-tip RI sensor based on an open cavity has much higher sensitivity when compared with other optical refractive index sensors based on evanescent field [203, 204]. **Table. 2** summarize several types of optical fiber refractive index sensors. It's noteworthy that with the increase of the refractive index of the test liquid samples, the spectral valley gradually becomes shallower. It is because the decrease of the difference of their refractive indexes leads to the decay of Fresnel reflection at the interface between liquid and microbeam/fiber. Consequently, both the visibility of the interference fringe and the intensity of reflected light decrease.

Notably, there are multiple resonant peaks and valleys in the reflection spectrum, and the wavelengths of all these peaks/valleys shift when the refractive index of the test liquid changes, which makes it difficult to track a specific peak/valley. A wavelength-track method can be adopted to solve this issue. The effective cavity length L_{eff} can be calculated by using the FFT's result of the reflection spectrum, thus the order of the target resonant peak/valley to be tracked can be estimated by using $k = 2\,L_{eff} / \lambda_k$. When the reflection spectrum shifts due to the change of the medium's refractive index, the wavelength of the tracked resonant peak/valley can be calculated as $\lambda_{k\_new\_calculated} = 2\,L_{eff\_new} / k$, where L_{eff_new} is the effective cavity length deduced from the FFT's result of the shifted reflection spectrum. Then an optical spectrum analyzer or other spectrometric methods can be adopted to measure the wavelength λ_{k_new} of the specific resonant peak/valley. In this way, the wavelength of the target resonant peak/valley can be tracked in real time when the reflection spectrum shifts.

4.4.3 Gas pressure sensing

The remote monitoring the gas pressure in tiny space has also been experimentally demonstrated as another promising application of the optical

Table. 2 Performance summary of different types of optical fiber RI sensors.

Ref. No.	Types	Principle	Sensitivity	Dynamic range
190	fiber Bragg grating	evanescent field	300 nm/RIU	1.450 ~ 1.456
191	long period grating	LPG Michelson interferometer	160 nm/RIU	1.3 ~ 1.45
192	fiber-taper seeded LPG pair	LPG Mach-Zehnder interferometer	176 nm/RIU	1.33 ~ 1.36
193	thin-core fiber modal interferometer	mode mismatch	138 nm/RIU	1.33 ~ 1.39
194	Fabry Perot cavity	optical path	1130.887 nm/RIU	1.333 ~ 1.395
195	tapered optical fiber	evanescent field	6008 nm/RIU	1.337 ~ 1.347
197	localized surface plasmon resonance	collective oscillation	914 nm/RIU	1.33 ~ 1.4
our work	fiber-top suspended microbeams	optical path	917.3 nm/RIU	1.33 ~ 1.38

fiber-tip sensor. It's known that at room temperature (20 °C-25 °C), the refractive index of air can be related to pressure p (Pa) and temperature t (°C) as [205-207]

$$n_{air} = 1 + 2.8756 \times 10^{-9} \times p \frac{1 + 10^{-8}(0.601 - 0.00972 \times t) \times p}{1 + 0.003661 \times t}. \tag{4.3}$$

When the air pressure is below 1 MPa, the quadratic term p^2 is negligible. Assuming the cavity length is a constant, the air pressure change induced wavelength shift of the k^{th} order spectral valley/peak in the interference fringe can be expressed as

$$\Delta\lambda \cong \alpha \frac{\lambda_k}{n_{air}} \Delta p, \tag{4.4}$$

where the coefficient α can be calculated by

$$\alpha = \frac{2.8756 \times 10^{-9}}{1 + 0.003661 \times t}. \tag{4.5}$$

The coefficient α is calculated to be 2.679×10^{-9} /Pa at room temperature. From the equations described above one can see that an approximately linear relationship exists between the wavelength shift of the optical fiber-tip sensor's interference fringe and air pressure under the circumstance that the temperature remains the same.

Figure 4.4 (b) shows the setup used to measure the optical fiber-tip sensor's response to the change of gas pressure. A gas chamber whose gas pressure was controlled by a high-pressure nitrogen cylinder in association with a gas flow regulator, was employed to provide a series of gas pressure from 0 to 700 KPa with a step of 50 KPa. A commercial pressure meter located in the chamber was utilized as a reference to calibrate the gas pressure. During the test, the ambient temperature was kept at room temperature to avoid interference induced by temperature fluctuation. The response of the optical fiber-tip pressure sensor to the change of gas pressure is experimentally measured and depicted in **Figure 4.7**. As shown in the inset figure, the tracked valley shifted to longer wavelength when the gas pressure in the chamber increased. Indeed, the increase of the refractive index of the nitrogen gas induced by pressure change resulted in the red shift of the

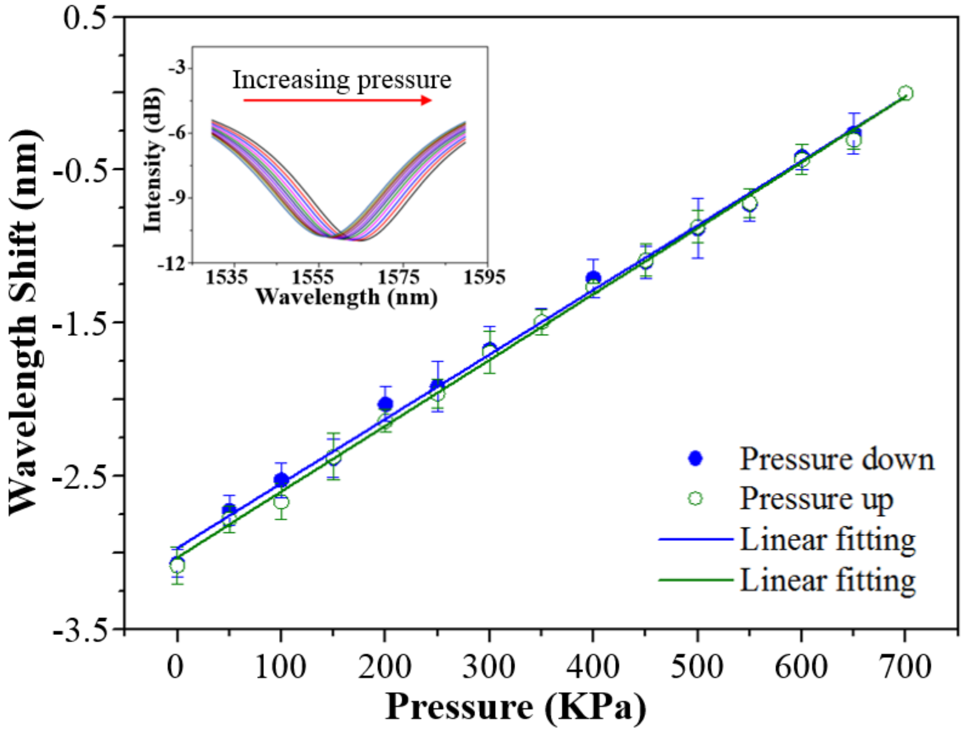

Figure 4.7. Response of a dip wavelength to the pressure change of the chamber where a fiber-tip suspended-microbeam sensor is placed. Inset shows the spectra evolution of the tracked resonance dip.

resonant valley in the reflection spectrum. The fiber-tip pressure sensor was tested with both increasement and decrease of gas pressure, the results showed good linearity and reversibility. The pressure sensitivity of the optical fiber-tip sensor is calculated to be 4.29 nm/MPa by linear regression, which is in accordance with the theoretically predicted value of 4.17 nm/MPa obtained by using Equation 4.4. Assuming the signal-to-noise ratio is 3, the detection limit of the optical fiber-tip gas-pressure sensor is estimated to be about 22.2KPa with a calculated noise level of 0.031 nm [208]. The pressure sensitivity of our open-cavity optical fiber-tip sensor is relatively low when compared with other diaphragm-based fiber-tip sensors due to different mechanisms, however, our sensor has a larger measurement range, which is favorable for applications where the air pressure is high. What's more, the open-cavity structure is more robust than cavity sealed by diaphragm under large pressure and fast variation of pressure.

4.5 Summary

In summary, we have managed to scale down the feature size of the 3D microstructures to fit the end-face of standard single-mode fiber via improving the optical 3D μ-printing technology. Ultrasmall fiber-top refractive-index sensor have been implemented by directly printing SU-8 suspended microbeams on the end-face of optical fiber to form FP micro-interferometers. The fiber-top FP cavities have been characterized by measuring their reflection spectra, and FFT has been adopted to analyze the reflection spectra to retrieve cavity information. The detection of refractive-index change of liquid and gas pressure have been experimentally demonstrated, respectively. The miniature fiber-tip sensor has shown a high sensitivity of 917.3 nm/RIU to refractive-index change, which surpasses other optical fiber refractive-index sensor based on other mechanisms such as evanescent field. The sensitivity to gas-pressure change is 4.29 nm/MPa, which is relatively low due to the pressure induced refractive index change of gas is small. Nevertheless, larger dynamic range and robustness are the advantages of our sensor. The tiny size, high sensitivity to refractive-index change, and remote detection capability of our optical fiber-tip sensor have made it a promising candidate for applications such as microfluidic biochemical-sensing where miniaturization is crucial. Moreover, due to the advantages of fiber-optic sensors such as electromagnetic immunity, our device is suitable for sensing applications in harsh environment.

Chapter 5

Ultracompact Optical Fiber Acoustic Sensors Based on In Situ μ-Printed Fiber-Top Optomechanical Microresonator

5.1 Introduction

Acoustic waves are mechanical waves with the frequencies ranging from infrasound (lower than 20 Hz) to ultrasound (above 20 kHz). Acoustic sensors working at different bands are usually designed and optimized for specific applications. A miniature acoustic sensor with broad bandwidth is usually desired, especially for ultrasonic detectors employed in industrial non-destructive testing and imaging. Ultrasonic waves have features such as good directionality, deep-penetration capability and long propagation distance [209]. For example, in photoacoustic imaging, the irradiation of modulated laser pulses onto biological tissues or organs will generate weak ultrasonic waves with broad bandwidth, which can be acquired by ultrasonic transducers for the reconstruction of the tissue's or organ's tomography [210]. Piezoelectric transducers are commonly used for the detection of ultrasonic waves. However, the high-sensitivity requirement leads to a centimeter-scale element size, which results in not only low lateral resolution but also poor signal-to-noise ratio and fidelity. What's more, the frequency response of piezoceramic materials-based transducers is typically not flat over the bandwidth of acoustic waves, thereby hindering the reconstruction of images [85]. Optical fiber-tip acoustic sensors are very attractive because of their miniature size and potential of ultrahigh sensitivity. The unique geometry of fiber tips, *i.e.*, tiny diameter with large aspect ratio, perfectly suits the applications where minimization is important, such as blood vessels and endoscopic photoacoustic imaging. Moreover, optical fibers are natural waveguides and can be easily connected with excitation light source and retrieve back the light-wave signal from fiber-tip acoustic sensor.

Fiber-optic acoustic sensors have been extensively investigated for various applications including homeland security [17, 211, 212], photoacoustic imaging [213, 214], photoacoustic spectroscopy [215, 216], photoacoustic endoscope [217] *etc*. because of their favorable features such as immunity to electromagnetic interference, light weight, remote sensing capability and multiplexing. Various schemes have been proposed to fabricate optical fiber acoustic wave sensors such as fiber-optic interferometers, fiber lasers [218], tapers [219], couplers [220] and long-period gratings [221]. Among these designs, fiber-optic interferometers have received remarkable attention owing to their simple structures and high sensitivity. In particular, optical fiber acoustic sensors based on fiber-tip Fabry-Pérot interferometers (FPIs) that are without the need of a long piece of optical fiber as required by Mach-Zehnder [222] and Michelson interferometers [223], have great potential in applications where minimization is crucial.

Conventional fiber-tip FPI acoustic sensors use an elastic diaphragm to form an air cavity together with the fiber end surface. Acoustic pressure deforms the thin film and changes the cavity length, which can be read out interferometrically. Various kinds of membranes ranging from polymer films to metallic diaphragms have been employed to fabricate acoustic transducers [56, 224-229]. Remarkably, two-dimensional material such as graphene [62] and molybdenum disulfide (MoS_2) [67] have shown impressive performance because of their ultrathin thickness and excellent mechanical strength. For a FPI acoustic sensor using circular diaphragm, the factors determining its sensitivity include the diameter, thickness and mechanical properties of the diaphragm. For a diaphragm with specific thickness and made from given material, the sensitivity of FPI acoustic sensor depends on the diameter of the diaphragm. One has to increase the diameter of the diaphragm if high sensitivity is demanded. However, the increase of the diaphragm's diameter will bring a negative influence on the miniaturization of the sensor. Here, we propose to solve the tradeoff by using fiber-top optomechanical microresonators with spirally suspended microbeams, as shown in **Figure 5.1 (a)**. The spiral structure can not only save space but also increase the effective length of the cantilever suspending the mirror in the center and thereby increase sensitivity of the acoustic sensor.

5.2 Design and analysis of SU-8 FPI acoutic sensor

5.2.1 Mechanical properties of SU-8 micromechanical resonator

As shown in **Figure 5.1 (a)**, a mirror that suspended with spiral microbeam is devised on the end surface of a standard single-mode optical fiber. An open air-cavity FP interferometer is formed by the suspended mirror and the end surface of optical fiber. The suspended microbeam will deform when acoustic pressure is applied on its surface, thus changing the length of FP cavity. The variation of the cavity length can be interferometrically demodulated to interrogate the incident acoustic pressure. Compared with diaphragm-based FPI acoustic sensor, the deflection of the center of the suspended mirror under given acoustic pressure will be much larger because of the structure of relatively long spiral micro-beam. As a consequence, higher sensitivity can be achieved on such an ultra-small fiber-end surface.

5.2.2 Frequency response of the micromechanical resonator under acoustic wave

The frequency response of such fiber-top spirally suspended mirrors has been numerically analyzed. The fundamental frequencies of the sensors are

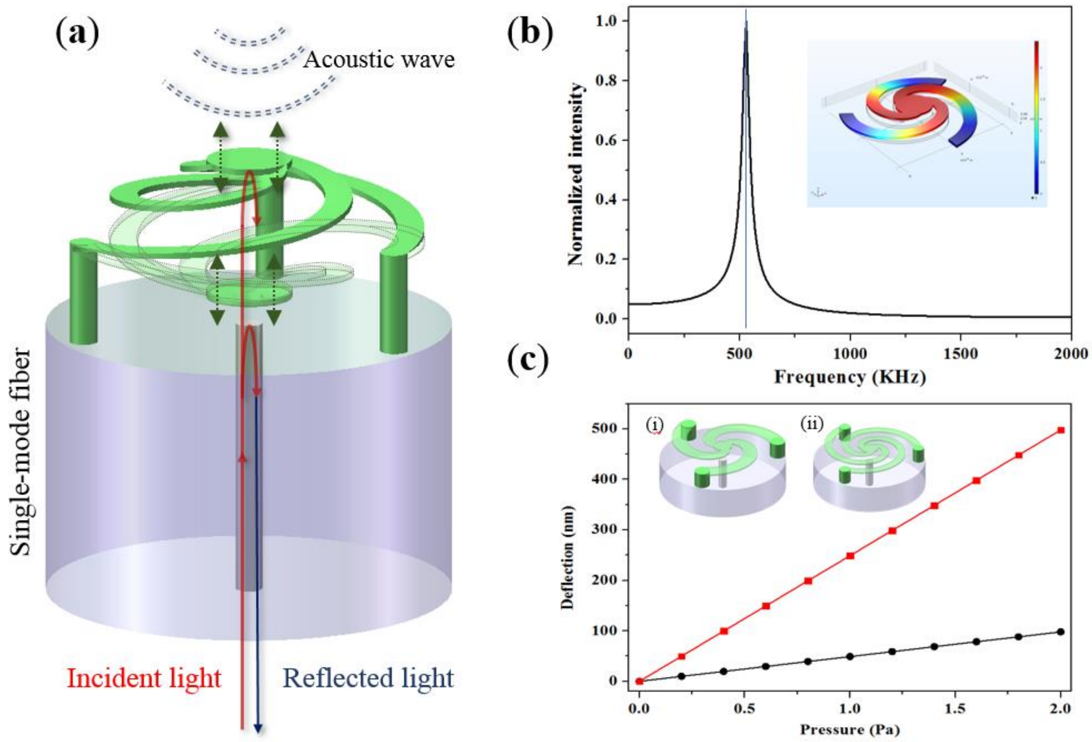

Figure 5.1. (a) Schematic diagram of the fiber-optic acoustic sensor. **(b)** Frequency response of the sensor shown in **(a)**. Inset shows the mode shapes of fundamental mode. **(c)** Defection of the two types of spirally suspended mirrors under different acoustic pressure at the fundamental frequencies of the microstructures: **(i)** and **(ii)** 3D models of two types of fiber-tip spirally suspended mirrors with different geometries.

at ultrasonic band, the theoretical analysis is focused on the response to high frequencies (from 100 kHz to 1 MHz).

To understand the frequency response of the device, one can consider the fiber-top cantilever with beam length L, width b, and thickness h, and its response to acoustic waves. Since the loss of ultrasonic waves in air is higher than that in water, we consider the response of the fiber-top cantilever immersed in water. The deflection of the beam $w(x, t)$ can then be described by [230]

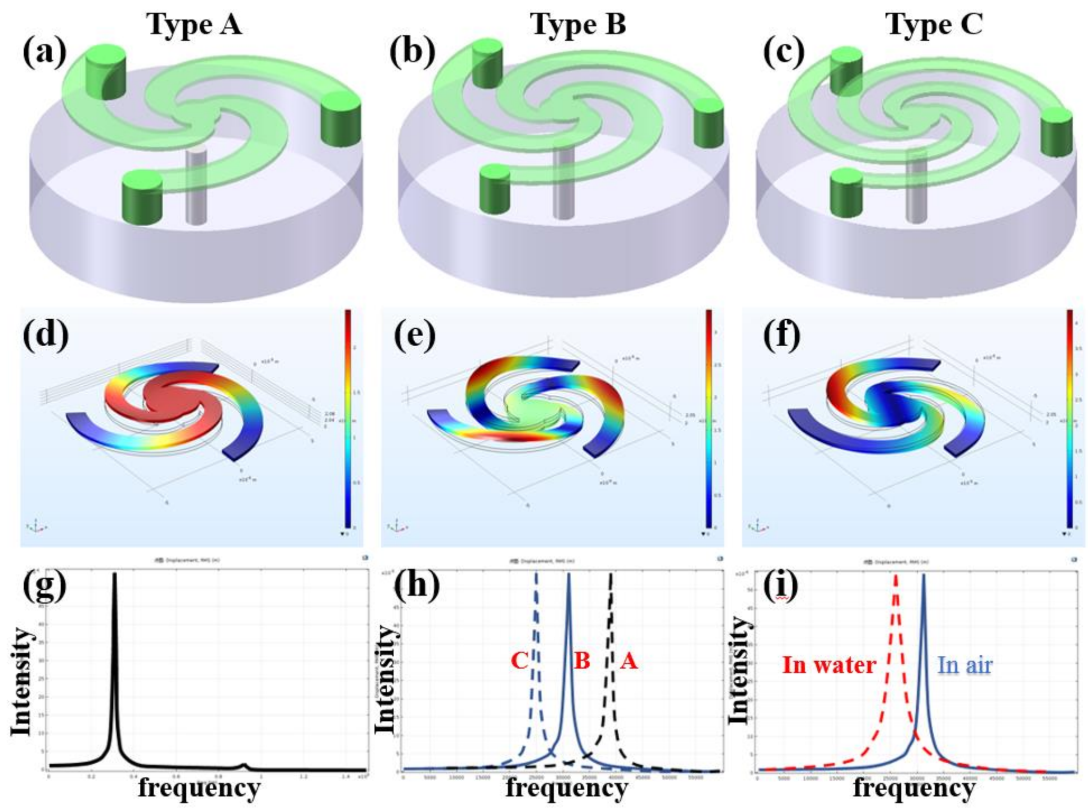

Figure 5.2. (a), **(b)** and **(c)** show the 3D models of three fiber-top spiral-shape suspended mirrors with different beam lengths and widths. **(d)**, **(e)**, and **(f)** depict the first three modes of the microstructure's mechanical resonance, respectively. The frequency response showing two resonance frequencies is plotted in **(g)**. The eigenfrequencies of the three microstructures shown in **(a)**, **(b)** and **(c)** are plotted in **(h)**. **(i)** shows the shift of fundamental frequency when the microstructure is immersed in water.

$$EI\frac{\partial^4 w(x,t)}{\partial x^4}+\mu\frac{\partial^2 w(x,t)}{\partial t^2}=F(x,t), \tag{5.1}$$

where E represents Young's modulus and I is the moment of inertial of the beam's cross section. μ is the mass per unit length of the beam and $F(x, t)$ represent the external force applied on the cantilever beam. t and x are the time and spatial variable, respectively.

The boundary conditions for the cantilever beam include: (a) the displacement of the fixed point is zero, *i.e.*, $w(0, t) = 0$; (b) the derivative of the displacement of the fixed point is zero; (c) the second-order derivative of the free end is zero; (d) the third order derivative of the free end is zero.

Scaling the spatial variable x with the beam length L and then applying Fourier transform to Equation 5.1, we can obtain

$$\frac{EI}{L^4}\frac{d^4\hat{W}(x,\omega)}{dx^4} - \mu\omega^2\hat{W}(x,\omega) = \hat{F}(x,\omega). \tag{5.2}$$

The external force can be decomposed into two parts

$$\hat{F}(x,\omega) = \hat{F}_{hydro}(x,\omega) + \hat{F}_{drive}(x,\omega), \tag{5.3}$$

where $\hat{F}_{drive}(x,\omega)$ is the excitation acoustic force. Assuming the diving force has a single frequency and the distribution of this force on the cantilever beam is uniform, it can be simplified as $\hat{F}_{drive}(x,\omega) = A$, where A is the amplitude of the exciting force. $\hat{F}_{hydro}(x,\omega)$ represents the hydrodynamic resistance described as

$$\hat{F}_{hydro}(x,\omega) = \frac{\pi}{4}\rho\omega^2 b^2 \Gamma(\omega)\hat{W}(x,\omega), \tag{5.4}$$

where ρ is the density of water and Γ(ω) is the hydrodynamic function. Substituting Equation 5.3 and 5.4 into Equation 5.2, the deflection $\hat{W}(x,\omega)$ can be solved as

$$\hat{W}(x,\omega) = \int_0^L G(x,x'\,|\,\omega)\frac{AL^4}{EI}dx', \tag{5.5}$$

where $G(x,x'\,|\,\omega)$ is Green's function.

Considering the geometric complexity of the spiral microstructures, FEM is adopted to analyze the eigenfrequency and frequency response of the polymer optomechanical resonator. **Figure 5.2 (a)**, **(b)** and **(c)** illustrate the 3D models of three spirally suspended optomechanical resonators with different lengths and widths of the suspending beam. The sketch of the spiral curves can be represented by the following parametric equations

$$\begin{cases} x = \alpha \cdot (t + \beta) \cdot \sin(\gamma \cdot t + \theta) \\ y = \alpha \cdot (t + \beta) \cdot \cos(\gamma \cdot t + \theta) \end{cases} \tag{5.5}$$

where α, β, γ, and θ are parameters defining the shape of the spiral curve. The geometric structures and stress distributions of the first three mechanical resonance modes of the microstructure shown in **Figure 5.2 (b)** are illustrated in **Figure 5.2 (d)**, **(e)** and **(f)**, respectively. For the fundamental

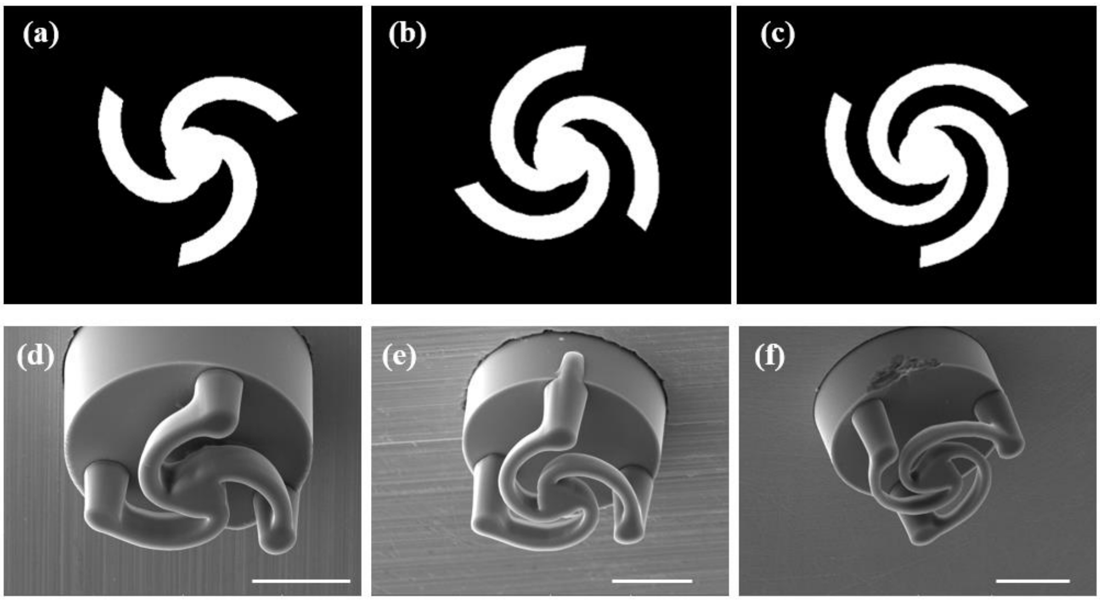

Figure 5.3. (a), (b) and **(c)** show the patterns used for the printing of different types of spiral-shape suspended mirrors. **(d)**, **(e)** and **(f)** shows the SEM images of the fabricated fiber-tip sensors as the design shown in **Figure 5.2 (a)**, **(b)** and **(c)**, respectively.

mode, the central part vibrates vertically while twists occur in the second and third modes. The frequency response with the first two resonance peaks is plotted in **Figure 5.2 (g)**. The amplitude of the fundamental mode is much larger than that of the high order mode. The eigenfrequencies of the three microstructures shown in **Figure 5.2 (a)**, **(b)** and **(c)** are plotted in **Figure 5.2 (h)**, which shows that the fundamental frequency decreases with the increase of the effective length of the spiral beam. **Figure 5.2 (i)** shows a blue shift of the fundamental frequency when the optomechanical resonator is moved from air to water. As expected, the simulation results show that the frequency response of such a device can be tailored by changing the geometries of microstructure without changing the outer diameter of the device. The Young's modulus and Poisson ratio of SU-8 used for FEM simulation is 4.0 GPa and 0.22, respectively. The thickness of the microbeams and micro-disk of the microresonators is about 10 μm and the lengths of microbeams shown in **Figure 5.2 (a)**, **(b)** and **(c)** are 77, 106, and 198 μm, respectively.

5.3 Fabrication of the fiber-tip SU-8 FPI acoustic sensor

SU-8 2100 (Microchem Corp.) was diluted by cyclopentanone to the concentration of 15 %. Tributylamine was mixed into the SU-8 solutions as inhibitor at a weight ratio of 0.056 % which can improve the spatial resolution of the optical μ-printing process. 2-(2H-Benzotriazol-2-yl)-4,6-bis (1-methyl-1-phenylethyl)phenol, also known as Tinuvin 234, which is a widely used UV absorption agent to limit the light penetration, was added into the solutions for enhancement of the vertical resolution of the optical 3D μ-printing process.

The fabrication processes of optical 3D μ-printing technology is similar to that described in Section 4.2, as shown in **Figure 4.2 (a)**. In brief, a uniform thin layer of SU-8 was spray coated to the cleaved end-face of a standard single-mode optical fiber mounted on a XY-axis motorized translation stage. To obtain high quality films with precise thickness control, an ultrasonic nozzle was employed to perform the spray coating. A scanning process, *i.e.*, the fiber tip was moved forth and back by the motorized stage at a certain velocity, was adopted to achieve uniform coating. The thickness of an individual layer of SU-8 film can be customized by the concentration of the solution, the pumping rate of the syringe pump which pumps SU-8 solutions to the nozzle, the scanning velocity and the distance between the nozzle and the fiber tip, and the gas pressure applied to the ultrasonic nozzle. Good repeatability and precise thickness control have been achieved in the experiments. After coating of a layer of SU-8, extra solvent was in situ evaporated by a ceramic heater embedded in the customized mount of optical fiber. After baking, the sample was moved by using motorized stage to the pre-aligned position for exposure process, with the assistance of the digital camera-based machine vision metrology. Thereafter, the image data sliced from the CAD model of the 3D microstructure by own-developed add-on software was used to generate optical patterns to irradiate the SU-8 film on the optical fiber end-face. The patterns for the exposure of the top layer of optomechanical resonator are shown in **Figure 5.3 (a), (b)** and **(c)**. The typical exposure time for the mirrors was about 10 seconds which is associated with the power density of 25.28 mw/cm^2. After exposure, the sample was in situ post-baked by using the integrated digital micro-heater. The processes were automatically repeated for the fabrication of the next layer of 3D microstructure. Finally, the sample was developed by using propyleneglycol monomethylether acetate (PGMEA). The development time was about 15 minutes. The SEM images of the fabricated structures are shown in **Figure 5.3 (d)**, **(e)** and **(f)**. The scale bar is 50 μm.

5.4 Testing of the fabricated optical fiber-tip acoustic sensor

5.4.1 Spectra of the optical fiber-tip acoustic sensors

The refection spectra of the fabricated fiber-top optomechanical resonator were measured in air by using an own-established experimental setup with a broadband light source, a circulator and an optical spectrum analyzer. FFT is used to analyze the reflection spectra. The FFT's results show two typical

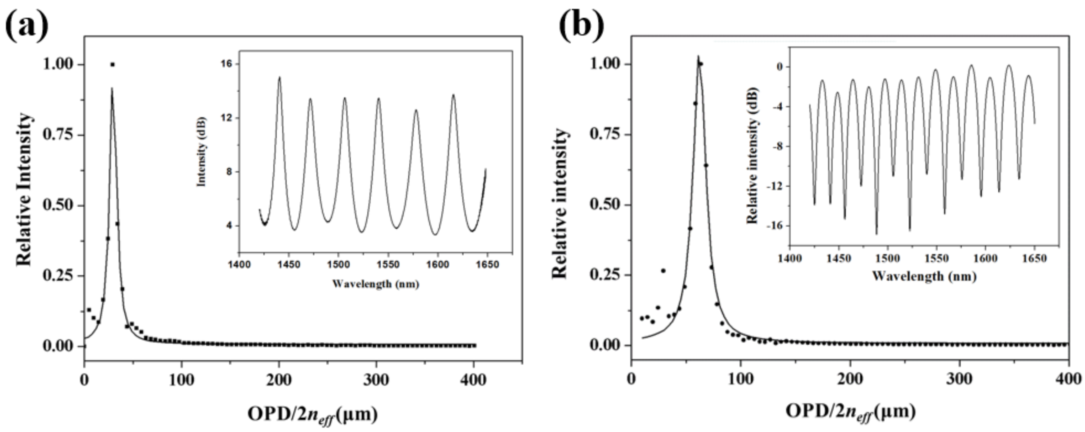

Figure 5.4. (a) Reflection spectrum of the fiber-tip acoustic sensor. (b) FFT's results of the reflection spectrum.

fiber-top FPIs cavities with distinguishing lengths, as shown in **Figure 5.4**, while the corresponding refection spectra are shown in the inset figures. To

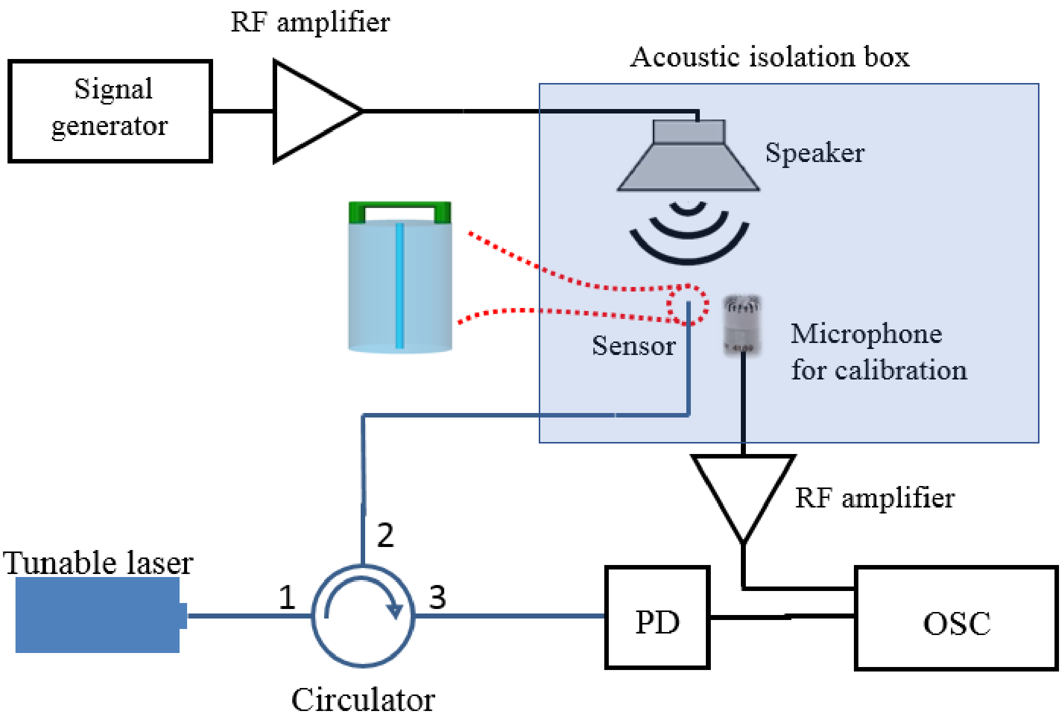

Figure 5.5. Schematic diagram of experimental setup for acoustic pressure measurement.

achieve larger dynamic range of measurement and higher sensitivity, the quadrature point of the interference fringe with sharpest slope was chosen as the operation point in the following test.

5.4.1 Testing results

The experimental setup for testing of the fiber-tip acoustic sensor's response to acoustic wave is shown in **Figure 5.5**. A speaker driven by an arbitrary waveform generator is used to generate the excitation acoustic waves. A tunable laser is used as the interrogation light source and its

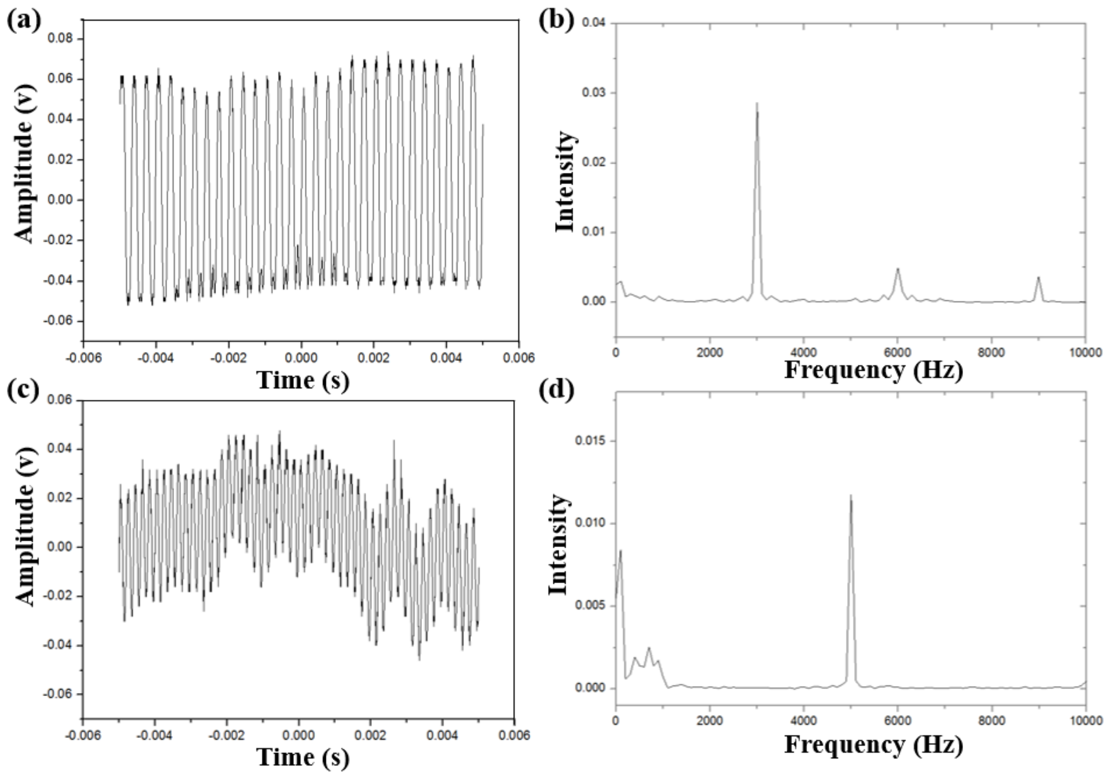

Figure 5.6 (a) and **(c)** shows the raw data representing the time domain response of the fiber-tip sensor to 3000 Hz and 5000 Hz excitation, respectively. **(b)** and **(d)** shows the FFT's results of the time-domain signal.

wavelength is set to the quadrature point so as to maximum the sensitivity of the sensor. The reflected light is coupled to a photodiode (PD) via a circulator and the light intensity variation is converted to an electric signal which is analyzed by an oscillator. A commercial microphone (B&K4189) was mounted to place near the fiber-tip sensor to calibrate the acoustic waves. The output signal from the calibration microphone is amplified by a conditioning amplifier and then detected by the oscillator. During the test, the speaker, fiber-tip sensor and calibration microphone all are putted in an

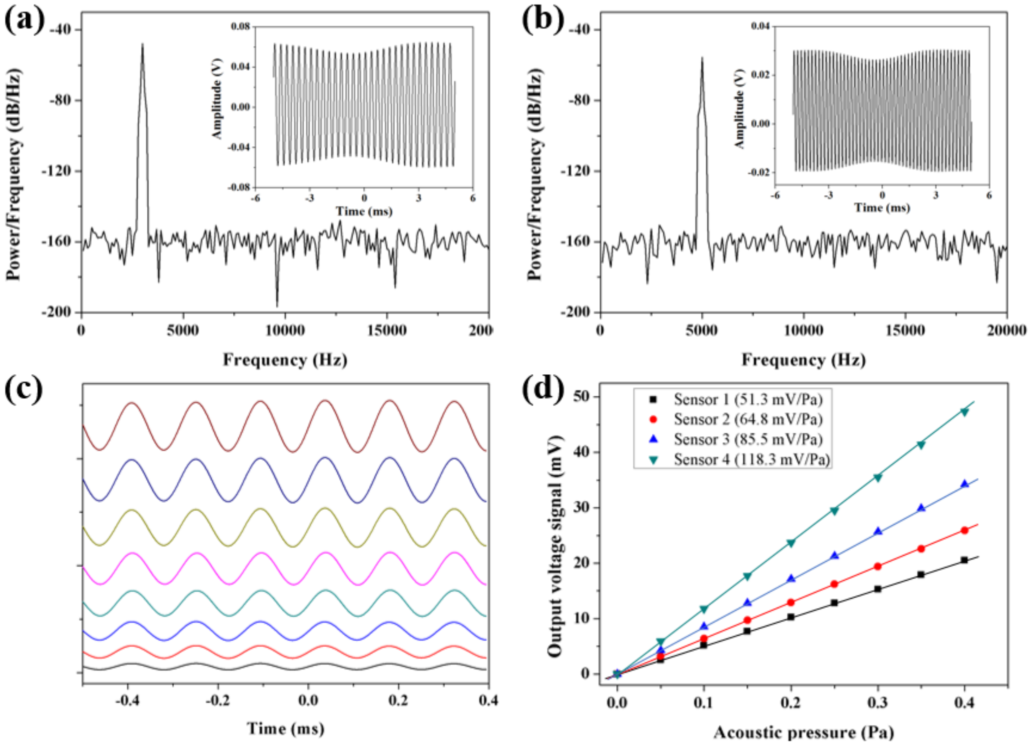

Figure 5.7 (a) and **(b)** Power densities spectra of the output voltage signals acquired form the PD when acoustic waves with frequencies of 3 kHz and 5 kHz are applied to the sensor. **(d)** Relationships between output voltage signals and applied acoustic pressure of four sensors. The time domain signals under different excitation acoustic pressures of sensor 4 is shown in **(c)**.

acoustic isolation box to depress the influence from external environment.

Figure 5.6 (a) and **(c)** depicts the raw data acquired from the PD when sinusoidal acoustic waves with frequency of 3000 Hz and 5000 Hz are applied, respectively. The corresponding frequency domain spectra are shown in **Figure 5.6 (b)** and **(d)**. It can be seen that the frequencies of the major peaks are in accordance with the excitation frequencies, which verify that the measured signals resulted from the excitation signals and can be demodulated to quantitatively analyze the acoustic waves. Slow-varying noises are observed in **Figure 5.6 (c)**, which may result from the disturbance in laser power. A band-pass filter can be utilized to eliminate the noise to increase signal-noise-ratio.

The power density spectra of the filtered output signals under the excitation of 3000 Hz and 5000 kHz are shown in **Figure 5.7 (a)** and **(b)**, respectively. Inset figures depict the corresponding measured time-domain signals. Acoustic waves of different intensities have been used to test the optical fiber-tip acoustic sensors and the corresponding output signals were recorded. Four optical fiber-tip acoustic sensors with different beam thicknesses have been tested and the measured signal vs. acoustic pressure plots are shown in **Figure 5.7 (d)**. All these four sensors belong to type C as shown in **Figure 5.2 (c)**. The length of microbeams is about 198 μm, while the thicknesses their microbeams and micro-disk are 15.2 μm, 13.5 μm, 10.3

μm and 7.1 μm, respectively. The output signals of sensor-4 under different acoustic pressures are plotted in **Figure 5.7 (c)**. A band-pass filter was used to suppress noises. Compared with the raw data shown in **Figure 5.6 (a)** and **(c)**, the measured data has higher quality of sinusoidal waveform. A linear relationship has been measured between the amplitude of output signal and the acoustic pressure, which is in line with the theoretical analysis under the condition that the induced deflection of the microstructure is small. Four sensors with different thicknesses showed different sensitivities, and the highest acoustic pressure sensitivity is determined to be 118.3 mV/Pa and the corresponding noise equivalent acoustic signal level is estimated to be 0.328 $\mu Pa/Hz^{1/2}$. **Table. 3** summarize several types of optical fiber acoustic

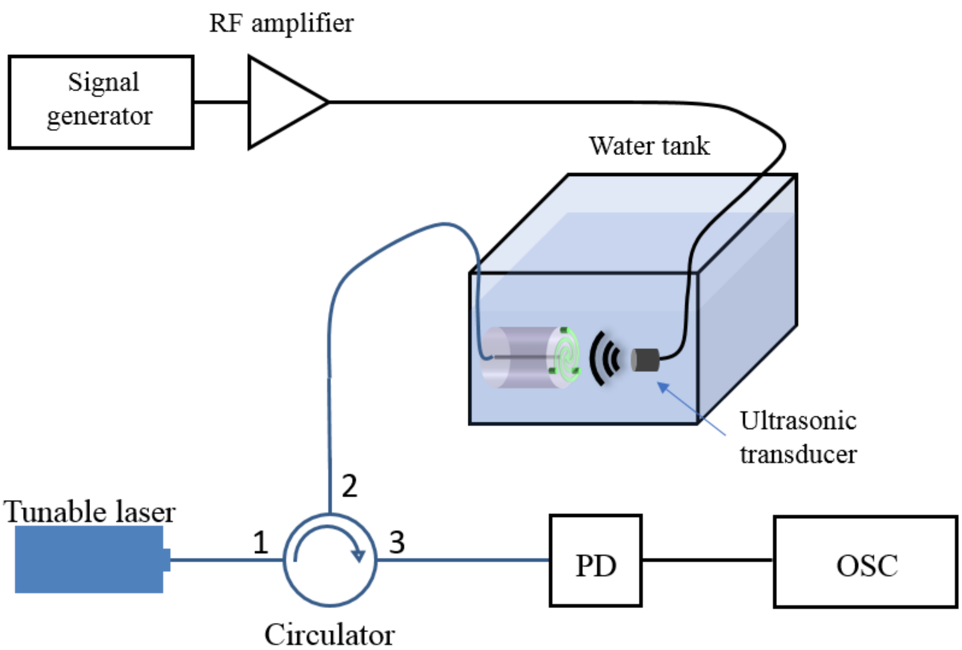

Figure 5.8 Experimental setup for the measurement of the fiber-tip sensor's frequency response.

sensors.

Table. 3 Performance summary of different types of optical fiber acoustic sensors.

Ref. No.	Material	Geometry	Frequency	Sensitivity	Detection limit
56	silver	diaphragm	4 kHz	160000 μm/MPa	14.5 $\mu Pa/Hz^{1/2}$
62	multilayer graphene	diaphragm	10 kHz	1100 μm/Mpa	60 $\mu Pa/Hz^{1/2}$
66	graphene oxide	diaphragm	20 kHz	-	1.8 $\mu Pa/Hz^{1/2}$
140	polymer	diaphragm	1 kHz	50.8 μm/Mpa	-
225	UV adhesive	diaphragm	1 kHz	57.3 mV/Pa	52.4 $\mu Pa/Hz^{1/2}$
228	polymer	diaphragm	40 kHz	10.4 μm/Mpa	-
85	polymer	plano-concave microresonator	1 ~ 40 MHz	-	1.6 $mPa/Hz^{1/2}$
50	stainless steel	cantilever	1 kHz	364000 μm/MPa	8.5 $\mu Pa/Hz^{1/2}$
229	fused silica	cantilever	0.74 MHz	9.75 μm/MPa	491.2 Pa
our work	SU-8 polymer	spirally-suspended microresonator	0.1 ~ 100 kHz	182 μm/MPa	0.328 $\mu Pa/Hz^{1/2}$

The frequency response of an acoustic sensor is an important property which determines its sensing performance and applicable frequency range for acoustic measurement. According to the FEM simulation results, the fundamental frequencies of the optical fiber-tip sensors are between several hundred kHz to 1 MHz. As speakers designed for audio frequency are not able to generate ultrasonic waves with sufficient amplitude, a broadband ultrasonic transducer whose resonance frequency is 1 MHz is employed to generate ultrasound waves to excite the fiber-tip sensors. Since the attenuation of ultrasonic waves in air is high, the test was conducted in water. The experimental setup for the measurement of frequency response is shown in **Figure 5.8**. The sensor under test was immersed in a water tank and an ultrasonic transducer was placed close to it. Sinusoidal signals from a signal generator are used to drive the ultrasonic transducer after radio frequency

(RF) amplification. The ultrasonic waves propagate in water for a short distance and then hit against optomechanical resonator. The ultrasonic transducer is aligned with the axis of the fiber and the distance between the surface of the transducer and the optical fiber-tip sensor can be adjusted. Similar to the readout apparatus used for audio acoustic wave detection, the intensity variation of reflected light is converted to electric signal as shown in **Figure 5.9 (a)**. The frequency of the ultrasonic wave is 500 kHz, which matches the frequency of the output signal as shown in **Figure 5.9 (b)**. The

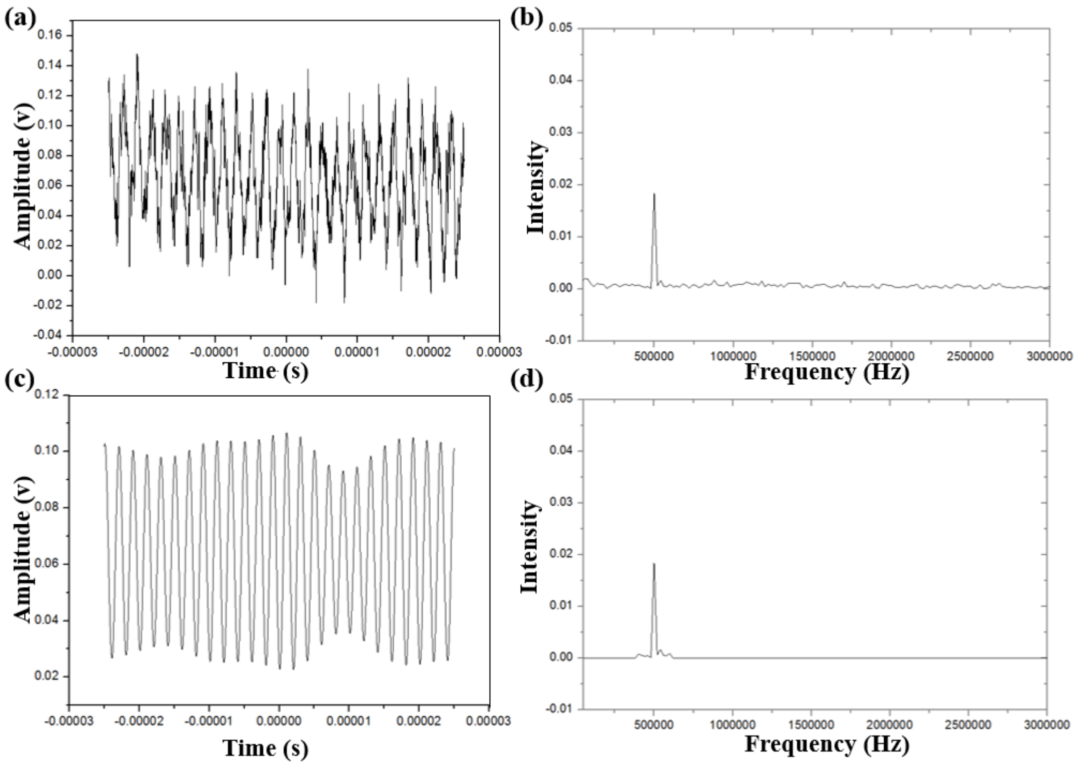

Figure 5.9 (a) The output signal corresponding to 500 kHz ultrasonic wave excitation. The filtered result is shown in **(c)**. **(b)** and **(d)** show the FFT's results of the signals in **(a)** and **(c)**, respectively.

output signals can be improved by using a band-pass filter with central

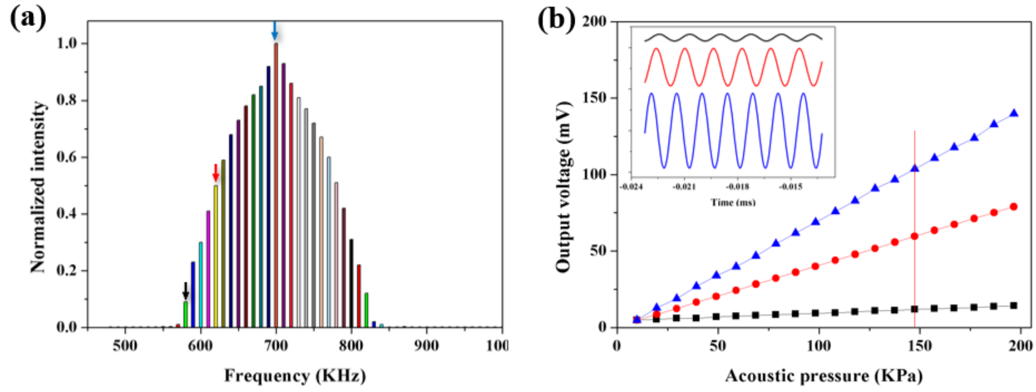

Figure 5.10 (a) The measured frequency response of a fiber-tip acoustic sensor. **(b)** Acoustic pressure versus output signal amplitude at different excitation frequencies. Inset shows the time-domain signals when excitation acoustic waves with different frequencies and equal pressure are applied to the sensor.

frequency of 500 kHz, and the results are shown in **Figure 5.9 (c)** and **(d)**. The sensor under test belongs to type B, as shown in **Figure 5.2 (b)**. Its beam length is 106 μm and the thickness of its microbeams and micro-disk is 10.1 μm. The relatively heavy noise may result from laser power fluctuation, PZT transducer used for the generation of ultrasonic waves, the imperfection of the microresonator microstructure and so on.

To obtain the frequency response of the optical fiber-tip sensor, a serial of ultrasonic waves with different frequencies but same intensities are used to test the sensor. The frequency was swept from 20 kHz to 1 MHz with a step of 50 kHz. A finer step of 10 kHz is used around the resonant frequency. The measured frequency response normalized by the frequency spectrum of the transducer is shown in **Figure 5.10 (a)**. A resonant peak was observed at

700 kHz, which matches well the FEM simulation result, i.e., 724 kHz. The relationship between the acoustic pressure and amplitude of output signal was measured as plotted in **Figure 5.10 (b)** at three different excitation frequencies. One can see that the sensitivity of the optomechanical resonator to acoustic waves can be greatly enhanced when its frequency of acoustic wave is the same as the fundamental resonant frequency of the optomechanical resonator. It is because the acoustic wave excited resonance of the resonator can greatly increase the amplitude of the induced vibration. The inset figures show the measured time-domain signals when the sensor was excited by the acoustic wave at the three frequencies. The frequency response of three optomechanical resonators with different geometries have

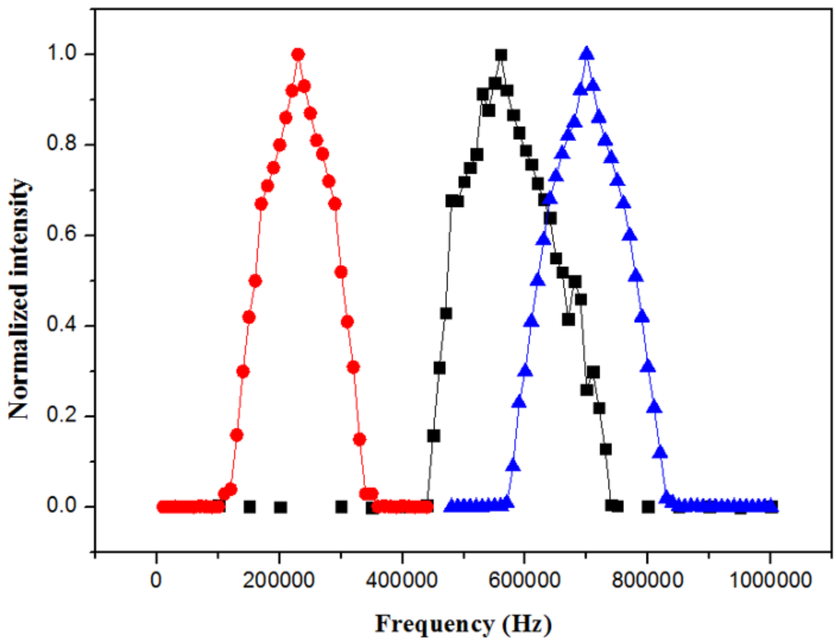

Figure 5.11 Frequency response of three fiber-tip acoustic sensors with different geometries.

been measured and the measured results are shown in **Figure 5.11**. The fundamental frequency of these three sensors are measured to be 230 kHz, 560 kHz and 700 kHz, respectively. The results indicate that the frequency response of the optomechanical resonators can be flexibly tuned by customizing the geometry of the spiral beams.

5.5 Summary

Novel optical fiber-tip acoustic sensors based on fiber-top optomechanical microresonators have been designed and fabricated by using optical 3D μ-printing technology. The structure of spiral microbeams has been adopted to overcome the limitations existing in conventional diaphragm-based fiber-tip FPI acoustic sensors, *i.e.*, the small area of optical fiber-end surface is fully used to enhance the sensitivity without increasing the size of the sensor. A high sensitivity of 118.3 mV/Pa at audio frequency has been achieved and the corresponding noise equivalent acoustic signal level is estimated to be 0.328 $\mu Pa/Hz^{1/2}$. Moreover, the frequency response of the optical fiber-tip sensors has been theoretically analyzed and experimentally measured. Fundamental resonance has been observed and the enhanced sensitivity has been demonstrated by setting the frequency of the excitation acoustic wave to the fundamental frequency of optomechanical resonators. Such an optomechanical resonator sensor provides a new pathway for development of high-sensitivity ultrasmall optical fiber acoustic sensors for various applications.

Chapter 6

Conclusions and Future Outlook

6.1 Conclusions

In this thesis, with an in-house optical 3D μ-printing technology, different kinds of optical fiber sensors based on the microstructures that are fabricated on the end surface of fiber-optic ceramic ferrule and standard single-mode fiber are developed. This technology can overcome the limitations of conventional micro/nano-fabrication technique on micromachining optical fibers and enables flexibly 3D microengineering of optical fiber end-surfaces to harness the magic power of lightwave technology at micrometer scale for development of small-size & high-performance optical fiber-tip sensors. The optical 3D μ-printing technology has programmable virtual 'photomask', which spares expensive photomasks and shortens development cycle. What's more, the system has favorable in situ microfabrication capability, which is crucial for the implementation of 3D microstructures on the end-surface of optical fibers. However, there is still space for further improvement of the optical 3D μ-printing technology. For instance, the resolution can be further improved towards nanofabrication.

Three types of miniature optical fiber/ferrule-top sensors have been fabricated by using the optical 3D μ-printing technology. First of all, different kinds of suspended-mirror devices (SMDs) are directly printed on the end-faces of optical fiber ferrules by using the optical 3D μ-printing technology. The reflection spectra of the ferrule-top SMDs have been measured and then numerical analyzed by using fast Fourier transform to characterize the SMDs. The application of the fabricated ferrule-top SMD as a displacement microsensor has been experimentally demonstrated. The optical microfabrication technology can rapidly print complex 3D SMDs on the end-faces of optical fiber ferrules, which is promising for the development of miniature photonic sensors and applications.

Then efforts have been made to scale down the microstructures from ferrule-top to fiber-top. By incorporating an ultrasonic nozzle-based spray coating system, suspended diaphragms are successfully printed on the flat tip of a standard single-mode optical fiber. The reflection spectra of the fiber-tip devices have been measured and used to analyze the Fabry-Pérot cavities formed by suspended microbeams. The optical fiber-tip sensors have been demonstrated to detect the RI change of liquid and the gas pressure of ambient environment, respectively. High sensitivities of 917.3 nm/RIU to RI change and 4.29 nm/MPa to gas-pressure change have been achieved. Such ultra-small optical fiber-tip sensors with remote sensing capability are very promising in microfluidic biosensing and environmental monitoring applications

Moreover, optomechanical microresonators have been designed and directly printed on the end-face of optical fibers. Ultracompact optical fiber acoustic sensors are experimentally demonstrated based on the mechanism that the spiral-shape microbeams deform under acoustic pressure, thus changing the cavity length of the Fabry-Pérot cavity formed by the fiber end-face and suspended mirror which can be interferometrically readout. The mechanical resonance of the fiber tip sensor is analyzed by FEM method. The response of the sensor to both acoustic waves and ultrasonic waves are measured. Frequency response is also measured, and fundamental resonance is observed. The fabricated sensor shows a high sensitivity of 118.3 mV/Pa at audio frequency and a corresponding noise equivalent acoustic signal level of 0.328 $\mu Pa/Hz^{1/2}$.

6.2 Future Outlook

SMDs are useful tools to study the optomechanical resonant interactions. However, the fabricated SMDs suffer from low finesse due to the low reflectivity of the interfaces between fiber/air and suspended SU-8 diaphragm/air. By depositing metal to the interfaces, the reflectivity can be enhanced as well as the Q-factor of the cavity. Another approach is to fabricate suspended plano-concave mirrors instead of planar ones to improve the confinement of light by refocusing the diverging beam back into the optical cavity. It’s very attractive to fabricated high Q SMDs on the fiber tip since the same optical fiber can be used to guide the probe light and the reflected light, which provide a compact platform to investigate optomechanical phenomena.

Suspended SU-8 diaphragm has already been printed on the endface of single-mode optical fiber. If the diaphragm is coated with functional materials, a lot of miniature sensors can be developed. For example, hydrogen sensor can be made by depositing the SI-8 diaphragm with Pd because Pd expands when absorbing hydrogen, which will induce deflection of the suspended diaphragm. What’s more, biosensor can be fabricated by modifying the diaphragm. The integration of the fiber-tip suspended diaphragm with microfluidic chips is another interesting research topic, which fully take advantage of the miniature size and remote sensing ability of optical fiber.

Although the sensitivity of the fiber-tip acoustic sensor is high compared with others, the detection limit is still relatively large because the thickness of the spiral-like beam is high. The sensitivity and detection limit of the sensor can be further enhanced by decreasing the thickness of the beam. Besides optimization of the exposure doze and UV dye concentration, the mechanical strength of SU-8 need to be improved by filling the photoresist solution with nanoparticles, e.g., silica nanoparticle. The Young’s modulus of SU-8 is much smaller than that of metal or inorganic materials such as silica and silicon, which make SU-8 suspended beam more sensitive to pressure. However, current printing process is not able to fabricate ultrathin SU-8 structures, which restricts further improvement of sensitivity. Fiber-top suspended microstructures which vibrate at their resonant frequencies can be employed to develop highly sensitive sensors by tracking the shift of resonant frequency introduced by the attachment of small weight objects such as molecules and cells.

Reference

1. J. M. López-Higuera, *Optical sensors* (Ed. Universidad de Cantabria, 1998).
2. V. M. N. Passaro, C. D. Tullio, B. Troia, M. L. Notte, G. Giannoccaro, and F. D. Leonardis, "Recent Advances in Integrated Photonic Sensors," Sensors **12**, 15558-15598 (2012).
3. J. Haus, *Optical sensors: basics and applications* (John Wiley & Sons, 2010).
4. X. D. Hoa, A. G. Kirk, and M. Tabrizian, "Towards integrated and sensitive surface plasmon resonance biosensors: A review of recent progress," Biosensors and Bioelectronics **23**, 151-160 (2007).
5. F. J. Blanco, M. Agirregabiria, J. Berganzo, K. Mayora, J. Elizalde, A. Calle, C. Dominguez, and L. M. Lechuga, "Microfluidic-optical integrated CMOS compatible devices for label-free biochemical sensing," Journal of Micromechanics and Microengineering **16**, 1006-1016 (2006).
6. R. Horváth, H. C. Pedersen, N. Skivesen, D. Selmeczi, and N. B. Larsen, "Optical waveguide sensor for on-line monitoring of bacteria," Opt. Lett. **28**, 1233-1235 (2003).
7. C. A. Barrios, K. B. Gylfason, B. Sánchez, A. Griol, H. Sohlström, M. Holgado, and R. Casquel, "Slot-waveguide biochemical sensor," Opt. Lett. **32**, 3080-3082 (2007).
8. A. D. Kersey, M. A. Davis, H. J. Patrick, M. LeBlanc, K. P. Koo, C. G. Askins, M. A. Putnam, and E. J. Friebele, "Fiber grating sensors," Journal of Lightwave Technology **15**, 1442-1463 (1997).
9. L. Rindorf, J. B. Jensen, M. Dufva, L. H. Pedersen, P. E. Høiby, and O. Bang, "Photonic crystal fiber long-period gratings for biochemical sensing," Optics Express **14**, 8224-8231 (2006).
10. Y. Miao, B. Liu, H. Zhang, Y. Li, H. Zhou, H. Sun, W. Zhang, and Q. Zhao, "Relative Humidity Sensor Based on Tilted Fiber Bragg Grating With Polyvinyl Alcohol Coating," IEEE Photonics Technology Letters **21**, 441-443 (2009).
11. Y. Liu, L. Wang, M. Zhang, D. Tu, X. Mao, and Y. Liao, "Long-Period Grating Relative Humidity Sensor With Hydrogel Coating," IEEE Photonics Technology Letters **19**, 880-882 (2007).
12. T. Wei, Y. Han, Y. Li, H.-L. Tsai, and H. Xiao, "Temperature-insensitive miniaturized fiber inline Fabry-Perot interferometer for highly sensitive refractive index measurement," Optics Express **16**, 5764-5769 (2008).
13. J. Lou, L. Tong, and Z. Ye, "Modeling of silica nanowires for optical sensing," Optics Express **13**, 2135-2140 (2005).
14. W. C. Wong, C. C. Chan, L. H. Chen, T. Li, K. X. Lee, and K. C. Leong, "Polyvinyl alcohol coated photonic crystal optical fiber sensor for humidity measurement," Sensors and Actuators B: Chemical **174**, 563-569 (2012).
15. L. V. Nguyen, S. C. Warren-Smith, A. Cooper, and T. M. Monro, "Molecular beacons immobilized within suspended core optical fiber for specific DNA detection," Optics Express **20**, 29378-29385 (2012).
16. C. K. Kirkendall and A. Dandridge, "Overview of high performance fibre-optic sensing," Journal of Physics D: Applied Physics **37**, R197-R216 (2004).
17. J. A. Bucaro, H. D. Dardy, and E. F. Carome, "Fiber‐optic hydrophone," The Journal of the Acoustical Society of America **62**, 1302-1304 (1977).

18. G. Kostovski, P. R. Stoddart, and A. Mitchell, "The Optical Fiber Tip: An Inherently Light-Coupled Microscopic Platform for Micro- and Nanotechnologies," Advanced Materials **26**, 3798-3820 (2014).
19. K. Totsu, Y. Haga, and M. Esashi, "Ultra-miniature fiber-optic pressure sensor using white light interferometry," Journal of Micromechanics and Microengineering **15**, 71-75 (2004).
20. C. Pang, F. Gesuele, A. Bruyant, S. Blaize, G. Lerondel, and P. Royer, "Enhanced light coupling in sub-wavelength single-mode silicon on insulator waveguides," Optics Express **17**, 6939-6945 (2009).
21. W. Parkes, V. Djakov, J. S. Barton, S. Watson, W. N. MacPherson, J. T. M. Stevenson, and C. C. Dunare, "Design and fabrication of dielectric diaphragm pressure sensors for applications to shock wave measurement in air," Journal of Micromechanics and Microengineering **17**, 1334-1342 (2007).
22. J.-Y. Fang, C.-H. Tien, and H.-P. D. Shieh, "Dual-probe near-field fiber head with gap servo control for data storage applications," Optics Express **15**, 14619-14628 (2007).
23. D. Iannuzzi, S. Deladi, V. J. Gadgil, R. G. P. Sanders, H. Schreuders, and M. C. Elwenspoek, "Monolithic fiber-top sensor for critical environments and standard applications," Applied Physics Letters **88**, 053501 (2006).
24. P. Jia and J. Yang, "Integration of large-area metallic nanohole arrays with multimode optical fibers for surface plasmon resonance sensing," Applied Physics Letters **102**, 243107 (2013).
25. E. J. Smythe, M. D. Dickey, J. Bao, G. M. Whitesides, and F. Capasso, "Optical Antenna Arrays on a Fiber Facet for in Situ Surface-Enhanced Raman Scattering Detection," Nano Letters **9**, 1132-1138 (2009).
26. A. Petrušis, J. H. Rector, K. Smith, S. de Man, and D. Iannuzzi, "The align-and-shine technique for series production of photolithography patterns on optical fibres," Journal of Micromechanics and Microengineering **19**, 047001 (2009).
27. G. Kostovski, D. J. White, A. Mitchell, M. W. Austin, and P. R. Stoddart, "Nanoimprinted optical fibres: Biotemplated nanostructures for SERS sensing," Biosensors and Bioelectronics **24**, 1531-1535 (2009).
28. S. Feng, X. Zhang, H. Wang, M. Xin, and Z. Lu, "Fiber coupled waveguide grating structures," Applied Physics Letters **96**, 133101 (2010).
29. Y. Lin, Y. Zou, and R. G. Lindquist, "A reflection-based localized surface plasmon resonance fiber-optic probe for biochemical sensing," Biomedical Optics Express **2**, 478-484 (2011).
30. F. Schiappelli, R. Kumar, M. Prasciolu, D. Cojoc, S. Cabrini, M. De Vittorio, G. Visimberga, A. Gerardino, V. Degiorgio, and E. Di Fabrizio, "Efficient fiber-to-waveguide coupling by a lens on the end of the optical fiber fabricated by focused ion beam milling," Microelectronic Engineering **73-74**, 397-404 (2004).
31. H. E. Williams, D. J. Freppon, S. M. Kuebler, R. C. Rumpf, and M. A. Melino, "Fabrication of three-dimensional micro-photonic structures on the tip of optical fibers using SU-8," Optics Express **19**, 22910-22922 (2011).
32. X. Lan, Y. Han, T. Wei, Y. Zhang, L. Jiang, H.-L. Tsai, and H. Xiao, "Surface-enhanced Raman-scattering fiber probe fabricated by femtosecond laser," Opt. Lett. **34**, 2285-2287 (2009).

33. M. Kahl, E. Voges, S. Kostrewa, C. Viets, and W. Hill, "Periodically structured metallic substrates for SERS," Sensors and Actuators B: Chemical **51**, 285-291 (1998).
34. Y. Lin, Y. Zou, Y. Mo, J. Guo, and R. G. Lindquist, "E-Beam Patterned Gold Nanodot Arrays on Optical Fiber Tips for Localized Surface Plasmon Resonance Biochemical Sensing," Sensors **10**, 9397-9406 (2010).
35. S. Kang, H.-E. Joe, J. Kim, Y. Jeong, B.-K. Min, and K. Oh, "Subwavelength plasmonic lens patterned on a composite optical fiber facet for quasi-one-dimensional Bessel beam generation," Applied Physics Letters **98**, 241103 (2011).
36. S. A. Maier, *Plasmonics: fundamentals and applications* (Springer Science & Business Media, 2007).
37. A. Dhawan, M. D. Gerhold, and J. F. Muth, "Plasmonic Structures Based on Subwavelength Apertures for Chemical and Biological Sensing Applications," IEEE Sensors Journal **8**, 942-950 (2008).
38. C. Viets and W. Hill, "Comparison of fibre-optic SERS sensors with differently prepared tips," Sensors and Actuators B: Chemical **51**, 92-99 (1998).
39. P. R. Stoddart and D. J. White, "Optical fibre SERS sensors," Analytical and Bioanalytical Chemistry **394**, 1761-1774 (2009).
40. A. Dhawan and J. F. Muth, "Engineering surface plasmon based fiber-optic sensors," Materials Science and Engineering: B **149**, 237-241 (2008).
41. A. Ashkin, "Acceleration and Trapping of Particles by Radiation Pressure," Physical Review Letters **24**, 156-159 (1970).
42. R. S. R. Ribeiro, O. Soppera, A. G. Oliva, A. Guerreiro, and P. A. S. Jorge, "New Trends on Optical Fiber Tweezers," Journal of Lightwave Technology **33**, 3394-3405 (2015).
43. C. Liberale, P. Minzioni, F. Bragheri, F. De Angelis, E. Di Fabrizio, and I. Cristiani, "Miniaturized all-fibre probe for three-dimensional optical trapping and manipulation," Nature Photonics **1**, 723 (2007).
44. N. Yu, P. Genevet, F. Aieta, M. A. Kats, R. Blanchard, G. Aoust, J. Tetienne, Z. Gaburro, and F. Capasso, "Flat Optics: Controlling Wavefronts With Optical Antenna Metasurfaces," IEEE Journal of Selected Topics in Quantum Electronics **19**, 4700423-4700423 (2013).
45. M. Principe, M. Consales, A. Micco, A. Crescitelli, G. Castaldi, E. Esposito, V. L. Ferrara, A. Cutolo, V. Galdi, and A. Cusano, *Meta-tips for lab-on-fiber optrodes*, Sixth European Workshop on Optical Fibre Sensors (EWOFS'2016) (SPIE, 2016), Vol. 9916.
46. A. V. Kildishev, A. Boltasseva, and V. M. Shalaev, "Planar Photonics with Metasurfaces," Science **339**, 1232009 (2013).
47. P. Vaiano, B. Carotenuto, M. Pisco, A. Ricciardi, G. Quero, M. Consales, A. Crescitelli, E. Esposito, and A. Cusano, "Lab on Fiber Technology for biological sensing applications," Laser & Photonics Reviews **10**, 922-961 (2016).
48. J. Xu, X. Wang, K. L. Cooper, and A. Wang, "Miniature all-silica fiber optic pressure and acoustic sensors," Opt. Lett. **30**, 3269-3271 (2005).
49. B. Yu, A. Wang, and G. R. Pickrell, "Analysis of Fiber Fabry-Pérot Interferometric Sensors Using Low-Coherence Light Sources," Journal of Lightwave Technology **24**, 1758 (2006).

50. K. Chen, Z. Gong, M. Guo, S. Yu, C. Qu, X. Zhou, and Q. Yu, "Fiber-optic Fabry-Perot interferometer based high sensitive cantilever microphone," Sensors and Actuators A: Physical **279**, 107-112 (2018).
51. R. A. Wolthuis, G. L. Mitchell, E. Saaski, J. C. Hartl, and M. A. Afromowitz, "Development of medical pressure and temperature sensors employing optical spectrum modulation," IEEE Transactions on Biomedical Engineering **38**, 974-981 (1991).
52. W. N. MacPherson, J. M. Kilpatrick, J. S. Barton, and J. D. C. Jones, "Miniature fiber optic pressure sensor for turbomachinery applications," Review of Scientific Instruments **70**, 1868-1874 (1999).
53. W. Wang, N. Wu, Y. Tian, C. Niezrecki, and X. Wang, "Miniature all-silica optical fiber pressure sensor with an ultrathin uniform diaphragm," Optics Express **18**, 9006-9014 (2010).
54. F. Wang, Z. Shao, J. Xie, Z. Hu, H. Luo, and Y. Hu, "Extrinsic Fabry–Pérot Underwater Acoustic Sensor Based on Micromachined Center-Embossed Diaphragm," Journal of Lightwave Technology **32**, 4628-4636 (2014).
55. F. Guo, T. Fink, M. Han, L. Koester, J. Turner, and J. Huang, "High-sensitivity, high-frequency extrinsic Fabry–Perot interferometric fiber-tip sensor based on a thin silver diaphragm," Opt. Lett. **37**, 1505-1507 (2012).
56. F. Xu, J. Shi, K. Gong, H. Li, R. Hui, and B. Yu, "Fiber-optic acoustic pressure sensor based on large-area nanolayer silver diaghragm," Opt. Lett. **39**, 2838-2840 (2014).
57. B. Liu, J. Lin, H. Liu, A. Jin, and P. Jin, "Extrinsic Fabry-Perot fiber acoustic pressure sensor based on large-area silver diaphragm," Microelectronic Engineering **166**, 50-54 (2016).
58. B. Liu, J. Lin, J. Wang, C. Ye, and P. Jin, "MEMS-Based High-Sensitivity Fabry–Perot Acoustic Sensor With a 45° Angled Fiber," IEEE Photonics Technology Letters **28**, 581-584 (2016).
59. F. Xu, D. Ren, X. Shi, C. Li, W. Lu, L. Lu, L. Lu, and B. Yu, "High-sensitivity Fabry–Perot interferometric pressure sensor based on a nanothick silver diaphragm," Opt. Lett. **37**, 133-135 (2012).
60. L. H. Chen, C. C. Chan, W. Yuan, S. K. Goh, and J. Sun, "High performance chitosan diaphragm-based fiber-optic acoustic sensor," Sensors and Actuators A: Physical **163**, 42-47 (2010).
61. Z. Gong, K. Chen, X. Zhou, Y. Yang, Z. Zhao, H. Zou, and Q. Yu, "High-Sensitivity Fabry-Perot Interferometric Acoustic Sensor for Low-Frequency Acoustic Pressure Detections," Journal of Lightwave Technology **35**, 5276-5279 (2017).
62. J. Ma, H. Xuan, H. L. Ho, W. Jin, Y. Yang, and S. Fan, "Fiber-Optic Fabry–Pérot Acoustic Sensor With Multilayer Graphene Diaphragm," IEEE Photonics Technology Letters **25**, 932-935 (2013).
63. C. Li, Q. Liu, X. Peng, and S. Fan, "Analyzing the temperature sensitivity of Fabry-Perot sensor using multilayer graphene diaphragm," Optics Express **23**, 27494-27502 (2015).
64. W. Ni, P. Lu, X. Fu, W. Zhang, P. P. Shum, H. Sun, C. Yang, D. Liu, and J. Zhang, "Ultrathin graphene diaphragm-based extrinsic Fabry-Perot interferometer for ultra-wideband fiber optic acoustic sensing," Optics Express **26**, 20758-20767 (2018).
65. J. Ma, W. Jin, H. L. Ho, and J. Y. Dai, "High-sensitivity fiber-tip pressure sensor with graphene diaphragm," Opt. Lett. **37**, 2493-2495 (2012).
66. Y. Wu, C. Yu, F. Wu, C. Li, J. Zhou, Y. Gong, Y. Rao, and Y. Chen, "A Highly Sensitive Fiber-

Optic Microphone Based on Graphene Oxide Membrane," Journal of Lightwave Technology **35**, 4344-4349 (2017).

67. F. Yu, Q. Liu, X. Gan, M. Hu, T. Zhang, C. Li, F. Kang, M. Terrones, and R. Lv, "Ultrasensitive Pressure Detection of Few-Layer MoS2," Advanced Materials **29**, 1603266 (2017).
68. L. Cheng, C. Wang, Y. Huang, H. Liang, and B.-O. Guan, "Silk fibroin diaphragm-based fiber-tip Fabry-Perot pressure sensor," Optics Express **24**, 19600-19606 (2016).
69. B. Yu, D. W. Kim, J. Deng, H. Xiao, and A. Wang, "Fiber Fabry-Perot sensors for detection of partial discharges in power transformers," Applied Optics **42**, 3241-3250 (2003).
70. C. Lee, X. Wei, J. W. Kysar, and J. Hone, "Measurement of the Elastic Properties and Intrinsic Strength of Monolayer Graphene," Science **321**, 385-388 (2008).
71. K. S. Novoselov, A. K. Geim, S. V. Morozov, D. Jiang, Y. Zhang, S. V. Dubonos, I. V. Grigorieva, and A. A. Firsov, "Electric Field Effect in Atomically Thin Carbon Films," Science **306**, 666-669 (2004).
72. G. C. Hill, R. Melamud, F. E. Declercq, A. A. Davenport, I. H. Chan, P. G. Hartwell, and B. L. Pruitt, "SU-8 MEMS Fabry-Perot pressure sensor," Sensors and Actuators A: Physical **138**, 52-62 (2007).
73. X. Wang, J. Xu, Y. Zhu, K. L. Cooper, and A. Wang, "All-fused-silica miniature optical fiber tip pressure sensor," Opt. Lett. **31**, 885-887 (2006).
74. Z. L. Ran, Y. J. Rao, W. J. Liu, X. Liao, and K. S. Chiang, "Laser-micromachined Fabry-Perot optical fiber tip sensor for high-resolution temperature-independent measurement of refractive index," Optics Express **16**, 2252-2263 (2008).
75. X. Yang, N. Ileri, C. C. Larson, T. C. Carlson, J. A. Britten, A. S. P. Chang, C. Gu, and T. C. Bond, "Nanopillar array on a fiber facet for highly sensitive surface-enhanced Raman scattering," Optics Express **20**, 24819-24826 (2012).
76. M. Prasciolu, D. Cojoc, S. Cabrini, L. Businaro, P. Candeloro, M. Tormen, R. Kumar, C. Liberale, V. Degiorgio, A. Gerardino, G. Gigli, D. Pisignano, E. Di Fabrizio, and R. Cingolani, "Design and fabrication of on-fiber diffractive elements for fiber-waveguide coupling by means of e-beam lithography," Microelectronic Engineering **67-68**, 169-174 (2003).
77. L. Tian, S. Frisbie, A. A. Bernussi, and M. Holtz, "Transmission properties of nanoscale aperture arrays in metallic masks on optical fibers," Journal of Applied Physics **101**, 014303 (2007).
78. J. K. Kim, Y. Jung, B. H. Lee, K. Oh, C. Chun, and D. Kim, "Optical phase-front inscription over optical fiber end for flexible control of beam propagation and beam pattern in free space," Optical Fiber Technology **13**, 240-245 (2007).
79. M. Consales, A. Ricciardi, A. Crescitelli, E. Esposito, A. Cutolo, and A. Cusano, "Lab-on-Fiber Technology: Toward Multifunctional Optical Nanoprobes," ACS Nano **6**, 3163-3170 (2012).
80. S. Choi, K. R. Kim, K. Oh, C. M. Chun, M. J. Kim, S. J. Yoo, and D. Y. Kim, "Interferometric inscription of surface relief gratings on optical fiber using azo polymer film," Applied Physics Letters **83**, 1080-1082 (2003).
81. R. L. Heredero, S. Martin, R. F. d. Caleya, A. B. L. Ribeiro, F. M. Araújo, L. A. Ferreira, J. L. Santos, and H. Guerrero, "A study of the optical properties of photopolymer Fabry-Perot microcavities by a dual-wavelength fibre optic architecture," Measurement Science and

Technology **13**, 1094-1099 (2002).

82. M. Sasaki, T. Ando, S. Nogawa, and K. Hane, "Direct Photolithography on Optical Fiber End," Japanese Journal of Applied Physics **41**, 4350-4355 (2002).
83. Y. Lin, J. Guo, and R. G. Lindquist, "Demonstration of an ultra-wideband optical fiber inline polarizer with metal nano-grid on the fiber tip," Optics Express **17**, 17849-17854 (2009).
84. G. Giannini, L. Mastrogiacomo, S. Cabrini, A. Gerardino, A. Nottola, V. Foglietti, and E. Cianci, "Microfabrication of diffractive optical elements onto the active region of optical fiber termination," in *Proc. MICRO tec*, 2000), 695-697.
85. J. A. Guggenheim, J. Li, T. J. Allen, R. J. Colchester, S. Noimark, O. Ogunlade, I. P. Parkin, I. Papakonstantinou, A. E. Desjardins, E. Z. Zhang, and P. C. Beard, "Ultrasensitive plano-concave optical microresonators for ultrasound sensing," Nature Photonics **11**, 714-719 (2017).
86. R. Kirchner and H. Schift, "Thermal reflow of polymers for innovative and smart 3D structures: A review," Materials Science in Semiconductor Processing **92**, 58-72 (2019).
87. T. Gang, C. Zuo, X. Liu, X. Bai, and M. Hu, "High-sensitive ultrasonic sensor using fiber-tip PVC diaphragm Fabry-Perot interferometer and its imaging application," Sensors and Actuators A: Physical **279**, 474-480 (2018).
88. M. Kimura and K. Toshima, "Vibration sensor using optical-fiber cantilever with bulb-lens," Sensors and Actuators A: Physical **66**, 178-183 (1998).
89. J. Laine, B. E. Little, and H. A. Haus, "Etch-eroded fiber coupler for whispering-gallery-mode excitation in high-Q silica microspheres," IEEE Photonics Technology Letters **11**, 1429-1430 (1999).
90. F. J. Steemers and D. R. Walt, "Multi-Analyte Sensing: From Site-Selective Deposition to Randomly-Ordered Addressable Optical Fiber Sensors," Microchimica Acta **131**, 99-105 (1999).
91. D. J. White and P. R. Stoddart, "Nanostructured optical fiber with surface-enhanced Raman scattering functionality," Opt. Lett. **30**, 598-600 (2005).
92. S. Jradi, O. Soppera, D. J. Lougnot, R. Bachelot, and P. Royer, "Tailoring the geometry of polymer tips on the end of optical fibers via control of physico-chemical parameters," Optical Materials **31**, 640-646 (2009).
93. R. Bachelot, C. Ecoffet, D. Deloeil, P. Royer, and D.-J. Lougnot, "Integration of micrometer-sized polymer elements at the end of optical fibers by free-radical photopolymerization," Applied Optics **40**, 5860-5871 (2001).
94. M. Hocine, R. Bachelot, C. Ecoffet, N. Fressengeas, P. Royer, and G. Kugel, "End-of-fiber polymer tip: manufacturing and modeling," Synthetic Metals **127**, 313-318 (2002).
95. O. Soppera, S. Jradi, and D. J. Lougnot, "Photopolymerization with microscale resolution: Influence of the physico-chemical and photonic parameters," Journal of Polymer Science Part A: Polymer Chemistry **46**, 3783-3794 (2008).
96. L. G. Cohen and M. V. Schneider, "Microlenses for Coupling Junction Lasers to Optical Fibers," Applied Optics **13**, 89-94 (1974).
97. L. Xiao, W. Jin, M. S. Demokan, H. L. Ho, H.-y. Tam, J. Ju, and J. Yu, "Photopolymer microtips for efficient light coupling between single-mode fibers and photonic crystal fibers," Opt. Lett. **31**, 1791-1793 (2006).

98. R. Bachelot, A. Fares, R. Fikri, D. Barchiesi, G. Lerondel, and P. Royer, "Coupling semiconductor lasers into single-mode optical fibers by use of tips grown by photopolymerization," Opt. Lett. **29**, 1971-1973 (2004).
99. A. Majumdar and H. Huang, "Compact optical fiber whitelight interferometric distance sensor for arbitrary small distance measurement," Applied Optics **48**, 3702-3708 (2009).
100. O. Frazão, P. Caldas, J. L. Santos, P. V. S. Marques, C. Turck, D. J. Lougnot, and O. Soppera, "Fabry-Perot refractometer based on an end-of-fiber polymer tip," Opt. Lett. **34**, 2474-2476 (2009).
101. X. Zheng, D. Guo, Y. Shao, S. Jia, S. Xu, B. Zhao, W. Xu, C. Corredor, and J. R. Lombardi, "Photochemical Modification of an Optical Fiber Tip with a Silver Nanoparticle Film: A SERS Chemical Sensor," Langmuir **24**, 4394-4398 (2008).
102. S. Pevec and D. Donlagic, "Miniature all-fiber Fabry–Perot sensor for simultaneous measurement of pressure and temperature," Applied Optics **51**, 4536-4541 (2012).
103. T. Zhu, T. Ke, Y. Rao, and K. S. Chiang, "Fabry–Perot optical fiber tip sensor for high temperature measurement," Optics Communications **283**, 3683-3685 (2010).
104. P. Morris, A. Hurrell, A. Shaw, E. Zhang, and P. Beard, "A Fabry-Perot fiber-optic ultrasonic hydrophone for the simultaneous measurement of temperature and acoustic pressure," J Acoust Soc Am **125**, 3611-3622 (2009).
105. M. Deng, C.-P. Tang, T. Zhu, Y.-J. Rao, L.-C. Xu, and M. Han, "Refractive index measurement using photonic crystal fiber-based Fabry-Perot interferometer," Applied optics **49**, 1593-1598 (2010).
106. Y.-J. Rao, M. Deng, D.-W. Duan, and T. Zhu, "In-line fiber Fabry-Perot refractive-index tip sensor based on endlessly photonic crystal fiber," Sensors and Actuators A: Physical **148**, 33-38 (2008).
107. L. H. Chen, T. Li, C. C. Chan, R. Menon, P. Balamurali, M. Shaillender, B. Neu, X. M. Ang, P. Zu, W. C. Wong, and K. C. Leong, "Chitosan based fiber-optic Fabry–Perot humidity sensor," Sensors and Actuators B: Chemical **169**, 167-172 (2012).
108. J. S. Santos, I. M. Raimundo, C. M. B. Cordeiro, C. R. Biazoli, C. A. J. Gouveia, and P. A. S. Jorge, "Characterisation of a Nafion film by optical fibre Fabry–Perot interferometry for humidity sensing," Sensors and Actuators B: Chemical **196**, 99-105 (2014).
109. D. Su, X. Qiao, Q. Rong, H. Sun, J. Zhang, Z. Bai, Y. Du, D. Feng, Y. Wang, M. Hu, and Z. Feng, "A fiber Fabry–Perot interferometer based on a PVA coating for humidity measurement," Optics Communications **311**, 107-110 (2013).
110. S. Tierney, S. Volden, and B. T. Stokke, "Glucose sensors based on a responsive gel incorporated as a Fabry-Perot cavity on a fiber-optic readout platform," Biosensors and Bioelectronics **24**, 2034-2039 (2009).
111. Y. Zheng, L. H. Chen, X. Dong, J. Yang, H. Y. Long, P. L. So, and C. C. Chan, "Miniature pH Optical Fiber Sensor Based on Fabry–Perot Interferometer," IEEE Journal of Selected Topics in Quantum Electronics **22**, 331-335 (2016).
112. N. Liu, J. Hui, C. Sun, J. Dong, L. Zhang, and H. Xiao, "Nanoporous Zeolite Thin Film-Based Fiber Intrinsic Fabry-Perot Interferometric Sensor for Detection of Dissolved Organics in Water," Sensors **6**, 835-847 (2006).
113. P. C. Beard and T. N. Mills, "Extrinsic optical-fiber ultrasound sensor using a thin polymer film as

a low-finesse Fabry–Perot interferometer," Applied Optics **35**, 663-675 (1996).

114. V. Callegari, D. Iwaniuk, R. Bronnimann, E. Schmid, and U. Sennhauser, "Optimized fabrication of curved surfaces by a FIB for direct focusing with glass fibres," Journal of Micromechanics and Microengineering **19**, 107003 (2009).

115. P. M. Nellen, V. Callegari, and R. Brönnimann, "FIB-milling of photonic structures and sputtering simulation," Microelectronic Engineering **83**, 1805-1808 (2006).

116. S. Cabrini, C. Liberale, D. Cojoc, A. Carpentiero, M. Prasciolu, S. Mora, V. Degiorgio, F. De Angelis, and E. Di Fabrizio, "Axicon lens on optical fiber forming optical tweezers, made by focused ion beam milling," Microelectronic Engineering **83**, 804-807 (2006).

117. G. F. S. Andrade, J. G. Hayashi, M. M. Rahman, W. J. Salcedo, C. M. B. Cordeiro, and A. G. Brolo, "Surface-Enhanced Resonance Raman Scattering (SERRS) Using Au Nanohole Arrays on Optical Fiber Tips," Plasmonics **8**, 1113-1121 (2013).

118. A. Micco, A. Ricciardi, M. Pisco, V. La Ferrara, and A. Cusano, "Optical fiber tip templating using direct focused ion beam milling," Scientific Reports **5**, 15935 (2015).

119. D. Iannuzzi, S. Deladi, J. W. Berenschot, S. d. Man, K. Heeck, and M. C. Elwenspoek, "Fiber-top atomic force microscope," Review of Scientific Instruments **77**, 106105 (2006).

120. D. Iannuzzi, K. Heeck, M. Slaman, S. de Man, J. H. Rector, H. Schreuders, J. W. Berenschot, V. J. Gadgil, R. G. P. Sanders, M. C. Elwenspoek, and S. Deladi, "Fibre-top cantilevers: design, fabrication and applications," Measurement Science and Technology **18**, 3247-3252 (2007).

121. C. J. Alberts, S. d. Man, J. W. Berenschot, V. J. Gadgil, M. C. Elwenspoek, and D. Iannuzzi, "Fiber-top refractometer," Measurement Science and Technology **20**, 034005 (2009).

122. D. Iannuzzi, M. Slaman, J. H. Rector, H. Schreuders, S. Deladi, and M. C. Elwenspoek, "A fiber-top cantilever for hydrogen detection," Sensors and Actuators B: Chemical **121**, 706-708 (2007).

123. G. Gruca, D. Chavan, J. Rector, K. Heeck, and D. Iannuzzi, "Demonstration of an optically actuated ferrule-top device for pressure and humidity sensing," Sensors and Actuators A: Physical **190**, 77-83 (2013).

124. S. V. Beekmans and D. Iannuzzi, "Characterizing tissue stiffness at the tip of a rigid needle using an opto-mechanical force sensor," Biomedical Microdevices **18**, 15 (2016).

125. A. A. Said, M. Dugan, S. d. Man, and D. Iannuzzi, "Carving fiber-top cantilevers with femtosecond laser micromachining," Journal of Micromechanics and Microengineering **18**, 035005 (2008).

126. K. Jun Ki, K. Jun Ki, K. Jongki, O. Kyunghwan, S. Ik-Bu, S. Woojin, C. Hae Young, and L. Byeongha, "Fabrication of Micro Fresnel Zone Plate Lens on a Mode-Expanded Hybrid Optical Fiber Using a Femtosecond Laser Ablation System," IEEE Photonics Technology Letters **21**, 21-23 (2009).

127. W. Shin, I. B. Sohn, B. Yu, Y. L. Lee, S. C. Choi, Y. Noh, J. Lee, and D. Ko, "Microstructured Fiber End Surface Grating for Coarse WDM Signal Monitoring," IEEE Photonics Technology Letters **19**, 550-552 (2007).

128. X. Ma, H. Huo, W. Wang, Y. Tian, N. Wu, C. Guthy, M. Shen, and X. Wang, "Surface-Enhanced Raman Scattering Sensor on an Optical Fiber Probe Fabricated with a Femtosecond Laser," Sensors **10**, 11064-11071 (2010).

129. E. G. Johnson, J. Stack, T. J. Suleski, C. Koehler, and W. Delaney, "Fabrication of micro optics on

coreless fiber segments," Applied Optics **42**, 785-791 (2003).

130. S. Tibuleac, D. Wawro, and R. Magnusson, "Resonant diffractive structures integrating waveguide-gratings on optical fiber endfaces," in *1999 IEEE LEOS Annual Meeting Conference Proceedings. LEOS'99. 12th Annual Meeting. IEEE Lasers and Electro-Optics Society 1999 Annual Meeting (Cat. No.99CH37009)*, 1999), 874-875 vol.872.

131. S. Feng, S. Darmawi, T. Henning, P. J. Klar, and X. Zhang, "A Miniaturized Sensor Consisting of Concentric Metallic Nanorings on the End Facet of an Optical Fiber," Small **8**, 1937-1944 (2012).

132. A. Ostendorf and B. N. Chichkov, "Two-photon polymerization: a new approach to micromachining," Photonics spectra **40**, 72 (2006).

133. S. Maruo, O. Nakamura, and S. Kawata, "Three-dimensional microfabrication with two-photon-absorbed photopolymerization," Opt. Lett. **22**, 132-134 (1997).

134. B. H. Cumpston, S. P. Ananthavel, S. Barlow, D. L. Dyer, J. E. Ehrlich, L. L. Erskine, A. A. Heikal, S. M. Kuebler, I. Y. S. Lee, D. McCord-Maughon, J. Qin, H. Röckel, M. Rumi, X.-L. Wu, S. R. Marder, and J. W. Perry, "Two-photon polymerization initiators for three-dimensional optical data storage and microfabrication," Nature **398**, 51-54 (1999).

135. J. Serbin, A. Egbert, A. Ostendorf, B. N. Chichkov, R. Houbertz, G. Domann, J. Schulz, C. Cronauer, L. Fröhlich, and M. Popall, "Femtosecond laser-induced two-photon polymerization of inorganic–organic hybrid materials for applications in photonics," Opt. Lett. **28**, 301-303 (2003).

136. C. Liberale, G. Cojoc, P. Candeloro, G. Das, F. Gentile, F. D. Angelis, and E. D. Fabrizio, "Micro-Optics Fabrication on Top of Optical Fibers Using Two-Photon Lithography," IEEE Photonics Technology Letters **22**, 474-476 (2010).

137. G. Cojoc, C. Liberale, P. Candeloro, F. Gentile, G. Das, F. De Angelis, and E. Di Fabrizio, "Optical micro-structures fabricated on top of optical fibers by means of two-photon photopolymerization," Microelectronic Engineering **87**, 876-879 (2010).

138. T. Gissibl, S. Thiele, A. Herkommer, and H. Giessen, "Two-photon direct laser writing of ultracompact multi-lens objectives," Nature Photonics **10**, 554 (2016).

139. T. Gissibl, S. Thiele, A. Herkommer, and H. Giessen, "Sub-micrometre accurate free-form optics by three-dimensional printing on single-mode fibres," Nature Communications **7**, 11763 (2016).

140. M. Li, Y. Liu, X. Zhao, R. Gao, Y. Li, and S. Qu, "High sensitivity fiber acoustic sensor tip working at 1550nm fabricated by two-photon polymerization technique," Sensors and Actuators A: Physical **260**, 29-34 (2017).

141. V. Melissinaki, M. Farsari, and S. Pissadakis, "A Fiber-Endface, Fabry–Perot Vapor Microsensor Fabricated by Multiphoton Polymerization," IEEE Journal of Selected Topics in Quantum Electronics **21**, 344-353 (2015).

142. V. Melissinaki, I. Konidakis, M. Farsari, and S. Pissadakis, "Fiber Endface Fabry–Perot Microsensor With Distinct Response to Vapors of Different Chlorinated Organic Solvents," IEEE Sensors Journal **16**, 7094-7100 (2016).

143. V. Melissinaki, M. Farsari, and S. Pissadakis, "A Fiber Optic Fabry–Perot Cavity Sensor for the Probing of Oily Samples," Fibers **5**, 1 (2017).

144. Z. Xie, S. Feng, P. Wang, L. Zhang, X. Ren, L. Cui, T. Zhai, J. Chen, Y. Wang, X. Wang, W. Sun, J. Ye, P. Han, P. J. Klar, and Y. Zhang, "Demonstration of a 3D Radar-Like SERS Sensor Micro-

and Nanofabricated on an Optical Fiber," Advanced Optical Materials **3**, 1232-1239 (2015).

145. A. J. Thompson, M. Power, and G.-Z. Yang, "Micro-scale fiber-optic force sensor fabricated using direct laser writing and calibrated using machine learning," Optics Express **26**, 14186-14200 (2018).

146. E. J. Smythe, M. D. Dickey, G. M. Whitesides, and F. Capasso, "A Technique to Transfer Metallic Nanoscale Patterns to Small and Non-Planar Surfaces," ACS Nano **3**, 59-65 (2009).

147. D. J. Lipomi, R. V. Martinez, M. A. Kats, S. H. Kang, P. Kim, J. Aizenberg, F. Capasso, and G. M. Whitesides, "Patterning the Tips of Optical Fibers with Metallic Nanostructures Using Nanoskiving," Nano Letters **11**, 632-636 (2011).

148. G. Shambat, J. Provine, K. Rivoire, T. Sarmiento, J. Harris, and J. Vučković, "Optical fiber tips functionalized with semiconductor photonic crystal cavities," Applied Physics Letters **99**, 191102 (2011).

149. G. Shambat, S. R. Kothapalli, A. Khurana, J. Provine, T. Sarmiento, K. Cheng, Z. Cheng, J. Harris, H. Daldrup-Link, S. S. Gambhir, and J. Vučković, "A photonic crystal cavity-optical fiber tip nanoparticle sensor for biomedical applications," Applied Physics Letters **100**, 213702 (2012).

150. P. Jia and J. Yang, "A plasmonic optical fiber patterned by template transfer as a high-performance flexible nanoprobe for real-time biosensing," Nanoscale **6**, 8836-8843 (2014).

151. C. L. Arce, K. D. Vos, T. Claes, K. Komorowska, D. V. Thourhout, and P. Bienstman, "Silicon-on-Insulator Microring Resonator Sensor Integrated on an Optical Fiber Facet," IEEE Photonics Technology Letters **23**, 890-892 (2011).

152. I. W. Jung, B. Park, J. Provine, R. T. Howe, and O. Solgaard, "Highly Sensitive Monolithic Silicon Photonic Crystal Fiber Tip Sensor for Simultaneous Measurement of Refractive Index and Temperature," Journal of Lightwave Technology **29**, 1367-1374 (2011).

153. S. Hadzialic, S. Kim, S. B. Mallick, A. Sudbo, and O. Solgaard, "Monolithic Photonic Crystals," in *LEOS 2007 - IEEE Lasers and Electro-Optics Society Annual Meeting Conference Proceedings*, 2007), 341-342.

154. G. M. Whitesides and B. Grzybowski, "Self-Assembly at All Scales," Science **295**, 2418-2421 (2002).

155. C. Shi, H. Yan, C. Gu, D. Ghosh, L. Seballos, S. Chen, J. Z. Zhang, and B. Chen, "A double substrate “sandwich” structure for fiber surface enhanced Raman scattering detection," Applied Physics Letters **92**, 103107 (2008).

156. H.-H. Jeong, N. Erdene, J.-H. Park, D.-H. Jeong, H.-Y. Lee, and S.-K. Lee, "Real-time label-free immunoassay of interferon-gamma and prostate-specific antigen using a Fiber-Optic Localized Surface Plasmon Resonance sensor," Biosensors and Bioelectronics **39**, 346-351 (2013).

157. B. Sciacca and T. M. Monro, "Dip Biosensor Based on Localized Surface Plasmon Resonance at the Tip of an Optical Fiber," Langmuir **30**, 946-954 (2014).

158. F. L. Yap, P. Thoniyot, S. Krishnan, and S. Krishnamoorthy, "Nanoparticle Cluster Arrays for High-Performance SERS through Directed Self-Assembly on Flat Substrates and on Optical Fibers," ACS Nano **6**, 2056-2070 (2012).

159. M. Pisco, F. Galeotti, G. Quero, A. Iadicicco, M. Giordano, and A. Cusano, "Miniaturized Sensing Probes Based on Metallic Dielectric Crystals Self-Assembled on Optical Fiber Tips," ACS

Photonics **1**, 917-927 (2014).
160. C. Alberts, S. De Man, J. W. Berenschot, V. Gadgil, M. C. Elwenspoek, and D. Iannuzzi, "Fiber-top refractometer," Measurement science and technology **20**, 034005 (2009).
161. A. Cipullo, G. Gruca, K. Heeck, F. De Filippis, D. Iannuzzi, A. Minardo, and L. Zeni, "Velocity measurements of low speed air ows by ferrule-top cantilever optical ber sensor," Sensors and Actuators A-Physical **17**(2012).
162. N. Ma, P. C. Ashok, D. J. Stevenson, F. J. Gunn-Moore, and K. Dholakia, "Integrated optical transfection system using a microlens fiber combined with microfluidic gene delivery," Biomedical Optics Express **1**, 694-705 (2010).
163. Y. Lin, Y. Zou, Y. Mo, J. Guo, and R. G. Lindquist, "E-beam patterned gold nanodot arrays on optical fiber tips for localized surface plasmon resonance biochemical sensing," Sensors (Basel) **10**, 9397-9406 (2010).
164. G. Kostovski, D. White, A. Mitchell, M. Austin, and P. Stoddart, "Nanoimprinted optical fibres: Biotemplated nanostructures for SERS sensing," Biosensors and Bioelectronics **24**, 1531-1535 (2009).
165. M. Aspelmeyer, T. J. Kippenberg, and F. Marquardt, *Cavity optomechanics: nano-and micromechanical resonators interacting with light* (Springer, 2014).
166. S. Bose, K. Jacobs, and P. L. Knight, "Preparation of nonclassical states in cavities with a moving mirror," Physical Review A **56**, 4175-4186 (1997).
167. A. Abramovici, W. E. Althouse, R. W. P. Drever, Y. Gürsel, S. Kawamura, F. J. Raab, D. Shoemaker, L. Sievers, R. E. Spero, K. S. Thorne, R. E. Vogt, R. Weiss, S. E. Whitcomb, and M. E. Zucker, "LIGO: The Laser Interferometer Gravitational-Wave Observatory," Science **256**, 325-333 (1992).
168. A. Dorsel, J. D. McCullen, P. Meystre, E. Vignes, and H. Walther, "Optical Bistability and Mirror Confinement Induced by Radiation Pressure," Physical Review Letters **51**, 1550-1553 (1983).
169. B. S. Sheard, M. B. Gray, C. M. Mow-Lowry, D. E. McClelland, and S. E. Whitcomb, "Observation and characterization of an optical spring," Physical Review A **69**, 051801 (2004).
170. T. Corbitt, C. Wipf, T. Bodiya, D. Ottaway, D. Sigg, N. Smith, S. Whitcomb, and N. Mavalvala, "Optical Dilution and Feedback Cooling of a Gram-Scale Oscillator to 6.9 mK," Physical Review Letters **99**, 160801 (2007).
171. S. Olcum, N. Cermak, S. C. Wasserman, K. S. Christine, H. Atsumi, K. R. Payer, W. Shen, J. Lee, A. M. Belcher, S. N. Bhatia, and S. R. Manalis, "Weighing nanoparticles in solution at the attogram scale," Proceedings of the National Academy of Sciences **111**, 1310-1315 (2014).
172. G. Binnig, C. F. Quate, and C. Gerber, "Atomic Force Microscope," Physical Review Letters **56**, 930-933 (1986).
173. F. J. Giessibl, "Advances in atomic force microscopy," Reviews of Modern Physics **75**, 949-983 (2003).
174. N. V. Lavrik, M. J. Sepaniak, and P. G. Datskos, "Cantilever transducers as a platform for chemical and biological sensors," Review of Scientific Instruments **75**, 2229-2253 (2004).
175. J. Wu, X. Guo, A. P. Zhang, and H.-Y. Tam, "Rapid 3D μ-printing of polymer optical whispering-gallery mode resonators," Optics express **23**, 29708-29714 (2015).
176. M. J. Yin, M. Yao, S. Gao, A. P. Zhang, H. Y. Tam, and P. K. A. Wai, "Rapid 3D Patterning of Poly

(acrylic acid) Ionic Hydrogel for Miniature pH Sensors," Advanced Materials (2015).
177. A. P. Zhang, X. Qu, P. Soman, K. C. Hribar, J. W. Lee, S. Chen, and S. He, "Rapid Fabrication of Complex 3D Extracellular Microenvironments by Dynamic Optical Projection Stereolithography," Advanced Materials **24**, 4266-4270 (2012).
178. C. W. De Silva, *Vibration: fundamentals and practice* (CRC press, 1999).
179. T. Wang, S. Zheng, and Z. Yang, "A high precision displacement sensor using a low-finesse fiber-optic Fabry-Pérot interferometer," Sensors and Actuators A: Physical **69**, 134-138 (1998).
180. A. Koch and R. Ulrich, "Fiber-optic displacement sensor with 0.02 μm resolution by white-light interferometry," Sensors and Actuators A: Physical **25**, 201-207 (1990).
181. C. Zhong, C. Shen, Y. You, J. Chu, X. Zou, X. Dong, Y. Jin, and J. Wang, "Temperature-insensitive optical fiber two-dimensional micrometric displacement sensor based on an in-line Mach–Zehnder interferometer," J. Opt. Soc. Am. B **29**, 1136-1140 (2012).
182. Y. Alayli, S. Topçu, D. Wang, R. Dib, and L. Chassagne, "Applications of a high accuracy optical fiber displacement sensor to vibrometry and profilometry," Sensors and Actuators A: Physical **116**, 85-90 (2004).
183. J. H. Ng, X. Zhou, X. Yang, and J. Hao, "A simple temperature-insensitive fiber Bragg grating displacement sensor," Optics Communications **273**, 398-401 (2007).
184. D. Chavan, T. C. v. d. Watering, G. Gruca, J. H. Rector, K. Heeck, M. Slaman, and D. Iannuzzi, "Ferrule-top nanoindenter: An optomechanical fiber sensor for nanoindentation," Review of Scientific Instruments **83**, 115110 (2012).
185. "Fiber Optic Sensors," in *Wiley Encyclopedia of Biomedical Engineering*.
186. B. Lee, "Review of the present status of optical fiber sensors," Optical Fiber Technology **9**, 57-79 (2003).
187. A. D. Kersey and A. Dandridge, "Applications of fiber-optic sensors," IEEE Transactions on Components, Hybrids, and Manufacturing Technology **13**, 137-143 (1990).
188. C. Caucheteur, T. Guo, and J. Albert, "Review of plasmonic fiber optic biochemical sensors: improving the limit of detection," Analytical and Bioanalytical Chemistry **407**, 3883-3897 (2015).
189. G. F. S. Andrade, M. Fan, and A. G. Brolo, "Multilayer silver nanoparticles-modified optical fiber tip for high performance SERS remote sensing," Biosensors and Bioelectronics **25**, 2270-2275 (2010).
190. K. Schroeder, W. Ecke, R. Mueller, R. Willsch, and A. Andreev, "A fibre Bragg grating refractometer," Measurement Science and Technology **12**, 757-764 (2001).
191. L. Alwis, T. Sun, and K. Grattan, "Fibre optic long period grating-based humidity sensor probe using a Michelson interferometric arrangement," Sensors and Actuators B: Chemical **178**, 694-699 (2013).
192. D. Jin-Fei, A. P. Zhang, S. Li-Yang, Y. Jin-Hua, and H. Sailing, "Fiber-taper seeded long-period grating pair as a highly sensitive refractive-index sensor," IEEE Photonics Technology Letters **17**, 1247-1249 (2005).
193. B. Gu, M.-J. Yin, A. P. Zhang, J.-W. Qian, and S. He, "Low-cost high-performance fiber-optic pH sensor based on thin-core fiber modal interferometer," Optics Express **17**, 22296-22302 (2009).
194. Z. Ran, Y. Rao, J. Zhang, Z. Liu, and B. Xu, "A miniature fiber-optic refractive-index sensor based

on laser-machined Fabry–Perot interferometer tip," Journal of Lightwave Technology **27**, 5426-5429 (2009).

195. S. Zhu, F. Pang, S. Huang, F. Zou, Y. Dong, and T. Wang, "High sensitivity refractive index sensor based on adiabatic tapered optical fiber deposited with nanofilm by ALD," Optics Express **23**, 13880-13888 (2015).

196. D. Monzón-Hernández and J. Villatoro, "High-resolution refractive index sensing by means of a multiple-peak surface plasmon resonance optical fiber sensor," Sensors and Actuators B: Chemical **115**, 227-231 (2006).

197. J. Cao, M. H. Tu, T. Sun, and K. T. Grattan, "Wavelength-based localized surface plasmon resonance optical fiber biosensor," Sensors and Actuators B: Chemical **181**, 611-619 (2013).

198. N. Lindenmann, G. Balthasar, D. Hillerkuss, R. Schmogrow, M. Jordan, J. Leuthold, W. Freude, and C. Koos, "Photonic wire bonding: a novel concept for chip-scale interconnects," Optics Express **20**, 17667-17677 (2012).

199. J. Wu, X. Guo, A. P. Zhang, and H.-Y. Tam, "Rapid 3D µ-printing of polymer optical whispering-gallery mode resonators," Optics Express **23**, 29708-29714 (2015).

200. J. Wu, M.-j. Yin, K. Seefeldt, A. Dani, R. Guterman, J. Yuan, A. P. Zhang, and H.-Y. Tam, "In situ μ-printed optical fiber-tip CO2 sensor using a photocrosslinkable poly(ionic liquid)," Sensors and Actuators B: Chemical **259**, 833-839 (2018).

201. X. Ouyang, K. Zhang, J. Wu, D. S.-H. Wong, Q. Feng, L. Bian, and A. P. Zhang, "Optical μ-Printing of Cellular-Scale Microscaffold Arrays for 3D Cell Culture," Scientific Reports **7**, 8880 (2017).

202. M. Yao, P. K. A. Wai, J. Wu, A. P. Zhang, and H. Tam, "Optical 3D μ-printing of ferrule-top polymer suspended-mirror devices," in *2016 IEEE SENSORS*, 2016), 1-3.

203. A. P. Zhang, S. Li-Yang, D. Jin-Fei, and H. Sailing, "Sandwiched long-period gratings for simultaneous measurement of refractive index and temperature," IEEE Photonics Technology Letters **17**, 2397-2399 (2005).

204. T.-H. Xia, A. P. Zhang, B. Gu, and J.-J. Zhu, "Fiber-optic refractive-index sensors based on transmissive and reflective thin-core fiber modal interferometers," Optics Communications **283**, 2136-2139 (2010).

205. K. P. Birch and M. J. Downs, "An Updated Edlén Equation for the Refractive Index of Air," Metrologia **30**, 155-162 (1993).

206. S. Mc Murtry, J. D. Wright, and D. A. Jackson, "Sensing applications of a low-coherence fibre-optic interferometer measuring the refractive index of air," Sensors and Actuators B: Chemical **72**, 69-74 (2001).

207. D.-w. Duan, Y.-j. Rao, and T. Zhu, "High sensitivity gas refractometer based on all-fiber open-cavity Fabry–Perot interferometer formed by large lateral offset splicing," J. Opt. Soc. Am. B **29**, 912-915 (2012).

208. A. Shrivastava and V. Gupta, "Methods for the determination of limit of detection and limit of quantitation of the analytical methods," Chronicles of Young Scientists **2**, 21-25 (2011).

209. F. Li, Y. Liu, L. Wang, and Z. Zhao, "Investigation on the response of fused taper couplers to ultrasonic wave," Applied Optics **54**, 6986-6993 (2015).

210. P. Beard, "Biomedical photoacoustic imaging," Interface Focus **1**, 602-631 (2011).

211. M. Ichihara, M. Takeo, A. Yokoo, J. Oikawa, and T. Ohminato, "Monitoring volcanic activity using correlation patterns between infrasound and ground motion," Geophysical Research Letters **39**(2012).

212. N. Takahashi, K. Yoshimura, S. Takahashi, and K. Imamura, "Development of an optical fiber hydrophone with fiber Bragg grating," Ultrasonics **38**, 581-585 (2000).

213. A. P. Jathoul, J. Laufer, O. Ogunlade, B. Treeby, B. Cox, E. Zhang, P. Johnson, A. R. Pizzey, B. Philip, T. Marafioti, M. F. Lythgoe, R. B. Pedley, M. A. Pule, and P. Beard, "Deep in vivo photoacoustic imaging of mammalian tissues using a tyrosinase-based genetic reporter," Nature Photonics **9**, 239 (2015).

214. H. F. Zhang, K. Maslov, G. Stoica, and L. V. Wang, "Functional photoacoustic microscopy for high-resolution and noninvasive in vivo imaging," Nature Biotechnology **24**, 848-851 (2006).

215. Y. Cao, W. Jin, H. L. Ho, and J. Ma, "Miniature fiber-tip photoacoustic spectrometer for trace gas detection," Opt. Lett. **38**, 434-436 (2013).

216. K. Chen, M. Guo, S. Liu, B. Zhang, H. Deng, Y. Zheng, Y. Chen, C. Luo, L. Tao, M. Lou, and Q. Yu, "Fiber-optic photoacoustic sensor for remote monitoring of gas micro-leakage," Optics Express **27**, 4648-4659 (2019).

217. J.-M. Yang, K. Maslov, H.-C. Yang, Q. Zhou, K. K. Shung, and L. V. Wang, "Photoacoustic endoscopy," Opt. Lett. **34**, 1591-1593 (2009).

218. M. Han, T. Liu, L. Hu, and Q. Zhang, "Intensity-demodulated fiber-ring laser sensor system for acoustic emission detection," Optics Express **21**, 29269-29276 (2013).

219. B. Xu, Y. Li, M. Sun, Z.-W. Zhang, X.-Y. Dong, Z.-X. Zhang, and S.-Z. Jin, "Acoustic vibration sensor based on nonadiabatic tapered fibers," Opt. Lett. **37**, 4768-4770 (2012).

220. Y. Li, X. Wang, and X. Bao, "Sensitive acoustic vibration sensor using single-mode fiber tapers," Applied Optics **50**, 1873-1878 (2011).

221. W. Ni, P. Lu, X. Fu, S. Wang, Y. Sun, D. Liu, and J. Zhang, "Highly Sensitive Optical Fiber Curvature and Acoustic Sensor Based on Thin Core Ultralong Period Fiber Grating," IEEE Photonics Journal **9**, 1-9 (2017).

222. D. Pawar, C. N. Rao, R. K. Choubey, and S. N. Kale, "Mach-Zehnder interferometric photonic crystal fiber for low acoustic frequency detections," Applied Physics Letters **108**, 041912 (2016).

223. L. Liu, P. Lu, H. Liao, S. Wang, W. Yang, D. Liu, and J. Zhang, "Fiber-Optic Michelson Interferometric Acoustic Sensor Based on a PP/PET Diaphragm," IEEE Sensors Journal **16**, 3054-3058 (2016).

224. S. Wang, P. Lu, L. Liu, H. Liao, Y. Sun, W. Ni, X. Fu, X. Jiang, D. Liu, J. Zhang, H. Xu, Q. Yao, and Y. Chen, "An Infrasound Sensor Based on Extrinsic Fiber-Optic Fabry–Perot Interferometer Structure," IEEE Photonics Technology Letters **28**, 1264-1267 (2016).

225. L. Liu, P. Lu, S. Wang, X. Fu, Y. Sun, D. Liu, J. Zhang, H. Xu, and Q. Yao, "UV Adhesive Diaphragm-Based FPI Sensor for Very-Low-Frequency Acoustic Sensing," IEEE Photonics Journal **8**, 1-9 (2016).

226. S. Dass and R. Jha, "Tapered Fiber Attached Nitrile Diaphragm-Based Acoustic Sensor," Journal of Lightwave Technology **35**, 5411-5417 (2017).

227. H. Liao, P. Lu, L. Liu, S. Wang, W. Ni, X. Fu, D. Liu, and J. Zhang, "Phase Demodulation of Short-Cavity Fabry–Perot Interferometric Acoustic Sensors With Two Wavelengths," IEEE Photonics Journal **9**, 1-9 (2017).

228. J. Jiang, T. Zhang, S. Wang, K. Liu, C. Li, Z. Zhao, and T. Liu, "Noncontact Ultrasonic Detection in Low-Pressure Carbon Dioxide Medium Using High Sensitivity Fiber-Optic Fabry–Perot Sensor System," Journal of Lightwave Technology **35**, 5079-5085 (2017).

229. J. Liu, L. Yuan, J. Lei, W. Zhu, B. Cheng, Q. Zhang, Y. Song, C. Chen, and H. Xiao, "Micro-cantilever-based fiber optic hydrophone fabricated by a femtosecond laser," Opt Lett **42**, 2459-2462 (2017).

230. J. E. Sader, "Frequency response of cantilever beams immersed in viscous fluids with applications to the atomic force microscope," Journal of Applied Physics **84**, 64-76 (1998).